Title
Satellite Observations and Dynamic Rupture Modeling of the 2021 Haiti Earthquake

Author
Yin, Harriet Zoe

Publication Date
2024

Peer reviewed|Thesis/dissertation

UNIVERSITY OF CALIFORNIA SAN DIEGO

Satellite Observations and Dynamic Rupture Modeling of the 2021 Haiti Earthquake

A dissertation submitted in partial satisfaction of the
requirements for the degree Doctor of Philosophy

in

Earth Sciences

by

Harriet Zoe Louisa Yin

Committee in charge:

Jennifer S. Haase, Chair
Alice Agnes Gabriel
Ross Parnell-Turner
David T. Sandwell
Lelli Van Den Einde
Xiaohua Xu

2024

The Dissertation of Harriet Zoe Louisa Yin is approved, and it is acceptable in quality and form for publication on microfilm and electronically.

University of California San Diego

2024

TABLE OF CONTENTS

LIST OF FIGURES

LIST OF TABLES

ACKNOWLEDGEMENTS

First, I would like to thank Jennifer Haase, my advisor and mentor who first allowed me to join her research group and then supported and encouraged me throughout opportunities, setbacks, successes, and unforgettable experiences during my time at Scripps. Her creative, energetic, and inclusive approach to science is something I admire greatly and hope to emulate in my own career. I am grateful to each of my committee members with whom I was lucky enough to collaborate. I am so grateful for their support.

I have many to thank for patiently and thoughtfully answering my many questions (no matter how large or small) and generously offering their insights and expertise as I bumbled along: members of the Gabriel research group, especially Mathilde Marchandon, Jeremy Wong, Fabian Kutschera, Jeena Yun, and Thomas Ulrich; members of the Sandwell research group: especially Hugh Harper, Katherine Guns, Xiaohua Xu, Yao Yu; Debi Kilb with whom I discussed many an idea over many a lunch (mostly brought to me!); and, of course, members of the Haase research group: especially Bing Cao, Ignacio Sepulveda, and Jessie Saunders. The Haitian earthquake science community has been unfailingly kind and open towards me. I have benefited greatly from many discussions with others studying this complicated region including: Steeve Symithe, Bryan Raimbault, Roby Douilly, Eric Calais, Veronica Cedillos, Bernard Mercier deLepinay, and others.

I am grateful to Heidi Tremayne, Anna Lang, and many others in the EERI community who introduced me to a framework for understanding earthquake hazard and risk and how it shapes lives and communities. This has motivated and guided my graduate work and will, I'm sure, continue to shape my work long into the future.

I don't think I knew that a community like the one at Scripps existed before I experienced it for myself. The people I have met here have been nothing short of exceptional. Their brilliance, kindness, quirkiness, and openness are unmatched and I will forever be indebted to them. They include (but are far from limited to): Hugh Harper, Andi Adams, Yao Yu, Nicole Clizzie, Gabrielle Hobson, Zel Hurewitz, Margaret Morris, Phil Choi, and Fabian Kutschera. You've made IGPP not just a great workplace but a home.

I find it difficult to separate between the IGPP community and my personal community because so many at IGPP have become some of my closest friends. I'm thinking of: Hannah Peterson, Chloe Gustafson, Derek Alcorn, Maya Becker, Drake Singleton, Ryley Hill, Eliza McCall, Dani Blatter, Wes Neeley, and Olivia Padilla. They have brightened my world immesurably and I wouldn't have made it here without them.

I am so grateful for my office mate and dear friend, Nick Lau, without whom my PhD would have been much less full of jokes, naps, beers, and races up the Scripps hill. And I would not have made it to this point without my beloved friend Susheel Adusumilli (friend/roommate/officemate extraordinaire) who always manages to see the best in me and is generous with his time, knowledge, and friendship without fail.

There are also so many others who I met along the way: Thanks to Anne Schulberg, Mika Topitzes, Gaby Negrete-Garcia, Gabby Velasquez, and Julia Dohner for being wonderful friends, supportive confidants, and always bringing the fun, adventure, and delicious treats. Thanks to the Data Lagers and Pickleball Crew: Gaby Thomas, Kieran Lenssen, Bobby Sanchez, Emma Beer, Jake Mitchem, Jaedyn Francovich (and of course, Chloe, Derek, Susheel, and Nick) and many others who kept my Thursday and Friday nights full of laughter and life. Thanks also to friends from outside of San Diego, especially Lea Hamilton and Sam Trejo. And, of course, I'm so grateful to Jacob Morgan who has never stopped being encouraging, supportive, and just making life fun.

To my family: Mom, Dad, and Bili, for all of your support and encouragement in this, and in all of my endeavors in life. I love you dearly.

Chapter 1, in full, is a reprint of the material as it appears in The Bulletin of the Seismological Society of America. Yin, H. Z., Xu, X., Haase, J. S., Douilly, R., Sandwell, D. T., and Mercier de Lepinay, B., Seismological Society of America, 2023. The dissertation author was the primary investigator and author of this paper.

VITA

2016	Bachelor of Science in Geophysics, University of Texas at Austin
2020	Master of Science in Earth Sciences, Scripps Institution of Oceanography, University of California San Diego
2024	Doctor of Philosophy in Earth Sciences, Scripps Institution of Oceanography, University of California San Diego

PUBLICATIONS

Yin, H. Z., Xu, X., Haase, J. S., Douilly, R., Sandwell, D. T., and Mercier de Lepinay, B. (2022). Surface Deformation Surrounding the 2021 M_w7.2 Haiti Earthquake Illuminated by InSAR Observations. The Bulletin of the Seismological Society of America, 113, 41–57. https://doi.org/10.1785/0120220109

ABSTRACT OF THE DISSERTATION

Satellite Observations and Dynamic Rupture Modeling of the 2021 Haiti Earthquake

by

Harriet Zoe Louisa Yin

Doctor of Philosophy in Earth Sciences

University of California San Diego, 2024

Jennifer S. Haase, Chair

The 2021 M_w7.2 Haiti earthquake led to more than 2200 deaths and struck just a decade after the devastating 2010 M_w7.0 earthquake which was one of the deadliest earthquakes on record globally. Both events occurred within a complex network of faults comprising the Enriquillo Plantain Garden Fault Zone (EPGFZ), which spans the southern peninsula of Haiti. Although the main Enriquillo Plantain Garden Fault (EPGF) has historically been assumed to be a near-vertical strike-slip fault that runs the length of the peninsula, neither the 2010 nor 2021 events had a simple strike-slip mechanism, nor did either clearly rupture this relatively simple and well-mapped fault within its assumed geometry. This event emphasizes the importance of understanding segmented fault behavior and strain partitioning in transpressive regimes and

raises new questions about how stress is distributed across the region. In this dissertation, we use a variety of observations and modeling tools to better understand this complex fault system.

In Chapter 1, we present satellite remote sensing observations of ground deformation during and after the 2021 rupture, illuminating postseismic slip to the east of the rupture and resolving triggered slip on secondary faults. In Chapter 2, we use 3D dynamic rupture modeling of this earthquake in order to test which conditions may have controlled the observed complex combination of dip-slip and strike-slip rupture across this transpressional fault zone. In Chapter 3, we use Coulomb Failure Stress analysis to test the hypothesis that Coulomb Failure Stress changes resolved onto secondary fault surfaces increased where there was observed shallow slip. These studies have led to improved understanding of seismic hazard in Haiti.

Chapter 1

Surface deformation surrounding the 2021 M_w7.2 Haiti earthquake illuminated by InSAR observations

1.1 Abstract

Earthquakes pose a major threat to the people of Haiti, as tragically shown by the catastrophic M7.0, 2010 earthquake and more recently by the M7.2 2021 earthquake. These events both occurred within the transpressional Enriquillo Plantain Garden Fault Zone (EPGFZ) which runs through the southern peninsula of Haiti and is a major source of seismic hazard for the region. Satellite-based InSAR (Interferometric Synthetic Aperture Radar) data is used to illuminate the ground deformation patterns associated with the 2021 event. The analysis of Sentinel-1 and ALOS-2 InSAR data shows 1) the broad coseismic deformation field; 2) detailed secondary fault structures as far as 12 km from the main Enriquillo Plantain Garden Fault (EPGF) which are active during and after the earthquake; and 3) postseismic shallow slip, which migrates along a $\sim$40 km unruptured section of the EPGF for approximately two weeks following the earthquake. The involvement of secondary faults in this rupture requires adjustments to the representation of hazard that assumes a simple segmented strike-slip EPGF. This work presents the first successful use of phase gradient techniques to map postseismic deformation in a vegetated region, which opens the door to future studies of a larger number of

events in a wider variety of climates.

1.2 Introduction

The Enriquillo Plantain Garden Fault Zone (EPGFZ) accommodates roughly half of the 20 mm/year of relative motion between the Caribbean plate and the North American plate (DeMets et al., 2000b) as the margin transitions from transform motion in the western Caribbean to subduction in the Antilles arc (Mann et al., 1995). Recent geodetic studies have shown slip rates of 9-10 mm/yr along the EPGFZ on the southern peninsula of Haiti with a largely left-lateral orientation and some compressional motion (S. J. Symithe & Calais, 2016; S. J. Symithe et al., 2015). There has been a recognized need to understand strain partitioning in this transpressional boundary following geodetic studies illustrating the interaction of offshore and onshore thrust systems with the main strike-slip strand of the fault zone, the EPGF, during the Holocene (Wang et al., 2018a). The geology and faults of the EPGFZ have been mapped in detail (Bien-Aime-Momplaisir et al., 1988a; Boisson, 1987), and more recent work has re-examined these maps to interpret the major active faults and their segmentation (Prentice et al., 2010b; Saint Fleur et al., 2020b; Wessels et al., 2019), which could be hypothesized to constrain the length of characteristic earthquake ruptures. The current seismic hazard maps constructed for Haiti were a major improvement over the previous global hazard maps (Frankel et al., 2011). The current maps estimate the seismic hazard from the major crustal faults including the strike slip Enriquillo-Plantain Garden fault in the south and Septentrional fault in the north, and the Transhaitian Belt (THB), a series of en enchelon fold and thrust faults north of Port-au-Prince. The maps include the contributions from the North Hispaniola Fault subduction boundary and the Muertos Trough subduction zone to the south (Fig 3.1). The EPGFZ was considered to be a single segment from the western limit of the 2010 rupture to the western coast of Haiti. Considering observations of the 2010 and 2021 earthquakes together can provide insight on rupture segmentation and could therefore play an important role in further refining the distribution of seismic hazard within the fault zone.

The Jan 12, 2010, earthquake occurred within the EPGFZ on the previously unmapped Léogâne blind thrust fault (Calais et al., 2010b; Mercier de Lepinay et al., 2011), with upward motion on the eastern part of the rupture in a direction opposite to that indicated by the regional topography (Hashimoto et al., 2011; Hayes et al., 2010). This upward motion resulted in up to 0.64 m of coastal uplift (Hayes et al., 2010) and 0.40 m of broad subsidence in the coastal mountain range (Hashimoto et al., 2011). A significant amount of triggered seismicity followed the main shock on the adjacent off-shore Trois Baies thrust fault (Douilly, Haase, Ellsworth, Bouin, Calais, Symithe, Armbruster, de Lepinay, et al., 2013b) (Fig 3.1). Coseismic static and kinematic slip models of the 2010 earthquake showed that the rupture propagated westward with two main slip patches, one with a major component of dip-slip in the east and another primarily with strike-slip in the west (Calais et al., 2010b; Meng et al., 2012; S. J. Symithe et al., 2013b). Calculations of the change in Coulomb Failure Stress (dCFS) from the coseismic slip showed a region of estimated stress increase collocated with aftershock observations to the west of the 2010 rupture on the Trois Baies fault and on the EPGF at depth. This suggested the possibility of higher hazard in these regions (S. J. Symithe et al., 2013b). Calculations of the cumulative stress changes from major historical events showed loading on adjacent fault segments over the course of several earthquake cycles (Ali et al., 2008b). Dynamic rupture modeling experiments for the 2010 earthquake explored the conditions that could explain the rupture pattern on the Léogane fault, without rupturing the main EPGF, nor the Trois Baies fault (Douilly et al., 2015b). It was found that variations in frictional properties were necessary for rupture to propagate from the eastern to western plane of the Léogane fault. However, the models suggest that the rupture did not jump to the Trois Baies and Enriquillo faults due to their orientations with respect to the Léogane fault. The interpretation of EPGFZ as a single, segmented strike-slip fault may therefore be oversimplified.

The Aug 14, 2021 $M_w 7.2$ earthquake did not rupture the segment identified with the highest dCFS following the 2010 event. Instead, it ruptured from the center of the Miragoâne-

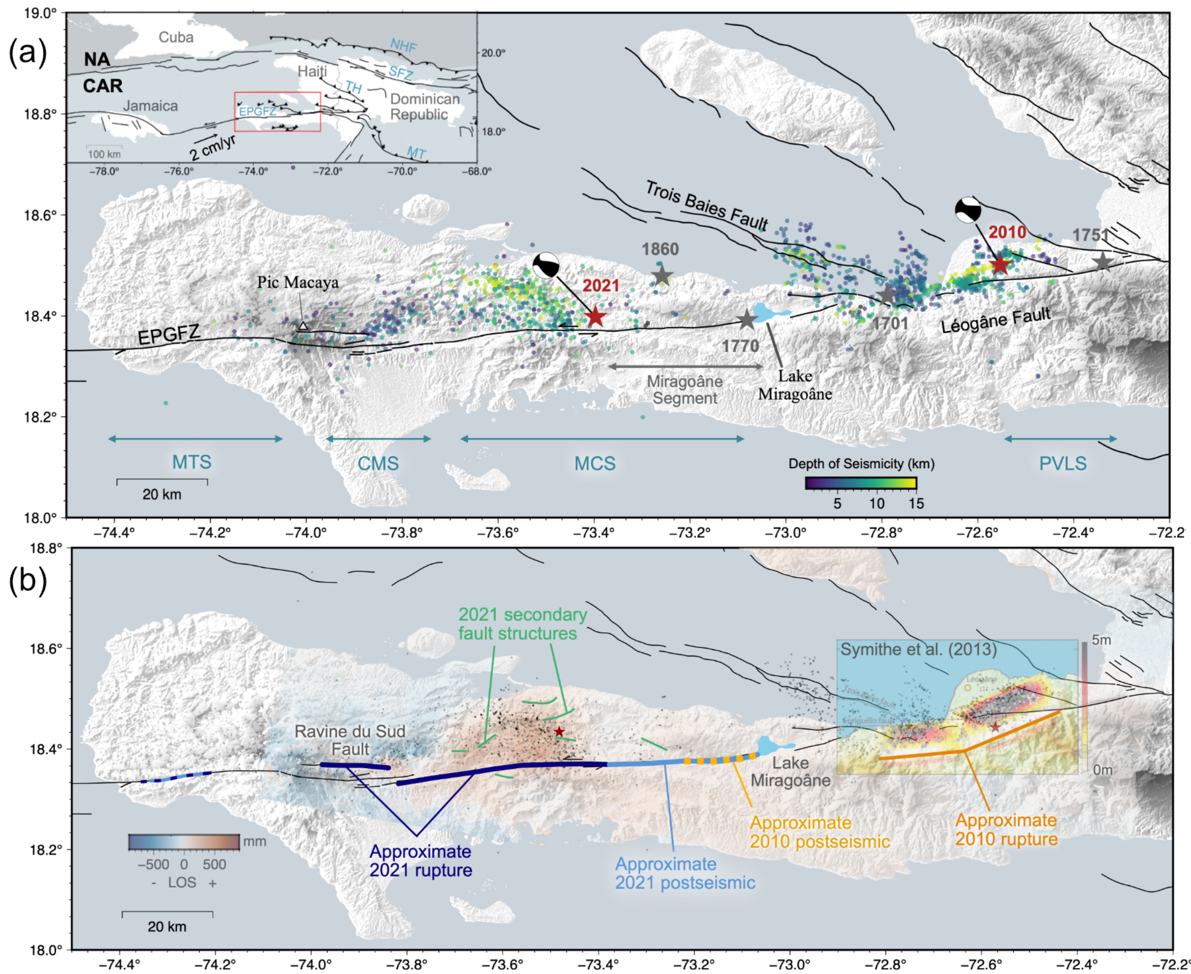

Figure 1.1. **(a)** Overview of the southern peninsula of Haiti, highlighting major geographic markers, fault zone locations, and historic earthquakes. Major historic earthquakes are marked by stars, with red stars highlighting the locations of the 2021 M7.2 and 2010 M7.0 epicenters with CMT moment tensor solutions. Aftershock locations are shown with circles, colored by event depths Calais, Symithe, Monfret, Delouis, Lomax, Courboulex, Ampuero, Lara, Bletery, Chèze, Peix, Deschamps, de Lépinay, et al. (2022a) and Douilly, Haase, Ellsworth, Bouin, Calais, Symithe, Armbruster, de Lepinay, et al. (2013b). Mapped EPGFZ faults (black lines) are from Saint Fleur et al. (2020b). Previously understood segmentation of the Enriquillo Plantain Garden Fault Zone from Saint Fleur et al. (2020b) is shown with horizontal blue arrows, and designates the Macaya-Tiburon Segment (MTS), Clonard-Macaya Segment (CMS), Miragoâne-Clonard Segment (MCS) and Pietonville-Léogane Segment (PVLS). The unruptured segment of the MCS is labeled as the Miragoâne segment. **(b)** Summary of faults active in the 2010 and 2021 ruptures. The approximate extents of the 2021 and 2010 co- and post-seismic slip features are shown with colored lines. Note that the north-dipping Leogane blind thrust fault is on the north side of the mapped EPGF that ruptured in 2010 S. J. Symithe et al. (2013b) but has a surface projection that appears on the south side of the EPGF (solid orange lines). The line-of-sight deformation from the descending ALOS-2 track D138 coseismic pair is overlaid for context, where the region of red indicates uplift.

Clonard Segment (MCS) and continued approximately 80 km westward (Fig 3.1). Aftershock locations for the 2021 M_w7.2 were calculated by the local network, Ayiti-Séismes, which includes the new RaspberryShake sensors that were deployed in local homes in a citizen science initiative (Calais, Symithe, Monfret, Delouis, Lomax, Courboulex, Ampuero, Lara, Bletery, Chèze, Peix, Deschamps, de Lépinay, et al., 2022a). The seismicity on the north side of the surface trace indicates that the fault is likely north dipping, although there are not yet clear planar features identified in the aftershok locations. Okuwaki and Fan (2022b) identified two distinct rupture episodes associated with this event, first rupturing a blind thrust fault in the east before jumping to a strike-slip fault westward. The aftershock distribution and back projection models both show that the two distinct ruptures were not contiguous (Calais, Symithe, Monfret, Delouis, Lomax, Courboulex, Ampuero, Lara, Bletery, Chèze, Peix, Deschamps, de Lépinay, et al., 2022a; Okuwaki & Fan, 2022b). InSAR data are consistent with a rupture dominated by left-lateral strike-slip motion in the west, and with dip slip motion in the east (Calais, Symithe, Monfret, Delouis, Lomax, Courboulex, Ampuero, Lara, Bletery, Chèze, Peix, Deschamps, de Lépinay, et al., 2022a; Maurer et al., 2022b). The rupture pattern of the 2021 event closely resembles that of the 2010 earthquake and suggests that the accommodation of compression along this boundary may play a major role in strain partitioning. Neither earthquake ruptured the intervening Miragoâne segment between the two event rupture planes, raising the question of whether this segment is seismically loaded or if it is accommodating strain in some other way. Observations of this complex rupture sequence are therefore highly relevant for both improving our understanding of seismic hazard in Haiti and in transpressive strike-slip margins in general.

1.3 Data

Two InSAR satellite missions were operational at the time of the 2021 event: Sentinel-1 twin satellites operated by the European Space Agency (ESA) and ALOS-2 operated by the Japanese Aerospace Exploration Agency (JAXA). Both InSAR data sets are used to generate

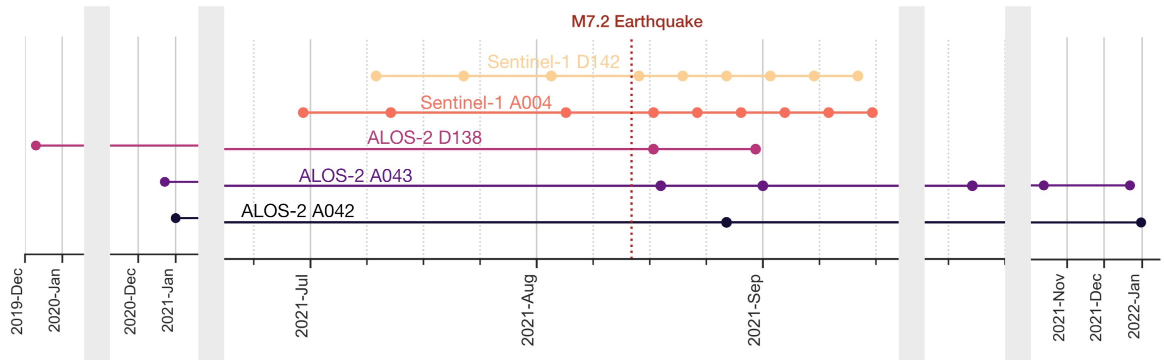

Figure 1.2. Timeline of all SAR scene acquisitions used in this work with the vertical red dashed line marking the Aug 14 earthquake. Sentinel-1 acquisitions are frequent, with ascending and descending acquisitions less than two weeks before the 2021 earthquake. In contrast, ALOS-2 acquisitions are infrequent, with the closest usable ALOS-2 acquisitions prior to the earthquake more than 6 months before the earthquake. Note the breaks in the horizontal axis in grey which represent large time periods between ALOS-2 acquisitions.

interferograms and derived products for this study. InSAR interferograms are formed using the difference in radar return phase between two satellite passes, with fringes representing small, coherent deformation of the Earth surface in the line-of-sight (LOS) of the radar. After unwrapping, these interferograms provide a broad view of surface deformation between two SAR acquisitions. Ascending and descending passes provide two unique look angles over the region which constrain the total deformation. The east-west trend of the EPGF and roughly east-west look angles of ascending and descending InSAR satellite passes for both missions in this region align fortuitously, making InSAR observations especially sensitive to fault-parallel motion, which is of the greatest interest. These InSAR missions have complementary strengths and limitations. In particular, we are concerned with radar wavelength, acquisition mode, and repeat acquisition times.

The longer ALOS-2 wavelength (L-band, 22.9 cm wavelength) makes it more resistant to decorrelation due to vegetation than the shorter Sentinel-1 wavelength (C-band, 5.5 cm wavelength), which is a major concern in tropical Haiti. Each satellite instrument can operate in a variety of acquisition modes, each with a corresponding swath footprint and resolution. The ALOS-2 repeat descending passes which cover this event are in the lower resolution ScanSAR mode (350 x 350 km swaths, with roughly 100 m resolution), while the repeat ALOS-2 ascending passes are in the higher resolution strip map mode (30 x 30 km swaths, with roughly 4 x 8 m resolution). Sentinel-1 acquisitions used in this study are in Interferometric Wideswath (IW) mode (250 km wide swaths, with 3 x 22 m resolution). ALOS-2 routine acquisitions are infrequent over Haiti, with the closest ALOS-2 repeat passes occurring more than six months prior to the earthquake for ascending passes and more than a year prior to the earthquake for descending passes (Fig 1.2). Sentinel-1 acquisitions in this region are generally frequent and regular, with repeat times of 6-12 days. This short temporal baseline in Sentinel-1 data relative to ALOS-2, would generally reduce phase decorrelation due to changes in the land surface properties between acquisitions. However, in this case there is a trade-off between the increased susceptibility to vegetation of Sentinel data and its more frequent acquisitions. When combined, Sentinel-1 and ALOS-2 data have the capability to illuminate small, rapidly changing signals like post-seismic slip while also capturing a high resolution deformation field and mitigating interference from vegetation.

1.4 Methods

We compile Sentinel-1 and ALOS-2 repeat acquisitions surrounding the time of the 2021 earthquake and use GMTSAR software to process the raw data (Sandwell et al., 2011; Wessel et al., 2013; Xu et al., 2017). Interferograms are Gaussian filtered at 200 m and re-sampled at 50 m before further processing. We unwrap the phase using the Statistical-Cost, Network-Flow Algorithm for Phase Unwrapping (SNAPHU) (Chen & Zebker, 2002), with nearest neighbor interpolation over the low coherence areas and water surfaces (Shanker & Zebker, 2009). The resulting LOS plots (Fig 1.3) show surface deformation in the line-of-sight of the observing satellite, where a positive LOS value indicates that the ground pixel has moved towards the satellite. Phase unwrapping is generally a non-unique process and requires parameter choices which affect the resulting LOS solution. These choices include phase filtering wavelength (applied prior to unwrapping), the minimum coherence threshold for pixels to be included in unwrapping, whether and how broadly to interpolate over low-coherence areas, and the maximum phase discontinuity that the unwrapping algorithm can assign. These parameters are calibrated by trial and error to minimize visually-identifiable unwrapping errors in resulting LOS plots. The sensitivity of the unwrapping results to these parameter changes can be an indicator of the reliability of the data for unwrapping.

1.4.1 Phase Unwrapping Reliability

Phase unwrapping of ALOS-2 data is more reliable than Sentinel-1 data due to its longer radar wavelength, enabling superior coherence. The region near the rupture in the Sentinel-1 coseismic interferograms could not be reliably unwrapped, likely due to extreme ground shaking near the fault and decorrelation due to vegetation. The unwrapping errors produced by Sentinel-1 coseismic pairs are illustrated in Fig 1.3 which shows a comparison between three unwrapping approaches used on the same Sentinel-1 ascending coseismic pair (Fig 1.3b-d) versus the closest-equivalent ALOS-2 ascending coseismic pair (Fig 1.3a). Figure 3a shows two overlapping, ascending ALOS-2 coseismic pairs in stripmap mode: A043, spanning Dec 23, 2020-Aug 18, 2021 and A042, spanning Jan 1 - Aug 22, 2021. These pairs are unwrapped allowing a 15 phase cycle (1.72m) discontinuity and interpolating regions with coherence below 0.1 over the nearest 300 pixels. The corresponding cross-sections show a smooth deformation pattern which is continuous across the mapped EPGF and has a maximum change across the fault of around 700 mm in the LOS direction. Both pairs cover the transect location and the similarity in unwrapped LOS solutions shown in the bottom panel of Figure 3a is a indicator that the unwrapping solutions are reliable. There are no clear signs of unwrapping errors and the coherence is generally good, which supports the interpretation that this unwrapping solution is close to the true deformation field.

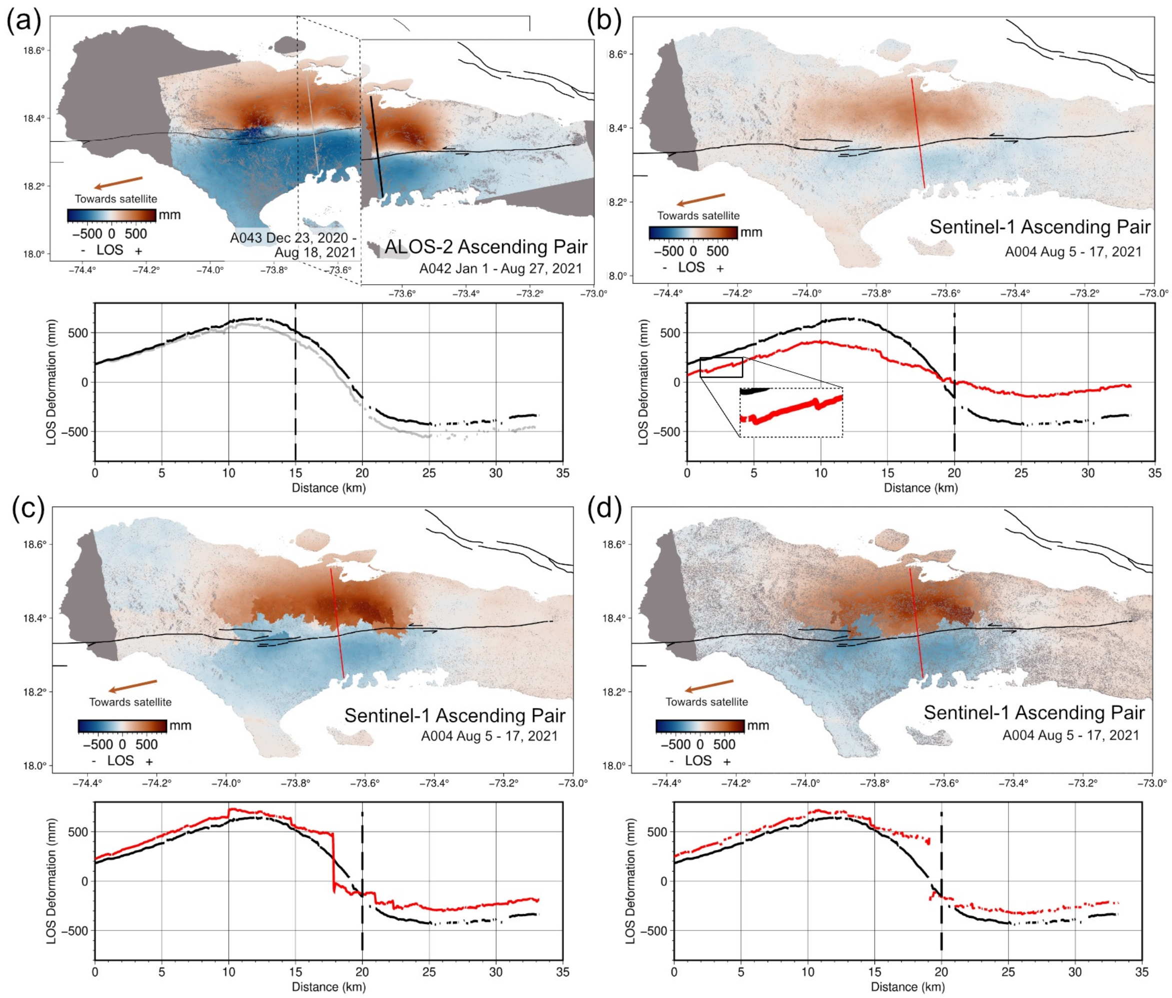

Figure 1.3. A comparison of ascending coseismic pairs unwrapped with different parameters. For each panel, the top inset shows the unwrapped LOS solution with a transect plotted perpendicular to the mapped EPGF (black). The bottom inset shows the corresponding LOS values along the transects plotted in gray, black, or red. The location of the main strand of the mapped EPGF (Saint Fleur et al., 2020b) is shown with the dashed vertical black lines in the cross-sections. Panel (a) shows overlapping ascending ALOS-2 coseismic pairs in stripmap mode: A043, spanning Dec 23, 2020-Aug 18, 2021 and A042, spanning Jan 1 - Aug 22, 2021. Panels (b-d) show the Sentinel-1 ascending track A004 coseismic pair spanning Aug 5-17, unwrapped using varying parameters. The ALOS-2 A042 LOS transect is shown in black in the panel (b-d) cross sections for comparison.

Figure 3b-d show three unique unwrapping solutions for the closest equivalent Sentinel-1 ascending coseismic pair spanning Aug 5-17, 2021. Figure 3b shows the pair unwrapped allowing no discontinuity and interpolating regions with coherence poorer than 0.06 over the nearest 300 pixels. The corresponding cross-section below shows a smoothed pattern of deformation with a maximum LOS deformation of about 400 mm, far below the ALOS-2 maximum deformation. This underestimation of maximum LOS deformation can be attributed to missed phase jumps, highlighted in the exploded view of Figure 3b. This illustrates that visual smoothness does not equate to a reliable unwrapping solution. Figure 3c shows the same pair with the same interpolation coherence threshold as Figure 3b, but unwrapped allowing an 80 cycle (about 2.22m) discontinuity. The corresponding transect has many more phase jumps, due to the larger discontinuity allowance, with a maximum LOS deformation of about 750 mm, comparable to that of the ALOS-2 pair. This LOS plot contains phase unwrapping errors, seen as the irregular southern edge of the red region, which obscures the pattern of deformation near the mapped EPGF. Figure 3d shows the pair unwrapped allowing an 80 cycle (about 2.22m) discontinuity and interpolating regions with coherence below 0.1 over all pixels. The corresponding transect shows a smoother pattern of deformation than Figure 3c, with a maximum LOS of about 750 mm, but with a large discontinuity near the mapped EPGF and some unwrapping errors persisting on the eastern and western portions of the main rupture.

The comparison among the LOS solutions using varying unwrapping criteria (Fig 3) illustrates the limitations of Sentinel-1 data for deducing the amplitude of the broad coseismic deformation pattern of this earthquake, where there is a trade-off between the amplitude of the LOS deformation and thresholds for phase cycle discontinuities and coherence. Maurer et al. (2022b) suggested that a possible explanation for significantly higher amplitude of the ALOS-2 A043 coseismic interferogram than the Sentinel-1 interferogram was that there was a significant amount of aseismic slip after the Sentinel-1 descending acquisition on Aug 15 but before the ALOS-2 A043 acquisition on Aug 17, that could be explained by an additional postseismic moment release equivalent to an M_w6.8. We find that although there is evidence of postseismic shallow slip after Aug 15, there is a lack of a clear, broad deformation signal in subsequent Sentinel-1 pairs spanning Aug 15 - 21 (D142) and Aug 17 - 23 (A004), which we would expect to capture any significant postseismic moment release (Fig S1). Calais, Symithe, Monfret, Delouis, Lomax, Courboulex, Ampuero, Lara, Bletery, Chèze, Peix, Deschamps, de Lépinay, et al. (2022a) used InSAR data in their modeling, and observed high uncertainty in the near-fault region of the closest earthquake-spanning Sentinel-1 LOS observations. They chose to mask those values (to around 10 km north of the EPGF). The variability of Sentinel-1 unwrapping results in our analysis is consistent with this approach, and this unwrapping uncertainty could explain the difference in deformation amplitude between Sentinel-1 and ALOS-2 coseismic pairs. Therefore, we assume that ALOS-2 unwrapping results are more reliable for understanding the true LOS deformation, so we use only ALOS-2 pairs for broad coseismic deformation pattern analysis and interpretations of surface rupture. We primarily use Sentinel-1 results to resolve postseismic creep on faults.

1.4.2 Phase Gradient Analysis

Phase unwrapping is a useful technique for estimating the broad surface deformation pattern in response to a rupture. However, the large amplitude broad deformation field may obscure small-scale deformation features with smaller amplitudes. In contrast, calculating the interferometric phase gradient directly from the unfiltered, full resolution interferogram (Sandwell & Price, 1998) highlights sharp changes in radar phase, amplifying the appearance of small-scale deformation features. Given the expression for interferometric phase at location, x, in terms of the real (R) and imaginary (I) components of the complex interferogram:

$$\phi(x) = tan^{-1}\left(\frac{I}{R}\right) \tag{1.1}$$

we can then use the chain rule to derive an expression for the phase gradient in terms of R and I:

$$\nabla\phi(x) = \frac{R\nabla I - I\nabla R}{R^2 + I^2} \tag{1.2}$$

where $\nabla = \frac{\partial}{\partial r}, \frac{\partial}{\partial a}$, a is the azimuth (flight) direction, and r is the range (look) direction in radar coordinates (Sandwell & Price, 1998; Xu, Sandwell, Ward, et al., 2020b).

This approach avoids the need for phase unwrapping and the solution can be stacked directly to enhance the signal to noise ratio. This is important because taking the gradient amplifies noise in the interferogram. We apply a square Gaussian filter with a large wavelength (200 m) to the phase gradient product in order to suppress noise. We take the gradient in both the azimuth (flight) and range (look) directions but find that the gradient in the azimuth direction tends to resolve features more clearly, likely because most active features are aligned more closely to the range direction than to the azimuth direction. Phase gradients calculated in the range direction are shown in Supplemental Figure S2 and do not reveal any new features. The offset direction of phase gradient features cannot be interpreted directly from phase gradient plots. Instead, corresponding LOS images are used to guide the interpretation. Phase gradient features are largely unresolvable from Sentinel-1 interferograms, even after stacking a large number of interferograms (Fig S3). This is likely due to the higher noise from phase decorrelation due to vegetation, which is then amplified by the phase gradient calculation. However, interferograms from ALOS-2 ascending tracks A043 and A042 which are in stripmap mode have excellent coherence and resolution, rendering clear linear features in the resulting phase gradient plots.

1.5 Results

The complete set of InSAR products from Sentinel-1 and ALOS-2 were examined for evidence of slip surrounding the main rupture zone. This dataset is openly available for download (Yin, Xu, Haase, Douilly, Sandwell, & Mercier de Lépinay, 2022). We describe three categories of observed surface deformation features in the following section: 1) broad coseismic

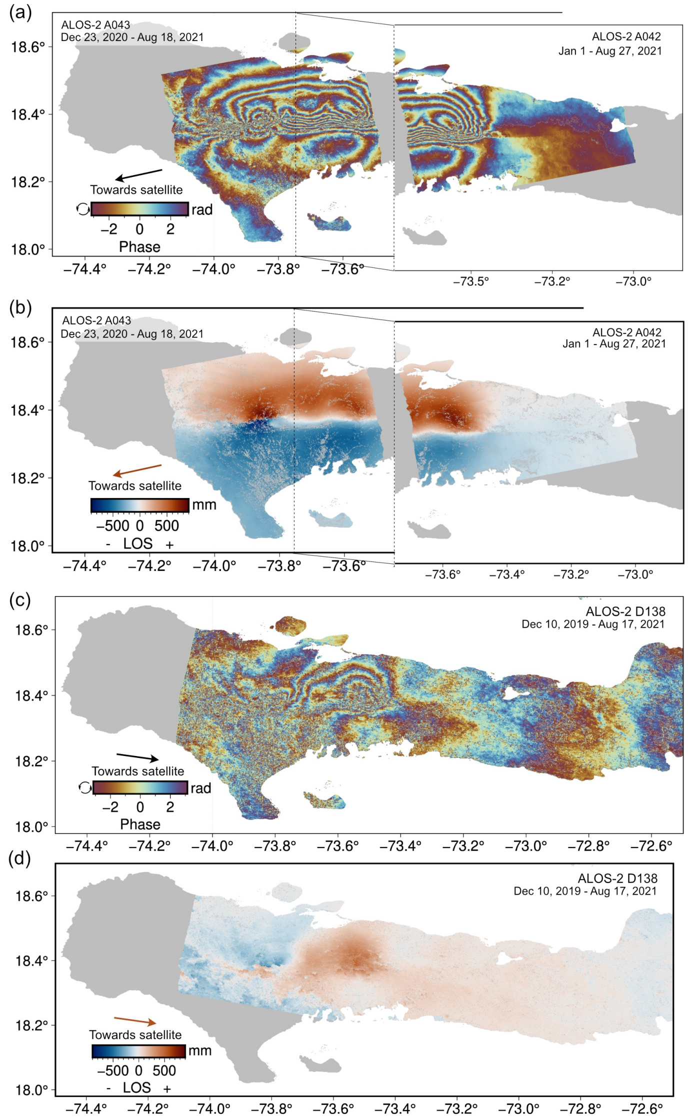

Figure 1.4. ALOS-2 ascending and descending coseismic pairs shown as wrapped phase and unwrapped LOS deformation. (a) ALOS-2 wrapped phase in stripmap mode from the coseismic pairs for ascending track A043 (left, Dec 23, 2020 to Aug 18, 2021) and ascending track A042 (right, Jan 1 - Aug 27, 2021); (b) Unwrapped phase, converted to LOS deformation for A042 and A043 coseismic pairs. Red represents positive motion of the ground surface in the direction of the arrow, and shows a deformation pattern dominated by left-lateral strike slip motion; (c)ALOS-2 wrapped phase in ScanSAR mode from the coseismic pair (Dec 10, 2019 to Aug 18, 2021) for descending track D138; (d) Unwrapped phase, converted to LOS deformation for the D138 coseismic pair. The red lobe to the east indicates a region of significant uplift while the western lobe of deformation continues to be dominated by left lateral deformation.

deformation pattern; 2) postseismic slip on the mapped EPGF adjacent to the main rupture; and 3) slip on secondary fault features off of the mapped EPGF.

1.5.1 Broad Coseismic Deformation

The broad coseismic deformation pattern of the 2021 earthquake is illuminated by earthquake-spanning interferograms from the ascending and descending ALOS-2 coseismic pairs shown in Fig 1.4. Fig 1.4a and 1.4b show overlapping ascending ALOS-2 tracks A043 (left, Dec 23, 2020 - Aug 18, 2021) and A042 (right, Jan 1 - Aug 27, 2021) acquired in stripmap mode spanning the earthquake. Fig 1.4a shows the wrapped phase with fringes converging near the mapped EPGF, indicating deformation caused by the main rupture. Fig 1.4b shows the unwrapped line-of-sight (LOS) deformation, with red indicating motion up and to the west extending from approximately 74°W to 73.4°W. Fig 1.4c and 1.4d show the descending pair (track D138), acquired in ScanSAR mode, spanning Dec 10, 2019 - Aug 18, 2022, which are the closest acquisitions before and after the earthquake. LOS deformation in Fig 1.4d shows a region of red, indicating motion up and to the east confined to the eastern portion of the rupture, which is consistent with dip slip motion. This observation agrees with the moment tensor solution for the event which shows strike slip motion with a component of dip slip (USGS, 2021), other finite fault rupture solutions (Calais, Symithe, Monfret, Delouis, Lomax, Courboulex, Ampuero, Lara, Bletery, Chèze, Peix, Deschamps, de Lépinay, et al., 2022a; Maurer et al., 2022b), and back projection estimates (Okuwaki & Fan, 2022b).

The coseismic LOS plots show a smooth transition from red to blue, across the EPGF, through most of the central and eastern rupture (from approximately $-73.8°$ to $-73.5°$) . This smooth transition indicates that the rupture likely did not reach the surface through this section. However, in the western portion of the rupture zone, there is a sharp transition from dark red to dark blue in both ascending and descending LOS plots (from approximately $-74.0°$ to $-73.8°$), suggesting surface rupture in this area. This surface rupture coincides with the mapped Ravine du Sud fault, indicating that this fault was active during the earthquake.

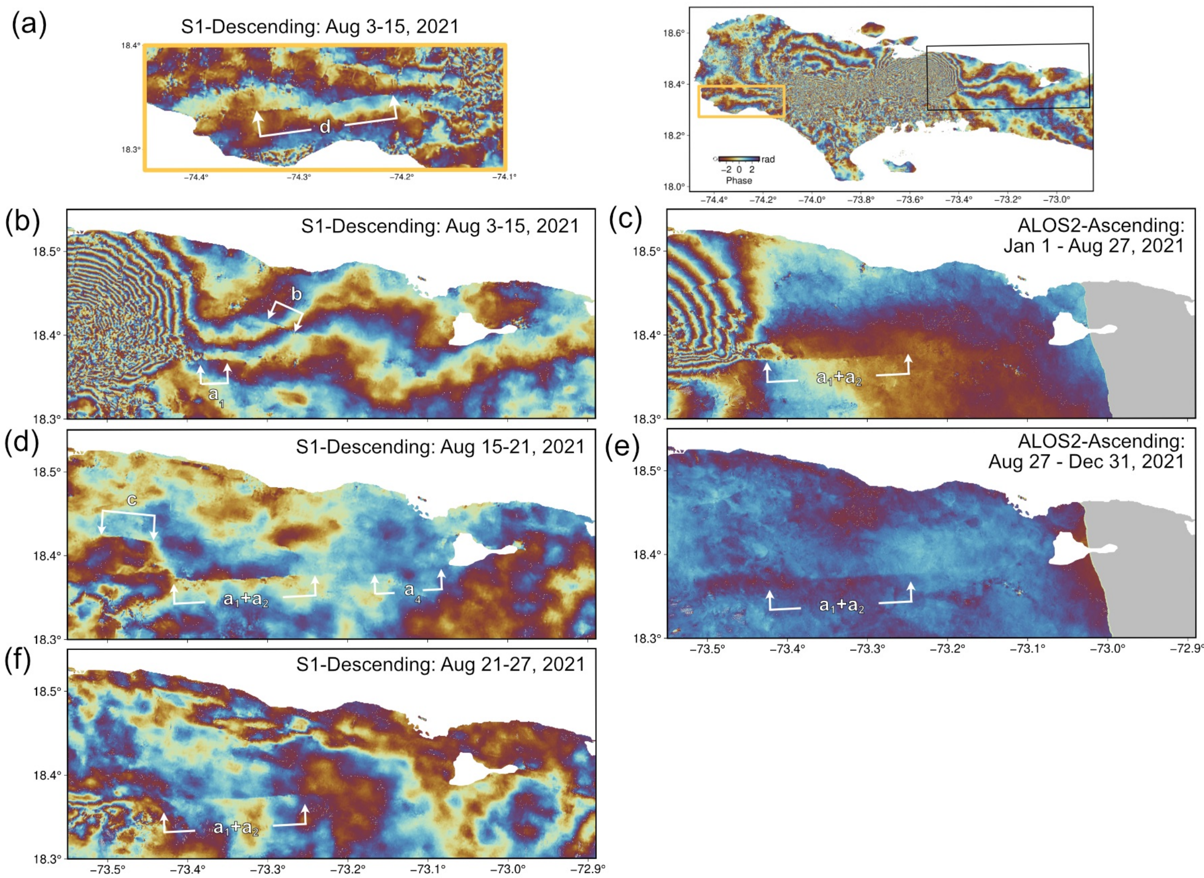

Figure 1.5. Consecutive pairs of Sentinel-1 descending track D142 and ALOS-2 ascending track A042 wrapped phase. Truncated phase features are highlighted with white arrows and indicate possible postseismic deformation. (a) Sentinel-1 descending track D142 Aug 3-15 pair zoomed to the orange outlined area to the west of the main rupture, Feature *d* is identified extending west of the main rupture; (b) Sentinel-1 descending track D142 Aug 3-15 pair zoomed to the black outlined area to the east of the main rupture; (c) ALOS-2 ascending track A042 Jan 1 - Aug 27, 2021 pair; (d) Sentinel-1 descending track D142 Aug 15-21 pair; (e) ALOS-2 ascending track A042 Aug 27 - Dec 31, 2021 pair. (f) Sentinel-1 descending track D142 Aug 21-27 pair.

1.5.2 Postseismic slip on the EPGF

Postseismic slip on the order of $\sim$2 cm occurred on the mapped EPGF to the east of the main rupture in the two weeks following the earthquake. The propagation of slip was captured by consecutive Sentinel-1 and ALOS-2 pairs, seen as offsets in the wrapped phase interferograms in Fig 1.5, where offsets indicate surface deformation. We use a perceptually uniform and cyclic color palette (romaO) to plot wrapped phase to reduce bias in the identification of features (Crameri et al., 2020). More confidence was given to features that appeared in both wrapped interferograms and phase gradient plots, that appeared in multiple interferogram pairs, and have more than $\sim$ 7 mm of offset in the wrapped phase images.

Fig 1.5b shows Sentinel-1 descending track D142 Aug 3 - 15 pair, which is dominated by the coseismic deformation signal from the main shock, seen as concentric curved fringes. However, to the east of that coseismic deformation pattern, feature a_1 is identified with a length of approximately 5 km where the fringes are offset. It is possible that this phase offset occurred as part of the coseismic rupture. However, another explanation is that postseismic slip occurred on a_1 in the day following the earthquake (i.e. before the second Sentinel-1 pass on Aug 15). This interpretation is supported by evidence of continued slip on feature a in the following InSAR pairs. In addition to slip on the mapped EPGF, a secondary feature b is identified in this pair to the north of the EPGF, but no further slip is observed on this segment in subsequent pairs. Fig 1.5a identifies feature d in the same coseismic pair (Aug 3 - 15, 2021), but to the west of the main rupture on the mapped EPGF. Feature d has a length of approximately 8km and does not appear in any subsequent pairs, so it could reasonably have occurred during the earthquake as coseismic slip, as is attributed by Maurer et al. (2022b), or in the day after the earthquake as postseismic slip. Because this feature is observed only in this coseismic pair, its extent and timing are less certain than that of feature a.

Fig 1.5d shows the Sentinel-1 descending track D142 Aug 15-21 pair for the following time period, where the feature identified in Fig 1.5b persists on a_1 and extends an extra $\sim$10 km to the east, identified in the figure as feature $a_1 + a_2$. This is clearly interpretable as postseismic slip, with an approximate maximum offset of 18 mm identified in the LOS direction across the fault. There appears to be a gap (unlabeled segment a_3) between slip on $a_1 + a_2$ and slip on feature a_4 which abuts Lake Miragoâne. In addition we identify a ~ 5 km secondary fault feature c that shows postseismic slip also occurring off of the main fault, with an orientation similar to segment b. Fig 1.5f shows Sentinel-1 descending track D142 Aug 21-27 pair, where slip continues along $a_1 + a_2$ but is no longer visible on a_4. No deformation is observed in the subsequent pairs of this Sentinel-1 descending track.

Fig 1.5c shows ALOS-2 ascending track A042 Jan 1-Aug 27 pair, which covers the same time period as Fig 1.5b, d, f combined. The direction of phase offsets in both the ascending and descending images of feature a indicates that the motion on feature a is primarily left-lateral, in the direction of the prevailing tectonic motion. Cumulatively, feature a persists for roughly 50 km to the east of the main rupture and is active for approximately two weeks following the earthquake. For each of these identified features, the slip is likely constrained to a very shallow portion of the crust because there is no broader deformation pattern associated with it.

Fig 1.5e shows ALOS-2 ascending track A042 pair spanning Aug 27-Dec 31. This pair shows a small amount of offset on $a_1 + a_2$ which accumulates after Aug 27. However, no slip is observed in Sentinel-1 pairs after Aug 27. Therefore, a possible interpretation is that the slip shown in Fig 1.5f accrued on Aug 27, just after the ALOS-2 Aug 27 acquisition. The Aug 27 ALOS-2 acquisition occurred before the Aug 27 Sentinel-1 acquisition, which is consistent with this interpretation.

1.5.3 Slip on secondary faults

Phase gradient plots highlight areas of discrete offsets in the phase, without the need for phase unwrapping. Linear features are identified by sharp changes from the background grey to bright or dark. Phase gradient features indicate high positive or negative gradient in areas of concentrated deformation or higher strain. Fig 1.6 shows stacked phase gradient values for

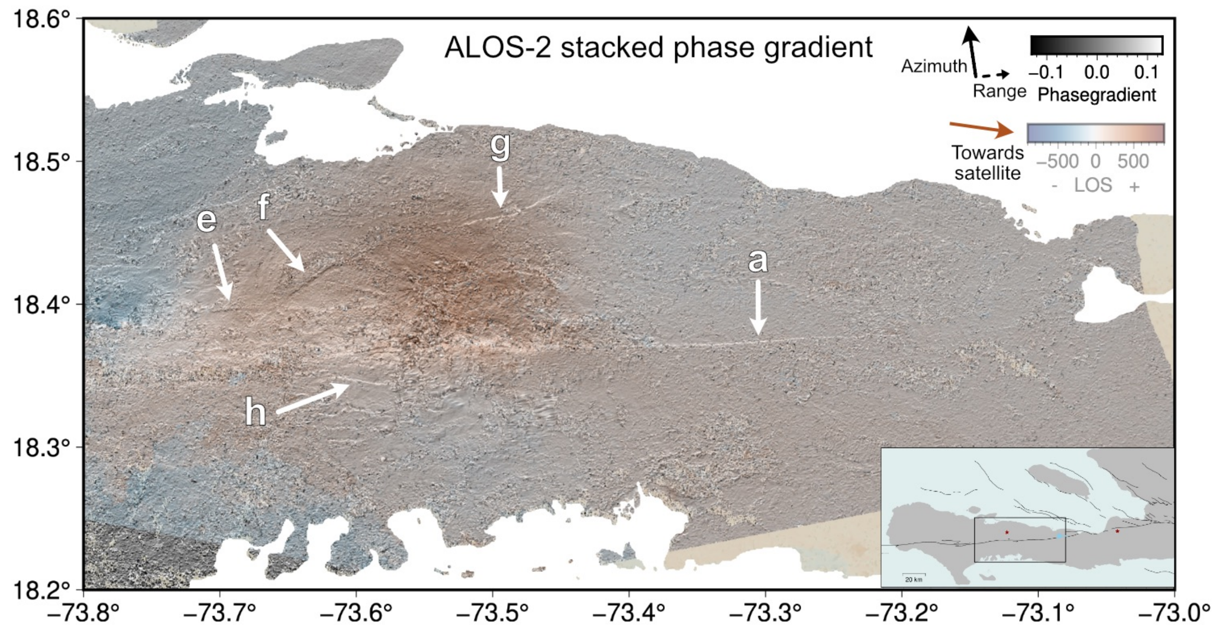

Figure 1.6. Stacked phase gradient of the interferometric phase taken in the azimuth (flight) direction. This stack sums the phase gradient from all ALOS-2 ascending track pairs between Dec 23, 2020 and Dec 31, 2021 (3 pairs for A042 and 5 pairs for A043). The phase gradient is overlain with the LOS plot from ALOS-2 pair D138 for context. The most apparent linear features are labeled *a* and *e*-*h*. Feature *a* is also observed as left-lateral slip in wrapped phase interferograms (Fig 1.5).

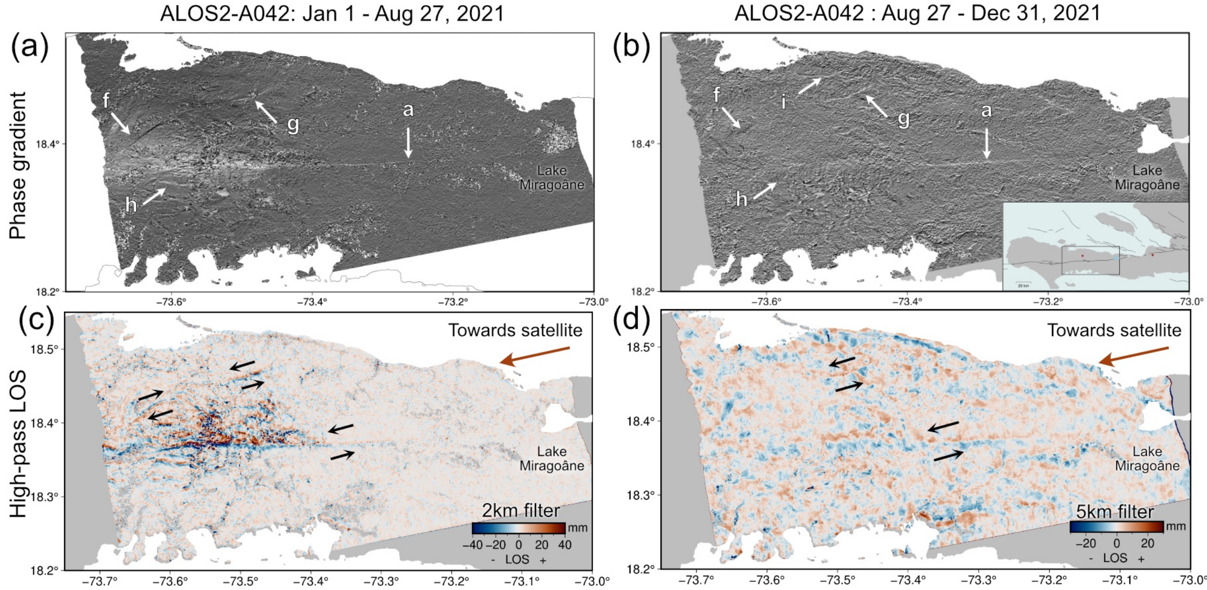

Figure 1.7. ALOS-2 ascending track 042 coseismic (left, Jan 1 - Aug 27, 2021) and postseismic (right, Aug 27 - Dec 31, 2021) pairs. Each pair is shown as phase gradient calculated in the azimuth direction (top), and high-pass filtered LOS deformation (bottom) to highlight tbe sense of motion on these smaller features. Features are labeled in white and the corresponding sense of motion on these features, if detectable, is indicated with black arrows on the LOS plots, below. (c) is high-pass filtered with a 2 km Gaussian filter and shows the northern side of the feature moving away from the satellite (relative to the southern side) on feature f and towards the satellite on feature g; (d) is high-pass filtered with a 5 km Gaussian filter and shows the same sense of motion on features g and a but sense of motion is unclear on feature f.

ALOS-2 ascending track A042 and A043 pairs. This figure contains phase gradient results for all pair combinations between Dec 23, 2020 to Dec 31, 2021 (3 pairs for A042 and 5 pairs for A043), calculated in the azimuth (flight) direction, and then summed to amplify the magnitude of phase gradient values in features appearing in multiple images above the random background noise. Deformation from the main rupture appears as a diffuse bright area surrounding the trace of the fault, generally without abrupt changes because the rupture did not reach the surface along most of the fault.

Five main features are identified based on the stacked phase gradient plot (Fig 1.6, labeled $a-h$). Feature a is identified east of the main rupture, confirming the wrapped phase analysis of postseismic slip on the EPGF, as discussed in the previous section. Features f and g are the clearest of the phase gradient features. They are identified as two separate features but could be viewed as a continuous feature that changes slowly from white (g) to black (f). Features e and h are identified less clearly than features f and g and run subparallel to the EPGF. Other subparallel lines above and below these features could reasonably be identified as features in addition to e and h. However, we limit our discussion to the labeled features which are the most visually apparent and appear in multiple products.

After features are identified in the stacked plot, further inspection of the individual pairs gives clues about when these features were active. Fig 1.7 shows coseismic (Jan 1 - Aug 27, 2021) and postseismic (Aug 27 - Dec 31, 2021) ascending ALOS-2 pairs, each with phase gradient calculated in the azimuth direction and a high-pass filtered LOS deformation plot to interpret the sense of motion on these smaller features. Features f, g, h and a are easily identified in the coseismic pair (Fig 1.7a). However, features f, g, and a can also be identified in the postseismic time period (Fig 1.7b), at least through Aug 27, 2021. In Fig 1.7b, we also identify an additional feature, i, which appears north of feature g, but with a similar curved shape. This feature is only identified in the Aug 27 - Dec 31, 2021 pair, suggesting that this feature is only active in the postseismic period. High-pass filtered LOS plots (Fig 7c-d) are used to interpret the sense of motion on each of these features. Fig 1.7c shows the northern side of the feature moving away from the satellite (relative to the southern side) on feature f, but towards the satellite on feature g. Fig 1.7d shows the same sense of motion on features g and a but the sense of motion is unclear on feature f. The motion on f is opposite to that on g, but the absolute sense of motion cannot be constrained from ascending pairs alone and the phase gradient calculations for the corresponding descending ALOS-2 and Sentinel-1 pairs were not able to resolve these features due to poorer resolution and higher noise, respectively.

1.5.4 Slip following the Jan 12, 2010 earthquake

Postseismic slip was reported after the Jan 12, 2010 earthquake (Wdowinski & Hong, 2011). We reprocessed ALOS-1 data from 2010 to confirm this postseismic deformation and to

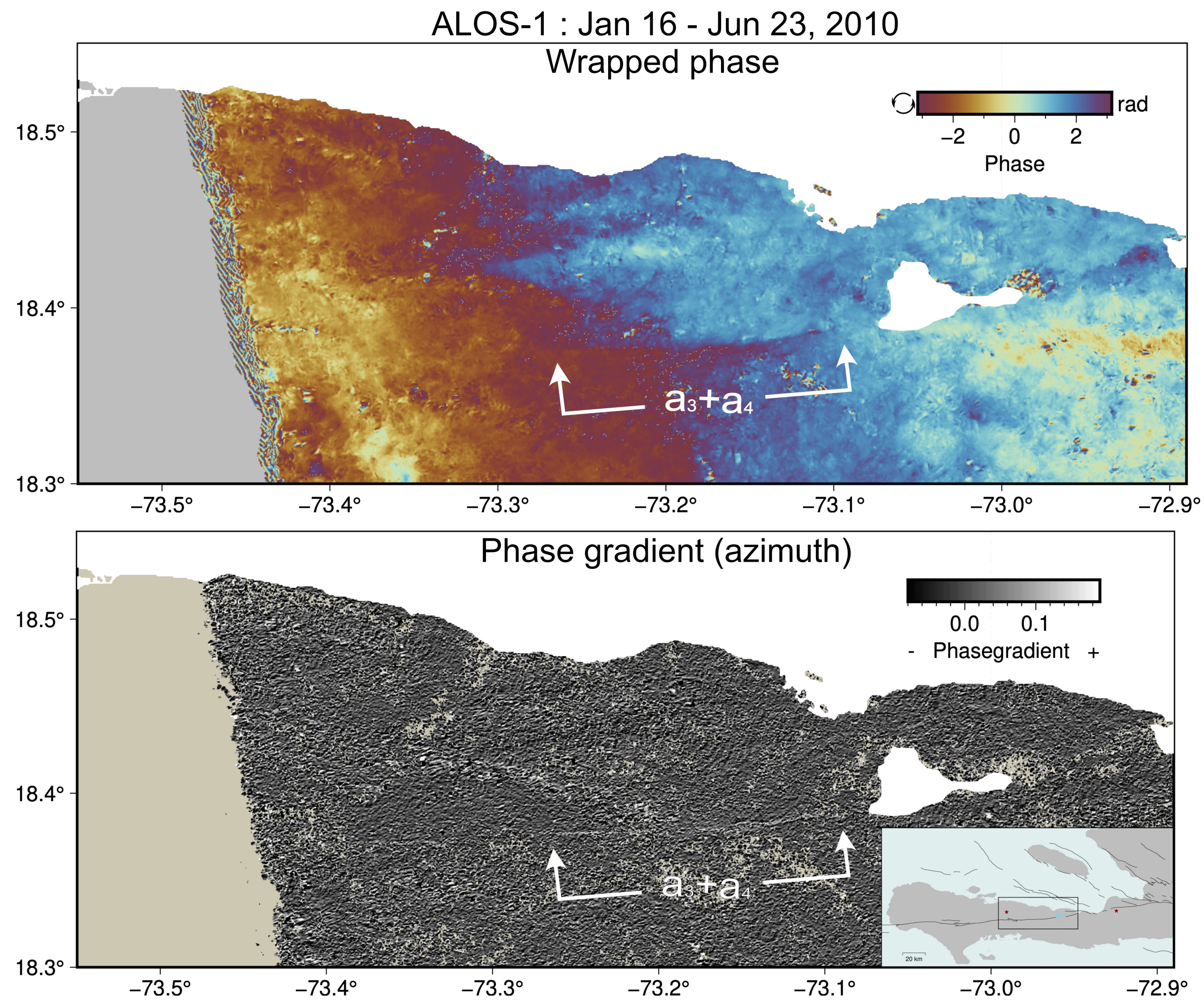

Figure 1.8. Postseismic deformation following the 2010 earthquake using ALOS-1 InSAR pair spanning Jan 16 -Jun 3, 2010. (a) Wrapped phase filtered at 200 m, postseismic offset indicated by black arrows; (b) phase gradient in the azimuth direction, postseismic offset indicated by white arrows.

determine its location relative to the 2021 postseismic slip. The wrapped phase from the ALOS-1 postseismic pair spanning Jan 16 - Jun 3, 2010, shows a pattern of postseismic deformation on the mapped EPGF directly west of Lake Miragoâne. The phase gradient calculation in the azimuth direction illuminates linear feature a, indicating concentrated strain on the same feature where postseismic slip is observed following the 2021 earthquake (Fig 1.8). While slip is not identified on the a_3 segment following the 2021 event, slip is detected on the a_3 segment following the 2010 event, on a segment totaling $\sim$17 km. The 2010 postseismic deformation was observed between Jan 16, 2010 (4 days after the earthquake) and Jun 3, 2010. The timing of this slip cannot be further constrained within this period. No postseismic deformation is observed in the subsequent ALOS-1 pair (Jun 3 - Jul 19, 2010). Similar to the postseismic deformation following the 2021 earthquake, the 2010 postseismic deformation on the EPGF decays within 1-2 km of the fault, suggesting that this slip is also very shallow.

1.6 Discussion

Taken together, InSAR observations surrounding the 2021 earthquake expose the evolution of deformation in the broader EPGFZ during and after the event. Observations of the broad coseismic deformation field are consistent with two broad zones of deformation: one to the west with pure left-lateral strike slip motion and one to the east with a significant component of dip-slip motion. The maximum LOS deformation is $\sim$1 m. We find strong evidence for surface rupture with offsets of $\sim$1.5 m in the LOS direction on the western portion of the segment on the mapped Ravine du Sud fault. Wrapped phase and phase gradient analysis shows postseismic left-lateral offsets on the order of $\sim$2 cm in the LOS direction on the mapped EPGF to the east of the main rupture. This feature is active for $\sim$2 weeks following the mainshock. There is evidence for similar postseismic deformation on this same segment of the EPGF following the 2010 earthquake, occurring at least four days after the earthquake, although the timing of this slip is less well-constrained. Finally, there is extensive evidence for the involvement of secondary

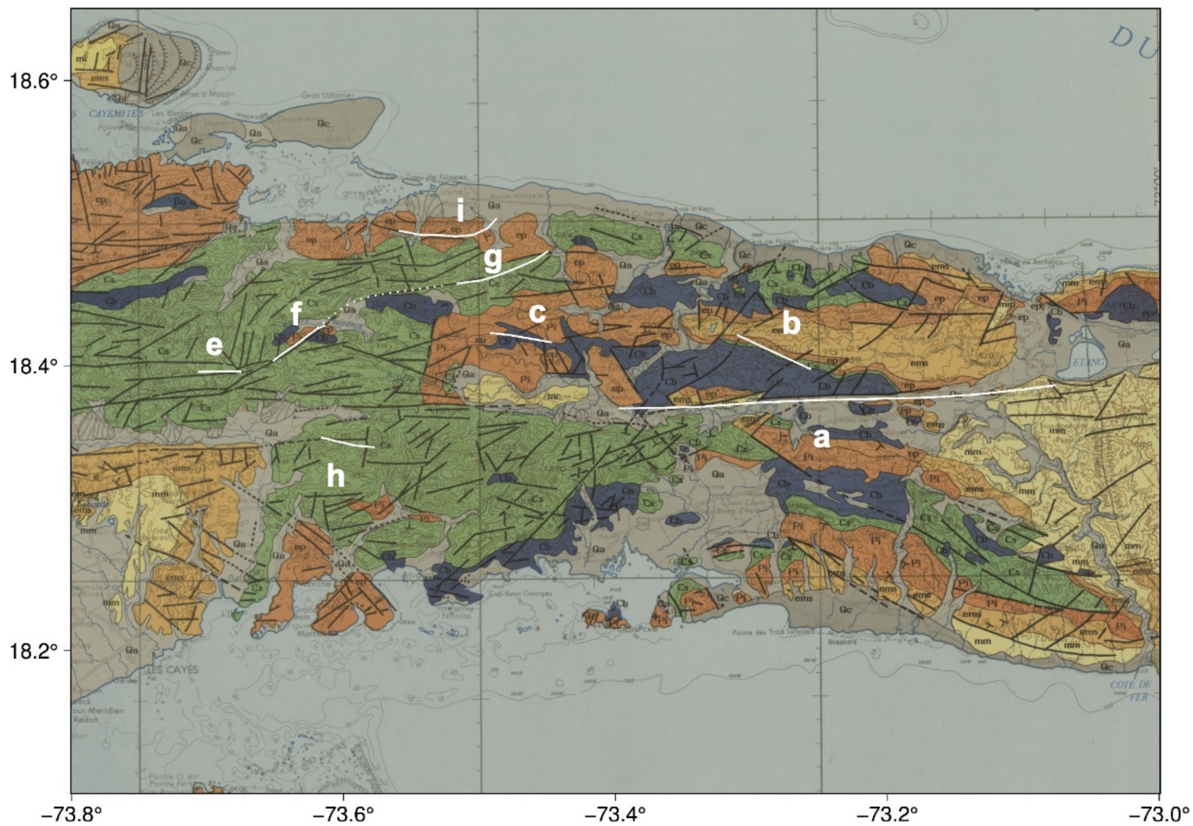

Figure 1.9. Geologic fault map of Haiti originally published by Bien-Aime-Momplaisir et al. (1988a) overlaid with features from the 2021 earthquake identified from InSAR data (white). Massive Cretaceous oceanic basalts of the Caribbean Large Igneous Province (CLIP), Cenomanian to Santonian in age (95 to 83 Ma), shown in purple/blue. Upper Cretaceous pelagic limestones of the *Macaya Fm* (Campanian-Maastrichtian in age, 80-66 Ma) shown in green. Younger Paleocene and Lower Eocene sedimentary units of the *Rivière Glace Fm* (65-60 Ma), shown in orange (Bien-Aime-Momplaisir et al., 1988a)

fault features which were active during the coseismic period and the two week period following the earthquake. Slip direction on these secondary faults is not well constrained and is likely limited to the shallow crust. The offsets on these secondary fault features are much smaller than the coseismic offsets so these features are likely more useful as indicators of surface response than as significant contributors to strain rate for moment release.

To better understand the origin of the secondary fault features, we compare features $a-i$ to a published geologic map Bien-Aime-Momplaisir et al. (1988a) identifying faults in the southern peninsula of Haiti (Fig 1.9). In the southern peninsula, massive Cretaceous oceanic basalts of the Caribbean Large Igneous Province (CLIP) *Dumisseau Fm* (Cenomanian to Santonian in age, 95 - 83 Ma, shown in purple/blue) have been uplifted and exposed at the core of folds which formed in response to compressional tectonic motion (Calais et al., 2016; Mann et al., 2002). These exposed basalts are surrounded by younger overlying sedimentary units, namely the Cretaceous pelagic limestones of the *Macaya Fm* (Campanian-Maastrichtian in age, 80-66 Ma, shown in green), and the still younger sedimentary units of the *Rivière Glace Fm.* (Paleocene and Lower Eocene in age, 65-60 Ma, shown in orange) (Mann et al., 1995).

In Fig 1.9, feature *a* corresponds to the well-documented expression of the main fault strand of the EPGF. Features *c* and *h* do not coincide clearly with mapped faults. Feature *b* occurs at approximately the boundary between outcrops of the oceanic basalts (purple/blue) and younger sedimentary units (orange). Feature *e* is coincident with a mapped fault in the pelagic limestones (green). Finally, features *f* and *g* both coincide well with mapped faults. The phase gradient images give some indication that the fault illuminated at *f* and *g* is continuous beneath the Quaternary alluvium that separates the fault traces on the geologic map, at the northern limit of where the Cretaceous basalts are exposed at the surface.

The younger sedimentary units (in orange, light green) are generally less competent than the more solid, uplifted oceanic basalts. We suggest that faults may be more difficult to identify in the field within or at the contact between the sedimentary units and the basalts. Additionally the boundary between stronger basalts and weaker sedimentary units might be a localized zone of weakness where faults could preferentially occur (for example, feature *b*). There are other more subtle features on the phase gradient map that may be interpreted as faults. However, we limit this discussion to features $a - i$, in which we have the most confidence based on their clarity and persistence in multiple images. The agreement between some features identified in InSAR data with previously mapped faults suggests that these faults were reactivated in the 2021 earthquake. One possible interpretation of the reactivation of these faults is that the uplift observed as dip-slip motion on the eastern portion of the fault rupture is accompanied by compressional motion on a blind thrust fault at depth. GPS observations on the southern peninsula indicate a combination of lateral strike slip at a rate of ~ 5 mm/yr and reverse slip of ~ 2 mm/yr (Calais et al., 2010b) which could be producing something akin to the flower structures interpreted in other areas of the EPGFZ (Mercier de Lepinay et al., 2011; Saint Fleur, Feuillet, Grandin, Jacques, Weil-Accardo, & Klinger, 2015).

In order to better understand the significance of the surface deformations observed surrounding the 2021 Haiti earthquake, it is useful to compare and contrast the observed slip behavior occurring (1) on the main EPGF and (2) on secondary faults associated with the Haiti earthquake to observations of similar slip behavior associated with other earthquakes:

Postseismic slip on the main fault

We observe postseismic slip on the main EPGF adjacent to the fault rupture unfolding for two weeks following the Haiti earthquake. This type of feature was investigated in a similar environment for the 1999 Izmit and Ducze earthquakes on the North Anatolian Fault, where InSAR analysis showed postseismic slip on the main fault from three to ten years after the earthquake, within the limits of the mainshock rupture zones (Hussain et al., 2016). However, the InSAR observations were not able to capture the early spatial distribution of slip. Instead, they were used to solve for along-fault variations of steady state creep. The early evolution was investigated using GPS observations from two near-fault sites to describe the period of early postseismic slip. The observations from Haiti highlight the usefulness of InSAR to identify the individual periods of slip with the higher temporal resolution of the weekly Sentinel-1 imagery, and show that there is variation of early slip along the fault in space as well as in time.

InSAR, GPS, and creepmeter observations of the 2004 Parkfield earthquake on the San Andreas Fault found postseismic slip occurring for $\sim$7 days following the mainshock. The cross-fault offset was $\sim$10 cm, larger than that observed following the 2021 Haiti event (Jiang et al., 2021). Parkfield results indicated that shallow slip migrated from above the main slip patch and spread to the north and the south of the main rupture in the 24 hrs after the earthquake and persisted for at least 7 days. The postseismic slip on the main fault contributed nearly the equivalent moment as was released in the main shock. InSAR imagery and GPS data were combined to determine the total postseismic slip over the 3 months following the earthquake. However InSAR data alone did not provide sufficient time resolution to break down the spatial distribution of slip further (Johanson, 2006; Langbein, 2006). In Haiti, shallow slip extended beyond the rupture in the first 24 hours, as occurred in Parkfield, but with much smaller amplitude. A denser sampling in time for Haiti compared to Parkfield provided subsequent images to show that the spatial distribution of slip accruing on adjacent sections of the main fault migrated over the 7-14 day time period, whereas this information was not accessible for Parkfield.

Following the 2014 Kangding, China, earthquake, Sentinel-1 InSAR observations were used to construct an average LOS displacement rate over 1800 days (Y. Li & Bürgmann, 2021). They solved for shallow creep from short wavelength filtered InSAR time series near the fault after removing a deep slip component. The shallow steady-state creep rate varied along strike from zero to $\sim$10 mm/yr along the fault. They were also successful in distinguishing different decay rates of postseismic creep for different segments along the fault with InSAR.

These examples illustrate that postseismic creep is often observed with InSAR on strike-slip faults following a major earthquake. These observations have often been used to estimate variations in creep rate that indicate varying frictional behavior along the length of the faults. InSAR data from Haiti shows that phase gradient maps can be used to observe the spatial distribution of early slip. This suggests that past earthquakes could be revisited to further investigate the details of the spatio-temporal variation in slip, and, in particular, extend the investigation further away from the main rupture segment to include the possibility of secondary fault structure activity. Characterizing the spatial distribution of creeping segments of strike slip faults and the degree of fault coupling contributes to understanding the ground motion and hazards associated with potential ruptures on faults with different properties (Aagaard et al., 2013; Y. Li & Bürgmann, 2021).

The lack of recent rupture on the Miragoâne segment of the EPGF raises questions about its seismogenic potential, a question complicated by InSAR observations of shallow postseismic slip. While an analysis of seismic hazard on this segment is beyond the scope of this study, we can make a rough estimate of the accumulated seismic moment deficit by making some simplifying assumptions. We assume that the last major earthquake that could have occurred on this segment was in 1770 (McCann, 2006) and that the length of the unruptured Miragoâne segment is 36 km as shown in Figure 1a. This geometry assumes that the 2010 earthquake released moment on the EPGFZ east of Lake Miragoâne, even though that earthquake occurred on the dipping Léogane fault and not the main EPGF. If we assume an interseismic slip rate of ~ 9 mm/yr at depth (S. J. Symithe et al., 2015) on a vertical strike-slip EPGF over the last 252 years (1770 - 2022) with the fault locked to a depth of 15 km (Frankel et al., 2011; S. J. Symithe et al., 2015) and a shear modulus of 45 GPa (Hayes et al., 2010), then the accumulated seismic moment is $5.51 \times 10^{19} N$. If this moment were to be released in a single seismic event, we estimate an available moment magnitude of $M_w 7.1$. We can also consider the impact that shallow slip could have in reducing this estimate. The postseismic deformation signals observed following both the 2010 and 2021 Haiti earthquakes decay rapidly with distance perpendicular to the fault (i.e. within about 1—2 km of the EPGF), consistent with subsurface slip that is confined to the shallow crust but locked beneath. Relatively short duration transient postseismic slip likely does not make a significant contribution to reducing the accumulated moment on this unruptured segment of the fault. If, however, the Miragoâne segment were consistently slipping from the surface to 5 km depth, the moment deficit would be reduced to $3.67 \times 10^{19} N$ which could still produce an event of $M_w = 7.0$. This estimate would need to be revised after a longer time period to provide a better constraint on the amount of steady creep that was releasing moment aseismically and providing a potential reduction in seismic hazard. It can be considered an estimate of upper bound on the moment deficit.

Slip on secondary faults

A second major conclusion from this work is that secondary fault structures were active in the near field of the Haiti earthquake, that some of these structures were previously mapped faults, and motion on these faults persisted for more than 2 weeks following the event. Earthquakes in the well-studied Southern California region provide several analogous examples of slip on secondary faults in response to earthquake ruptures. InSAR observations of the 1992 Landers earthquake (Price & Sandwell, 1998b) illuminated preexisting mapped faults within 50 km of the main rupture using phase gradient techniques. Because of the sparse InSAR repeat acquisitions at this time, the temporal evolution of this signal is uncertain. Similarly, Sandwell et al. (2000b) used InSAR data to study the Hector Mine Earthquake ($M_w 7.1$, 1999). Here, the phase gradient technique revealed triggered slip on adjacent faults within 4 days of the earthquake. Most recently, InSAR phase gradient techniques were used following the 2019 Ridgecrest earthquake (Xu, Sandwell, & Smith-Konter, 2020a; Xu, Sandwell, Ward, et al., 2020b), to reveal slip on hundreds of secondary faults. However, none of these examples provide documented observations of slip on secondary faults which persists for weeks, as we observe following the 2021 Haiti earthquake for feature $f-g$ north of the main EPGF.

We consider separately examples of shallow creep observed with InSAR that were triggered by regional or distant earthquakes, as opposed to earthquakes on the same fault system. (Bodin et al., 1994) showed creep on the Southern San Andreas Fault triggered by the 1992 Landers, Big Bear, and Joshua Tree earthquakes using creepmeter observations. The spatial extent of triggered slip on the southern San Andreas was captured by InSAR following the 2017 Chiapas earthquake (Tymofyeyeva et al., 2019), where creepmeters indicated that the timing corresponded to the passage of seismic waves. Surface slip was also triggered on the San Andreas Fault by the 2010 El Mayor-Cucapah earthquake (Wei et al., 2011).

These studies taken together illustrate the challenge of distinguishing slip triggered by dynamic stresses due to the passage of seismic waves from slip triggered by changes in the static stress field. Additional observations such as creepmeters or continuous GPS are required to pin down the timing of the slip. In Haiti, the continuation of slip on secondary faults for at least two weeks after the earthquake makes it likely that the cause could not have been solely dynamic triggering. Further study of the mechanism for secondary fault reactivation could include exploration of major aftershocks or distant events during the later time period. A teleseismic event in Chile was shown to trigger an increase in seismic tremor on faults in Haiti, and presented some evidence of triggering an increase in aftershocks (Aiken et al., 2016), so an extended study following the release of a final earthquake catalog could be useful.

Douilly et al. (2022) provides detailed cross-sections of relocated aftershocks that define the north dipping rupture plane beneath our mapped secondary features f and g. The scarcity of seismicity above 8 km suggests that our secondary features may represent surface response to motion or deformation in the block above the north dipping fault. The sparse shallow seismicity may indicate antithetic faults above 8 km that are favorably oriented with respect to the stress change of the main shock. The relationship of the seismicity to our secondary faults should be further investigated.

1.7 Conclusions

The 2021 Haiti earthquake did not rupture the EPGFZ adjacent to the 2010 earthquake but skipped over the intervening Miragoâne segment. InSAR observations provide evidence of postseismic slip on this unruptured segment following both earthquakes. Deformation following the 2021 earthquake accrued over approximately 40 km to the east of the rupture on the main strand of the EPGF. In some places, there was as much as 2 cm of cross-fault displacement. The slip signal persisted for approximately two weeks following the earthquake before decaying below the InSAR detection threshold. Deformation following the 2010 earthquake occurred on the same unruptured EPGF segment and extended from Lake Miragoâne to about 15 km to the west and occurred at least 4 days after the event. The amount of slip observed on this unruptured segment is not sufficient to compensate for the expected accumulated seismic moment in the gap, and therefore the fault remains a significant hazard. In other strike slip environments, especially in desert settings, using InSAR to determine the fault properties of creeping segments and the degree of coupling contributes to a better understanding of the hazard associated with potential future ruptures. This study illustrates the potential for this type of investigation in a tropical environment.

Secondary fault features revealed by phase gradient techniques indicate complex faulting to the north of the mapped EPGF. When cross-referenced with existing geologic maps, these features take on new import as reactivated older fault features. This reactivation of secondary fault features agrees with the broad distribution of aftershock relocations north of the mapped EPGF (Calais, Symithe, Monfret, Delouis, Lomax, Courboulex, Ampuero, Lara, Bletery, Chèze, Peix, Deschamps, de Lépinay, et al., 2022a), and could indicate fault complexity or the presence of a blind thrust at depth. The main fault rupture consisted of dip-slip motion in the east and left-lateral strike slip motion in the west (Calais, Symithe, Monfret, Delouis, Lomax, Courboulex, Ampuero, Lara, Bletery, Chèze, Peix, Deschamps, de Lépinay, et al., 2022a; Okuwaki & Fan, 2022b), similar to the 2010 pattern of rupture on the Léogane fault (Calais et al., 2010b). This produced a pattern of uplift between the EPGF and the secondary fault structures that is consistent with the implied direction of motion from the phase gradient and corresponding LOS deformation maps. The involvement of secondary faults in this rupture requires adjustments to the model of a simple segmented strike-slip EPGF (Saint Fleur et al., 2020b), and indicates that an accurate description of hazard should include transpression in a zone surrounding the main EPGF.

Locations with tropical climates and dense vegetation such as Haiti present a challenge for measuring surface deformation with InSAR. The longer wavelength of ALOS-2 data complemented by the frequent acquisitions of Sentinel-1 was a key pairing for the success of this study. The ability to resolve small-scale deformation features with phase gradient processing using L-band data in such a vegetated area is an important advance for the broader application of this technique. Sentinel-1 wrapped phase gradients have been successfully used to detect slip on secondary fault features in arid climates, i.e. Ridgecrest in the Owens Valley (Xu, Sandwell, & Smith-Konter, 2020a; Xu, Sandwell, Ward, et al., 2020b), Landers (Price & Sandwell, 1998b), and Hector Mine (Sandwell et al., 2000b) in the eastern California shear zone in the Mojave desert. However, this work presents the first successful application in a vegetated region which opens the door to future studies of a larger number of events in a wider variety of climates. In contrast to previous studies, the Sentinel-1 phase gradients over Haiti were largely unable to resolve deformation features, even when stacking multiple pairs. The upcoming NISAR mission should provide an ideal balance between frequent acquisitions and long wavelength (L-band) radar observations (Rosen & Kumar, 2021).

1.8 Data and Resources

Aftershock locations were calculated by the local Haitian seismic network, Ayiti-Séismes (https://ayiti.unice.fr/ayiti-seismes/) and (Calais, Symithe, Monfret, Delouis, Lomax, Courboulex, Ampuero, Lara, Bletery, Chèze, Peix, Deschamps, de Lépinay, et al., 2022a). Sentinel-1 InSAR data used in this study were collected and distributed by the European Space Agency (ESA) and are freely available via the Sentinel data hub (http://scihub.copernicus.eu/dhus). ALOS-2 InSAR data used in this study were collected by the Japanese Aerospace Exploration Agency (JAXA) and made available to the authors under an individual proposal. All interferograms and derived data products used in this study are made freely and publicly available at https://doi.org/10.5281/zenodo.6834534 (Yin, Xu, Haase, Douilly, Sandwell, & Mercier de Lépinay, 2022) and also at https://topex.ucsd.edu/haiti_7.2/index.html.

Supplemental Material for this article includes three supplemental figures and a more complete description of the moment deficit calculation referenced in the discussion section. Figure S1 shows all Sentinel-1 wrapped phase interferograms during the Aug 14 - Sep 4, 2021 time period in sequential pairs. Figure S2 shows the stacked phase gradient plot for ALOS-2 tracks A043 and A042 in the range (look) direction. Figure S3 shows an example of a phase gradient data from Sentinel-1 interferograms which do not show discernible deformation features.

1.9 Acknowledgments

We are grateful to two reviewers, Qi Ou and Jeremy Maurer, for their thoughtful and constructive feedback which improved the manuscript and figures. We thank the operators and hosts of the Ayiti-Séismes earthquake monitoring network at Bureau des Mines, Faculté des Sciences, Laboratoire URGéo, Université d'état d'Haïti, Ecole Normale Supérieur, and Laboratoire Géoazur for providing aftershock locations and making them free and openly available. We thank ESA for the rapid acquisition and distribution of Sentinel-1 data. We thank JAXA for access to ALOS-1 and ALOS-2 data. Rapid InSAR data processing was supported by a National Science Foundation RAPID grant (Grant 2150704). We thank Sylvert Paul and Francoise Courboulex at GéoAzur, and Eric Calais at ENS for helpful discussions related to the earthquake. We thank Katherine Guns for InSAR processing support. The development of the GMTSAR software was supported by the National Aeronautics and Space Administration (NASA) and the National Science Foundation through the NASA Earth Surface and Interior program (NNX16AK93G and 80NSSC19K1043), the NSF Office of Advanced Cyberinfrastructure program (OAC-1834807), and the NSF EarthScope program (EAR-1147435, EAR-1424374, EAR-1614875).

Chapter 1, in full, is a reprint of the material as it appears in The Bulletin of the Seismological Society of America. Yin, H. Z., Xu, X., Haase, J. S., Douilly, R., Sandwell, D. T., and Mercier de Lepinay, B., Seismological Society of America, 2023. The dissertation author was the primary investigator and author of this paper.

Chapter 2

3D dynamic rupture modeling of the 2021 Haiti earthquake used to constrain stress conditions and fault system complexity

2.1 Abstract

The 2021 $M_w 7.2$ Haiti earthquake was a devastating event which occurred within the Enriquillo Plantain Garden Fault Zone (EPGFZ). It is not well-understood why neither the 2010 nor 2021 earthquakes were simple strike slip events and, instead ruptured with two distinct patches of dip slip and strike slip motion on largely separate fault planes. We use 3D dynamic rupture modeling of this earthquake to test which conditions may have controlled the complex rupture. A suite of dynamic rupture simulations are developed to identify key factors required to reproduce the major characteristics and observations of the event including: the characteristic spatial and temporal separation of strike-slip and dip-slip motion, rupture transfer to the Ravine du Sud Fault (RSF), the InSAR surface deformation field, GNSS offsets, total seismic moment, and source time function. We construct a detailed fault system geometry which includes a north-dipping Thrust Fault (TF) and near-vertical RSF, along with surrounding regional and secondary faults. We find that along-strike changes to the frictional strength of the TF are needed to focus the slip to reproduce the scale and pattern of the deformation observed with InSAR. We find that lateral changes in the regional stress shape and orientation are key to reproducing

the observed rupture transfer from the TF to the RSF while maintaining the rake required to reproduce the broad InSAR surface deformation pattern and multi-peak source time function. The dynamic rupture modeling results suggest that significant variability in fault stress and strength as well as complexities of the subsurface geometry may have been key controls on the dynamics of the 2021 rupture.

2.2 Introduction

The 2021 M_w7.2 Haiti earthquake led to more than 2200 deaths and struck just over a decade after the devastating 2010 M_w7.0 earthquake which was one of the deadliest earthquakes recorded globally. Both events occurred within a complex network of faults comprising the Enriquillo Plantain Garden Fault Zone (EPGFZ), which spans the Tiburon Peninsula in southern Haiti (Figure 3.1). Although the main Enriquillo Plantain Garden Fault (EPGF) has historically been mapped as a near-vertical fault which accommodates purely strike slip motion, neither the 2010 nor the 2021 event had a simple strike-slip focal mechanism, nor did either clearly rupture this well-known fault as it is mapped. Instead, both recent ruptures initiated on a north-dipping fault segment which hosted significant dip slip motion and then transferred westward to an adjacent steeply-dipping fault segment with primarily strike slip motion (Calais, Symithe, Monfret, Delouis, Lomax, Courboulex, Ampuero, Lara, Bletery, Chèze, Peix, Deschamps, de Lépinay, et al., 2022b; Z. Li & Wang, 2023; Okuwaki & Fan, 2022a; Wen et al., 2023; Yin, Xu, Haase, Douilly, Sandwell, & Mercier de Lepinay, 2022). Both events also had major slip occurring off of the mapped EPGF fault: the 2010 event ruptured the blind Léogane thrust fault with seemingly no major slip accommodated on the EPGF, while the 2021 earthquake has been proposed to have initiated on a north-dipping thrust fault (it is unclear whether this is the EPGF or an unmapped fault) and then transferred westward to the mapped Ravine du Sud fault (Douilly et al., 2023; Raimbault et al., 2023) (Fig. 3.1). Major questions remain about the fault geometry responsible for the 2021 event and how that geometry relates to the known fault system. It is also still not well understood why neither the 2010 nor 2021 event was a simple strike slip event and, instead, each ruptured with two distinct patches of dip slip and strike slip motion on largely separate fault planes.

The recent 2010 earthquake rupture occurred to the east of the 2021 rupture (Fig. 3.1) and both events increased Coulomb Failure Stress (CFS) on the section of the EPGF between the two ruptures (Calais, Symithe, Monfret, Delouis, Lomax, Courboulex, Ampuero, Lara, Bletery, Chèze, Peix, Deschamps, de Lépinay, et al., 2022b; S. J. Symithe et al., 2013a). This segment of the EPGF, however, has remained unruptured by either earthquake, raising the question of whether it is locked and seismically loaded or if it is accumulating or accommodating strain in some other way. Interestingly, centimeter-scale shallow creep was observed on sections of this unruptured segment following both the 2010 and 2021 events (Maurer et al., 2022a; Yin, Xu, Haase, Douilly, Sandwell, & Mercier de Lepinay, 2022).

The combination of dip slip and strike slip motion observed in both 2010 and 2021 earthquakes is not unexpected given the tectonic setting of this fault zone. The EPGFZ occurs within the boundary between the North American (NA) and Caribbean (CAR) plates, which collide obliquely at an estimated rate of 18–20mm/yr (DeMets et al., 2000a). The Septentrional Fault, North Hispaniola fault, and the EPGFZ together accommodate both left-lateral and shortening motion, with the EPGFZ accommodating roughly half of the NA-CAR relative motion. A network of GNSS (Global Navigation Satellite System) stations throughout the region has allowed for the mapping of strain accumulation across the plate boundary (Calais et al., 2023; S. Symithe et al., 2015). Block modeling using GNSS data suggests two competing models for strain accumulation: The first model proposes that the EPGFZ accommodates about 6–7 mm/yr of left-lateral strike-slip motion, while the Jeremie-Malpasse (JM) reverse fault system off of the north shore of the Southern Peninsula (Fig. 3.1) is responsible for accommodating 6–7 mm/yr of north-south shortening (plate boundary-perpendicular motion). The second model proposes that the transpressive motion is accommodated primarily by the EPGFZ, with offshore thrust faults playing a less important role in shortening (Calais et al., 2023). A better understanding of where transpression is localizing and driving seismicity is needed to improve understanding of seismic hazard.

Seismic and geodetic observations surrounding the 2021 earthquake provide critical insights into the rupture process. The event was recorded by the Ayïti-Seismes network, which, at the time of the earthquake, included four accelerometers (three of which were Raspberry Shake stations hosted by residents), and three broadband seismometers (Calais, Symithe, Monfret, Delouis, Lomax, Courboulex, Ampuero, Lara, Bletery, Chèze, Peix, Deschamps, de Lépinay, et al., 2022b). Data from these stations were used to precisely locate a large cluster of aftershocks in the eastern portion of the rupture broadly delineating a north-dipping structure, with a more sparse cluster of aftershocks to the west indicating a near-vertical structure approximately coincident with the mapped RSF (Douilly et al., 2023). Interferometric Synthetic Aperture Radar (InSAR) geodetic imagery was captured from ALOS-2 and Sentinel-1 satellite missions, which resolved a detailed spatial pattern of co- and post-seismic ground deformation. Unwrapped InSAR interferograms showed deformation in the direction of the Line-of-Sight (LOS) of the observing satellite. Ascending and descending InSAR observations of the 2021 event constrained a region of uplift in the eastern part of the rupture consistent with thrust motion on a north-dipping structure, while fault-parallel motion dominated to the west, concentrating on the Ravine du Sud fault where the InSAR captured rupture reaching the surface (Z. Li & Wang, 2023; Raimbault et al., 2023; Yin, Xu, Haase, Douilly, Sandwell, & Mercier de Lepinay, 2022). GNSS offsets, which provide absolute static deformation measurements across the peninsula, confirmed the broad pattern of deformation observed in the InSAR data (Raimbault et al., 2023). Saint Fleur et al. (2024) conducted fieldwork following the 2021 event focused on documenting extensive surface cracking in response to the coseismic rupture. In the west, strike-slip cracks dominated, while the eastern section exhibited primarily thrust faulting. This variation aligns with the earthquake's mixed-mode rupture mechanism.

Several studies have investigated the slip distribution and fault geometry of the 2021 M_w 7.2 Haiti earthquake (i.e., Calais, Symithe, Monfret, Delouis, Lomax, Courboulex, Ampuero, Lara, Bletery, Chèze, Peix, Deschamps, de Lépinay, et al., 2022b; Goldberg et al., 2022; Z. Li & Wang, 2023; Maurer et al., 2022a; Okuwaki & Fan, 2022a; Raimbault et al., 2023; Wen et al., 2023). Despite differences in the inversion methods, considered observation datasets, and fault geometry, most inversion studies agree on the earthquake breaking at least two main fault segments. The rupture nucleated on an eastward north-dipping thrust segment where the slip reached ∼2.5-3 m without rupturing the surface. Then the rupture transferred westward to a sub-vertical strike-slip segment (broadly agreed to be the RSF) with ∼1-2 m of slip reaching the surface. Interestingly, the rupture does not clearly align with the previously mapped vertical EPGF. Kinematic models consistently inferred source time functions (STFs) that contain at least two main peaks at 5-8 sec and 15-20 sec after the origin time, likely each coincident with a corresponding segment. STFs are in agreement with back-projection results that show two strong seismic radiation episodes with roughly the same timing

Despite the extensive work that's been done to understand the tectonics in Haiti through data collection networks (e.g. Calais, Symithe, Monfret, Delouis, Lomax, Courboulex, Ampuero, Lara, Bletery, Chèze, Peix, Deschamps, de Lépinay, et al., 2022b; Raimbault et al., 2023; S. Symithe et al., 2015), geophysical surveys (e.g. Calais et al., 2023), and geologic mapping (e.g. Mercier de Lépinay et al., 2011; Prentice et al., 2010a; Prentice et al., 2003; Saint Fleur, Feuillet, Grandin, Jacques, Weil-Accardo, & Klinger, 2015; Saint Fleur et al., 2020a, 2024), gaps remain in our understanding of the complex faulting that drives seismic hazard, including the 2021 event.

Significant advances in the capabilities of dynamic rupture modeling techniques, enabled in part by the proliferation of high performance computing, provide an opportunity to understand the complex dynamics of the 2021 earthquake through 3D dynamic rupture simulation. Unlike kinematic or static slip inversions, which solve for slip distributions that sufficiently satisfy detailed observations, dynamic rupture models are forward simulations with a prescribed set of initial conditions and model parameters and allow the rupture to unfold spontaneously. Initial conditions consider fault geometry, material properties, fault strength (e.g., frictional properties, critical distance), and a description of pre-event stress on the fault. With these initial conditions it is possible to solve for the dynamic evolution of the rupture including fully dynamic wave propagation and permanent deformation (Harris et al., 2011; Harris et al., 2018; Ramos et al., 2022). While kinematic models can illuminate when and where slip occurred, dynamic rupture models can probe why the fault ruptured in a particular way, providing unique insights into the conditions that drove rupture.

Dynamic rupture simulations have been used to study fundamental aspects of earthquake physics (e.g. Douilly et al., 2015a; Gabriel et al., 2023), to assess earthquake hazards (e.g. Aochi & Ulrich, 2015; Douilly et al., 2017), to recreate notable rupture patterns in past earthquakes (Ma et al., 2008; Wollherr et al., 2019) and to discriminate between competing models of fault system geometries and faulting mechanisms (e.g. Palgunadi et al., 2020; Ulrich et al., 2019). In this study, we focus on identifying the conditions that control key observations of the 2021 M_w7.2 Haiti earthquake. Using the dynamic rupture models, we simulate InSAR surface deformations, GNSS offsets, and source time functions to compare with observations. We also aim to capture key rupture characteristics that are inferred from the observations, primarily the spatial and temporal separation of left-lateral and reverse fault slip, and rupture transfer from the initial fault to the RSF to better understand the conditions that lead the observed rupture.

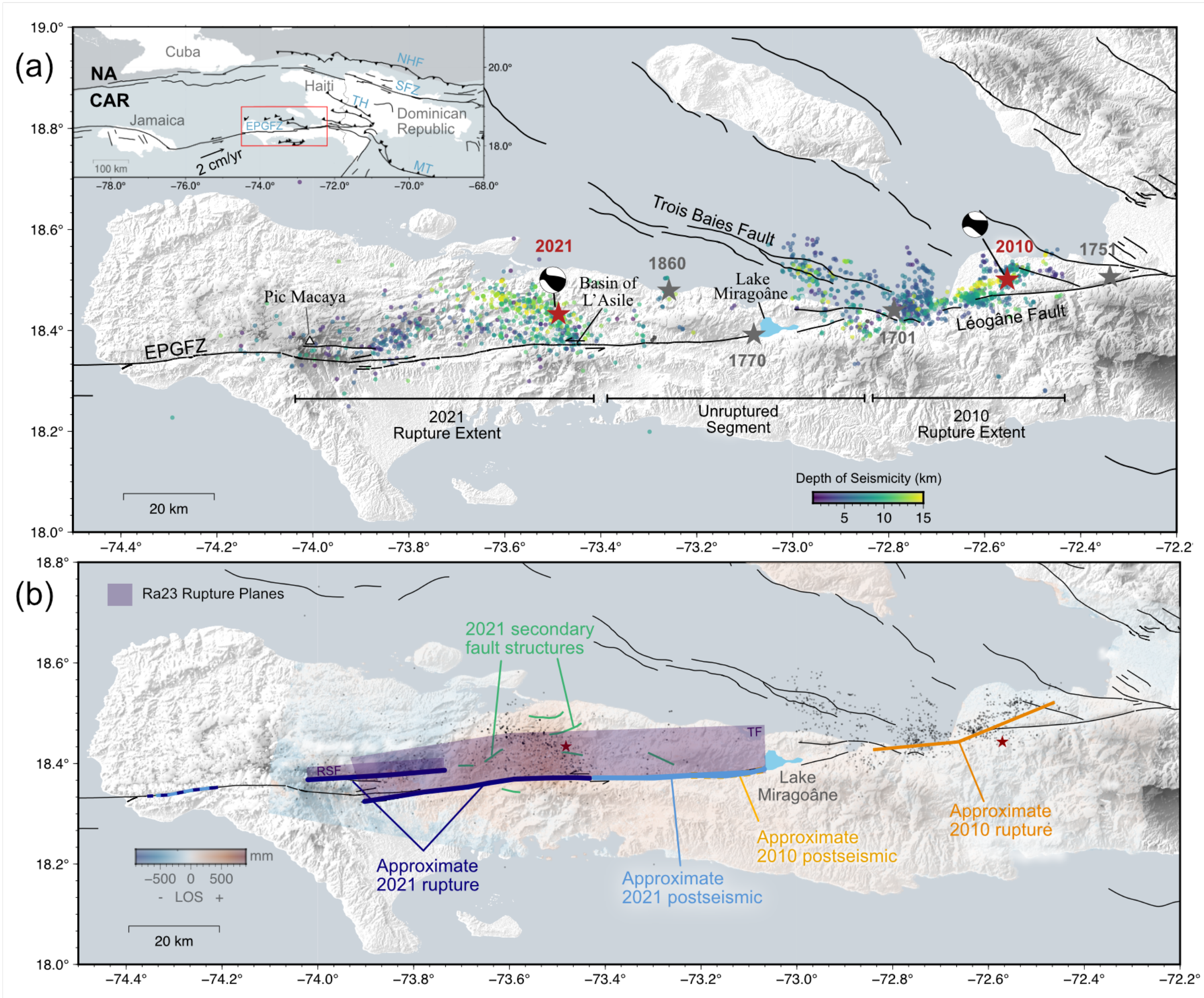

Figure 2.1. Overview of the tectonic setting of the 2021 earthquake. Top left inset shows the North American (NA) and Caribbean (CAR) tectonic plates. (a) Overview of the southern peninsula of Haiti, highlighting major geographic markers, fault zone locations, and historic earthquakes. Major historic earthquakes are marked by stars, with red stars highlighting the locations of the 2021 M_w7.2 and 2010 M_w7.0 epicenters with CMT moment tensor solutions.; Aftershock locations are shown with circles, colored by event depths. Aftershock locations following the 2010 event on the Léogane blind thrust fault and Trois Baies fault are from Douilly et al. (2023) (b) Descending InSAR unwrapped interferogram is overlaid on topography, where red indicates the region of surface uplift over the eastern part of the rupture north of the fault. The two main fault planes used in this study, the Thrust Fault (TF), and the Ravine du Sud Fault (RSF) are shown with purple transparent rectangles. The approximate extent of rupture is taken from InSAR data. Modified from Yin, Xu, Haase, Douilly, Sandwell, and Mercier de Lepinay (2022)

2.3 Methods and Model Setup

We solve the coupled dynamic rupture and seismic wave propagation problem using the open-source software SeisSol (https://github.com/SeisSol/). SeisSol utilizes a Discontinuous Galerkin discretization with arbitrary high-order derivative (ADER) time integration and local time stepping on unstructured adaptive tetrahedral meshes (Dumbser & Käser, 2006). SeisSol is verified through numerous dynamic rupture benchmark problems (Harris et al., 2018; Pelties et al., 2014) and is optimized for high performance computing achieving a significant fraction of the theoretical peak performance on several petascale supercomputers (Heinecke et al., 2014; Krenz et al., 2021; Uphoff et al., 2017). SeisSol allows for the combination of geometrically complex fault structures with region-specific fault and material properties. This is critical in Haiti where the geometric complexity of the fault zone has been interpreted to be central to the mechanics and strain partitioning of the EPGF fault system (Douilly, Haase, Ellsworth, Bouin, Calais, Symithe, Armbruster, de Lepinay, et al., 2013a; S. J. Symithe et al., 2013a; Wang et al., 2018b).

To construct a 3D dynamic rupture model, we must prescribe a set of parameters and initial conditions which govern the rupture including fault geometry, material properties, relative fault strength, and initial stress orientation and moment magnitude (Ramos et al., 2022). We choose parameters that reflect the best-available data and regional knowledge. In cases where relevant properties are unknown, we conduct sensitivity tests to determine the range of parameter values that allow for the reproduction of the earthquake observable. These parameters and initial conditions are described below.

2.3.1 Fault System Geometry

Fault geometry is a primary control on rupture evolution (Nielsen et al., 2000). The fault mesh developed to reproduce these observations is highly complex, with 17 non-planar, 3D fault segments that curve and intersect over a 200+ km domain to accurately capture the fault complexity documented in the region. This geometry combines results from several sources including mapped faults and slip inversion studies (Fig. 2.2). The geometry of the main two faults involved in the 2021 rupture is adapted from the Raimbault et al. (2023) study which distributes cosesismic slip from the 2021 event on two faults: (1) a thrust fault running subparallel to the EPGF (possibly the EPGF itself or a separate structure), herein called the Thrust Fault (TF) which dips north 66 ± 4°; and (2) the Ravine du Sud Fault (RSF) which is a mapped near-vertical fault, dipping north 86 ± 2°, Fig. 2.2). We extend the TF eastward from 73.2°W (where the Raimbault et al. geometry ends) to Lake Miragoane, following the mapped EPGF trace to allow for the possibility that this is a continuous structure. Raimbault et al. (2023) develop this fault geometry based on the nonlinear kinematic finite fault slip inversion constrained by teleseismic data in Calais, Symithe, Monfret, Delouis, Lomax, Courboulex, Ampuero, Lara, Bletery, Chèze, Peix, Deschamps, de Lépinay, et al. (2022b). Raimbault et al. (2023) combine fault traces of the RSF, EPGF, and geologically mapped fault traces from Saint Fleur et al. (2020a). They then explore a range of fault dips from 0 to 90° for these two segments to determine the fault dip (and slip distribution) that minimizes misfit between model prediction and GNSS and InSAR data.

Centimeter-scale offsets across linear features located 10-20 km away from the main fault were observed to slip in the 2 weeks following the earthquake with InSAR imagery (Yin, Xu, Haase, Douilly, Sandwell, & Mercier de Lepinay, 2022). These features are included to investigate how they behave during the dynamic rupture process and, in the absence of information about fault dip, are assumed to be vertical. We also include the 2010 earthquake rupture geometry which is taken from Douilly et al. (2015a). Offshore thrust faults which produced significant aftershock activity following the 2010 earthquake are taken from analysis of seismic reflection surveys in Calais et al. (2023). Finally, surrounding mapped faults are taken from the comprehensive database in Saint Fleur et al. (2020a) and are assumed to be vertical.

Our computational mesh is a box of $700 \times 500 \times 150\text{km}^3$ in the east, north, and vertical direction, respectively. The size is chosen to be large enough to avoid any spurious reflected waves from the non-perfect absorbing boundaries. The top surface of the domain includes the topography from the SRTM global DEM (Farr et al., 2007) downsampled at 1 km. The domain is discretized with tetrahedral elements of variable size using the software *PUMGen* (https://github.com/SeisSol/PUMGen/). *PUMGen* embeds MeshSim from SimMetrix, the underlying mesh generator of SimModeler (www.simmetrix.com), and exports the mesh into the efficient PUML format used by *SeisSol*. The mesh resolution is set to an element edge length of 200 m on the fault surfaces and gradually coarsens away from the faults to a maximum edge length of 15 km in the volume. The mesh includes a $300 \times 100 \times 40$ km^3 high-resolution box within which frequencies of at least up to 1 Hz can be resolved. The constructed unstructured tetrahedral mesh consists of 12 million elements. A simulation with 4th-order accuracy in time and space for 30 s requires $\sim$ 1100 CPU hours on the supercomputer SuperMUC-NG at the Leibniz supercomputing center in Garching, Germany. Elastic properties of the medium (density and Lamé's coefficients) are derived from the 1D velocity model of (Douilly et al., 2023) determined from aftershocks of the 2021 earthquake. Fault geometries and material properties are made available in the supplemental information.

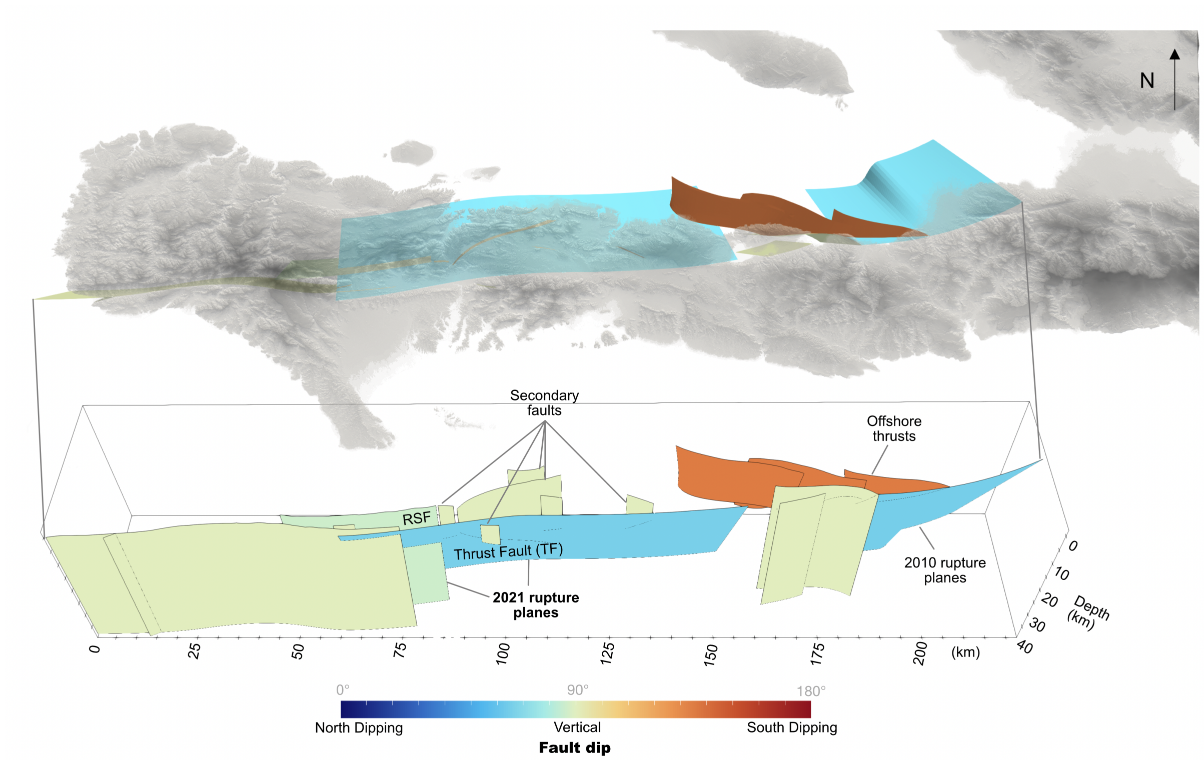

Figure 2.2. An oblique view of the fault geometry. 2021 M_w7.2 coseismic rupture planes are taken from Raimbault et al. (2023), secondary faults observed from InSAR data are taken from Yin, Xu, Haase, Douilly, Sandwell, and Mercier de Lepinay (2022), offshore thrust faults are modified from Calais et al. (2023), the 2010 M_w7.0 planes are adapted from Douilly et al. (2015a), and surrounding mapped faults are taken from Saint Fleur et al. (2020a). The top panel shows a top-down view of the topography of Haiti overlaid on the fault surfaces. The bottom panel shows a slightly adjusted view of the fault surfaces, labeled by source. Faults are colored by fault dip.

2.3.2 Friction and Fault Strength

A linear slip-weakening (LSW) friction law is used to describe the frictional fault strength (Andrews, 1976; Ida, 1972). Coseismically, the slip-dependent fault weakening behavior governed by aging law rate-and-state friction is similar to that governed by linear slip-weakening friction (e.g., Bizzarri & Cocco, 2003; Garagash, 2021; Kaneko et al., 2008). Fault strength, τ, at any location on the fault is calculated using:

$$\tau = -C - min(0, \sigma_n)(\mu_s - \frac{\mu_s - \mu_d}{D_c} min(S, D_c))$$

Where C is the on-fault frictional cohesion , σ_n is the normal stress, μ_s and μ_d are the static and dynamic coefficients of friction, respectively, D_c is the critical slip distance, and S is the accumulated fault slip. SeisSol convention is that compressive stresses are negative. Faults begin to slip when local shear stress exceeds the local fault strength. Fault strength then decreases linearly from static to dynamic levels over the critical slip distance, D_c, where larger critical distance implies larger fracture energy. μ_s, μ_d, and D_c are defined throughout the fault geometry and are assumed to be spatially uniform, except in some notable circumstances where we vary the value of μ_s on some sections of the TF, as described in the results section. We set on-fault frictional cohesion to 0.5 MPa below 6km on each fault and increase it linearly to 3 MPa at the surface to create a barrier to large surface ruptures.

2.3.3 Pre-stress Ratio

In a dynamic rupture simulation, only a small part of the fault needs to reach failure in order to initiate sustained rupture. The change in stress at the rupture front and dynamic stresses from seismic waves can raise the local shear stresses to exceed local fault strength, thereby sustaining the rupture. R, or the relative pre-stress ratio (Aochi, 2003; Ulrich et al., 2019), is the ratio of potential stress drop to full breakdown strength drop. The value of R is calculated from three components : 1) initial (static) fault strength, $\tau_y = \sigma_n \mu_s$; 2) final (dynamic) fault strength, $\tau_f = \sigma_n \mu_d$ and 3) initial shear stress, τ_0, resolved on the fault surfaces (Fig. 2.4).

The potential stress drop can be defined as the difference between initial shear stress and final shear stress ($\tau_0 - \tau_f$), while the potential strength drop is defined as the difference between the initial fault strength and the final shear stress. Under LSW, the final shear stress does not account for rapid co-seismic weakening and restrengthening (Gabriel et al., 2023; Madariaga, 1976) and so is equivalent to the dynamic shear strength. Accordingly, we can define:

$$R = \frac{\tau_0 - \tau_f}{\tau_y - \tau_f}$$

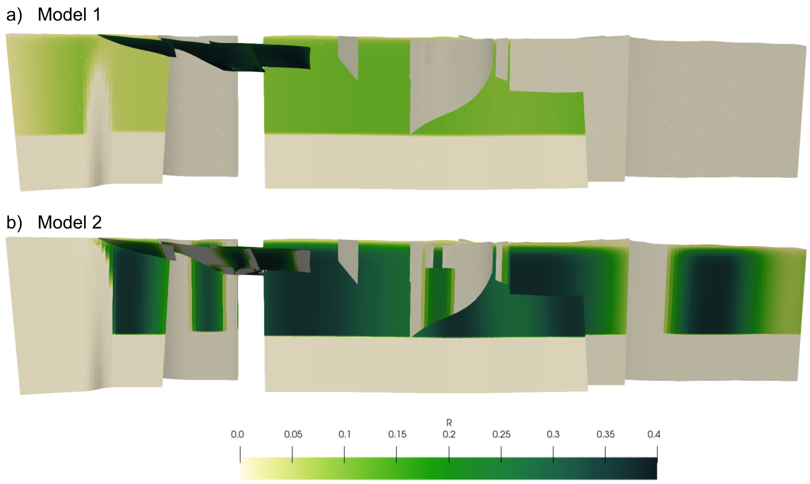

Figure 2.3. Pre-stress ratio values, R, resolved on the fault surfaces: a) R in the thrust faulting regime where the regional stress tensor has orientation SH_{max} = 40° stress shape ratio, ν=0.5; b) R in the strike-slip faulting regime where the regional stress tensor has orientation SH_{max} = 50° stress shape ratio, ν=0.0;

where τ_0 is the initial traction on the fault, τ_f is the final traction on the fault, τ_y is the fault strength which must be exceeded to initiate slip (Fig. 2.4). We can then define R as:

$$R = \frac{\tau_0 - \mu_d \sigma_n}{(\mu_s - \mu_d)\sigma_n}$$

(Tinti et al., 2021). These variables are shown schematically in Figure 2.4.

The value R_0 is a parameter used in the implementation of regional stresses, which defines the maximum value of R for a given regional stress tensor (Aochi, 2003). This effectively acts to scale the overall values of R resolved on the fault surfaces.

Fig. 2.4B shows a schematic profile of the fault stress and strength as a function of depth taken at one location on the fault. In the case of a fault near failure, the initial fault stress (black) will lie between the fault strength (green) and final stress levels (red). If rupture reaches this location on the fault, shear stresses may be brought above the shear strength and then drop to the final shear stress. If at any point the stresses are insufficient to reach the static strength then rupture will not propagate.

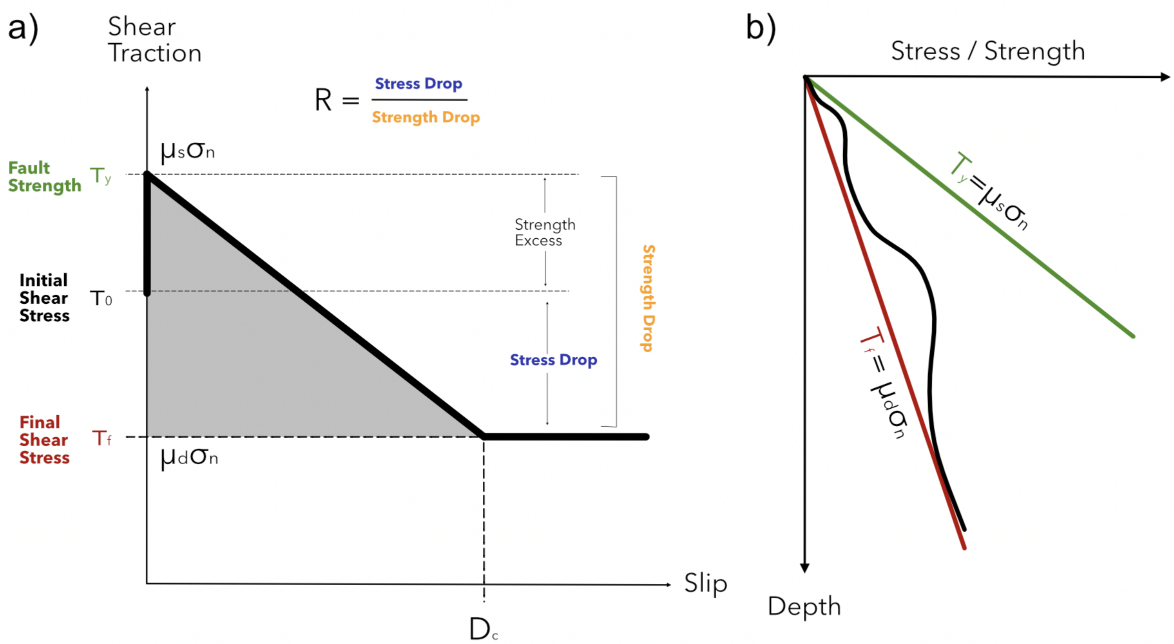

Figure 2.4. A schematic illustration of the relationship between shear traction, shear stress, and shear strength using Linear Slip Weakening laws; a) Shear traction as a function of slip at a single point on the fault. τ_0 is initial stress, τ_y, is fault strength τ_f is the dynamic shear strength, i.e. the final shear stress of the fault. The strength excess is the difference between τ_y and τ_0 that must be overcome for the fault to fail and initiate slip. D_c is the critical distance over which the fault decreases linearly from static to dynamic fault strength b) A schematic profile of shear stress and strength taken as a function of depth taken as a cross-section on some point on the fault at a single point in time. The black line shows a profile of shear stress with depth, τ_y (green) shows a profile of shear strength with depth, τ_f (red) shows a profile of dynamic strength with depth. Figure adapted from Tinti et al. (2021).

2.3.4 Initial Stress State

Following the work of Jia et al. (2023) and Hayek et al. (2024), we consider two main contributions to the stress distribution on the fault surfaces prior to the 2021 event: 1) regional stresses due to the accumulation of long-term regional tectonic loading; and 2) an *a priori* unknown distribution of on-fault stress variations on the fault surfaces which could be driven by the presence of subsurface asperities impacting the accumulation of stress on the fault or remaining stress heterogeneities left from past earthquakes. We develop dynamic rupture models which consider these sources of stress both separately and in combination to better understand their unique contributions to the observed rupture. We expect the regional stress field to broadly encourage left lateral strike slip and thrust motion on the main two faults, while the heterogeneous stress field may provide a more nuanced spatial pattern of stress concentrations. We note that this setup does not explicitly account for any stresses imparted by the 2010 earthquake. Here we describe the theory and methods used for each of these stress sources.

Regional Stress Field

We calculate a tectonically-driven regional stress state across the Peninsula (Fig. 2.6), assuming Andersonian stress conditions, where one principal stress component is assumed to be vertical (Heidbach et al., 2018; Simpson, 1997). We define the regional stress field by orienting SH_{max}, the azimuth of the maximum horizontal compressive stress (measured clockwise from north) and defining ν, the stress shape ratio which scales the relative amplitudes of principal stresses.

The stress shape ratio, ν, is defined as:

$$\nu = \frac{s_2 - s_3}{s_1 - s_3}$$

where s_1, s_2, and s_3, are the principal stress components ordered from largest to smallest. The faulting regime impacts the meaning of ν. For example, in a strike-slip faulting regime, ν=0.5

indicates pure strike-slip, $\nu < 0.5$ indicates tanspression, while $\nu > 0.5$ indicates transtension. The faulting regime depends on which component corresponds the maximum horizontal principal stress SH_{max}, the minimum horizontal principal stress, SH_{min}, and the vertical principal stress component, S_v. In the thrust faulting regime, $SH_{max} > SH_{min} > S_v$, whereas in the strike slip faulting regime, $SH_{max} > S_v > SH_{min}$ (Heidbach et al., 2018) (Figure 2.5).

We calculate the stress tensor at every point on the faults, comprising what we call the ”regional-only” stress field (Fig. 2.6A). We use a stress modulation function, $\Omega(z)$ (Ulrich et al., 2019), to smoothly taper deviatoric stresses to zero at seismogenic depths between 25-28 km, to mimic the brittle ductile transition at the bottom of the seismogenic zone. This depth range is chosen based on the distribution of relocated aftershock seismicity, which is limited, on average, to a depth of 25-30 km (Douilly, Haase, Ellsworth, Bouin, Calais, Symithe, Armbruster, de Lepinay, et al., 2013a). Kinematic slip inversions also found the slip distribution to be limited to above 20 km (Calais, Symithe, Monfret, Delouis, Lomax, Courboulex, Ampuero, Lara, Bletery, Chèze, Peix, Deschamps, de Lépinay, et al., 2022b; Goldberg et al., 2022).

We compare different effective normal stress assumptions (Madden et al., 2022): one where effective normal stress increases with depth throughout the crust with lithostatic stress. Alternatively, we use a fluid over-pressure assumption Madden et al., 2022; Rice, 1992 in which, at depth, the pore fluid pressure gradient mirrors the lithostatic stress gradient, leading to constant effective normal stress at depth. In our implementation of this assumption, we use a pore fluid pressure ratio of $\gamma = \gamma_{water}/\rho = 0.34$ and taper stresses to 52 MPa at 6 km depth (Gabriel et al., 2023). With lithostatic stress conditions, normal stresses continuously increased with depth, causing large normal stresses on the fault at depth and preventing sustained rupture. When rupture did occur, stress drops tended to be extremely large, producing large slip magnitude (>10 m in some cases), supershear rupture and other unobserved effects. When using the over-pressure condition, we observed more realistic stress drops, slip magnitudes, and rupture velocities. We therefore use this fluid over-pressure assumption in all the following simulations.

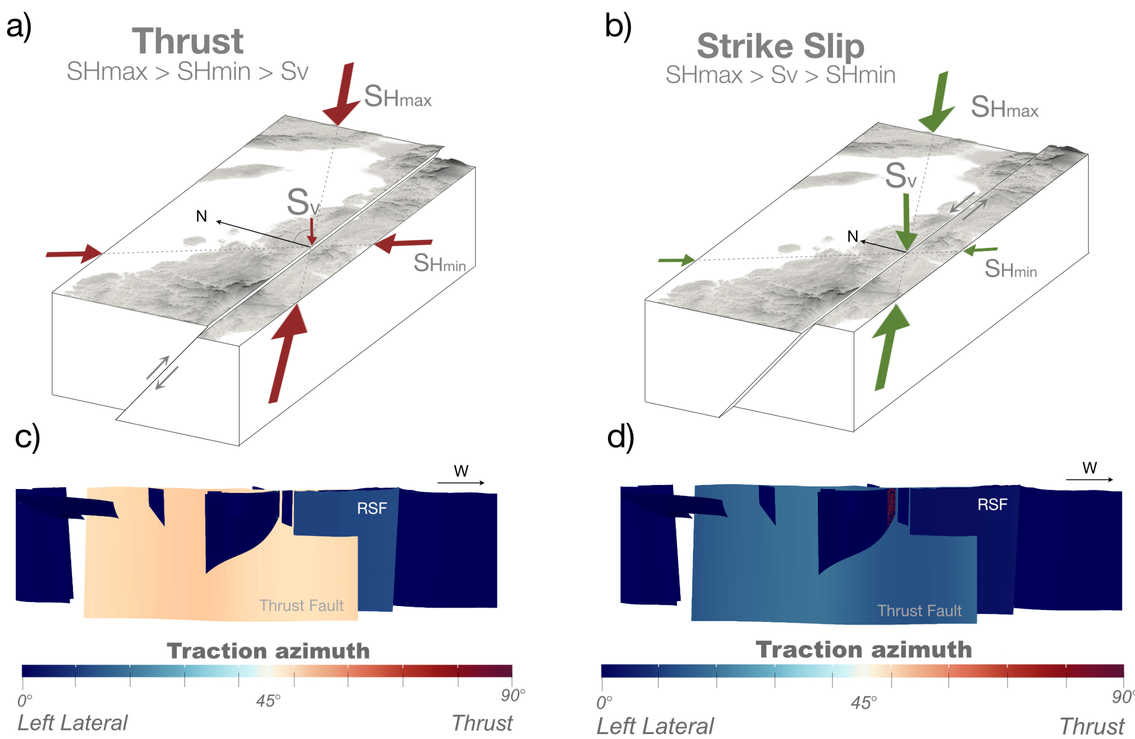

Figure 2.5. a) Schematic of a thrust faulting regime where the minimum horizontal component SH_{min} is larger than the vertical component, S_v; b) schematic of a strike slip faulting regime where the minimum horizontal component SH_{min} is smaller than the vertical component, S_v. The top row shows the relative size of the principal stress components schematically with the topography of Haiti shown on the top face with a simple north-dipping fault schematically representing the TF. The bottom row shows the corresponding shear stresses resolved on the fault surfaces. Bottom left shows a thrust regime with $v = 0.5$, and results in a much higher angle of the traction vector on the north-dipping TF, the bottom right shows a much shallower traction vector, corresponding to a strike slip regime with $v = 0.0$. Adapted from Heidbach et al. (2018).

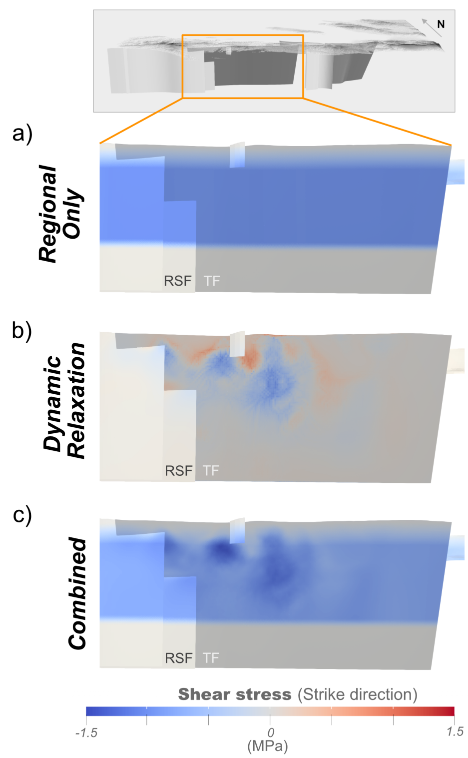

Figure 2.6. Initial shear stresses resolved on the fault surfaces, where negative shear stresses in the strike direction encourage left-lateral slip. : a) tectonically-driven regional stresses, where deviatoric stresses are tapered to zero below the seismogenic depth starting at 25 km depth; b) stresses derived from the dynamic relaxation method; c) the combined regional and slip-driven stresses. The dynamic relaxation method contributes stress heterogeneities which encourage localized slip.

Stress heterogeneity on the fault surface

In addition to regional stresses, we additionally consider the presence of heterogeneities in the initial stresses on the fault. We use a ”dynamic relaxation” technique in which a slip distribution, in this case taken from a static finite fault slip inversion, is assumed to be the result of some heterogeneous stress distribution on the fault plane prior to the earthquake. In order to quantify this heterogeneous pre-event stress distribution, we run a pseudo-static simulation (Glehman et al., 2024; Tinti, Fukuyama, et al., 2005; Yang et al., 2019) using the same computational mesh and the same fault geometry as the subsequent dynamic rupture simulations. The slip distribution is combined with a time dependent slip rate function to impose an interface condition on all faults that slipped and kinematically compute the stress-change time series to find the resulting static stress change. As a result, fault portions which accumulated slip during the 2021 earthquake are assumed to have had pre-stress levels elevated beyond the background stress. This could be due to frictionally locked asperities, heterogeneities in the fault strength due to geology, or other conditions (Fig. 2.6b).

The Raimbault et al. (2023) GNSS and InSAR-derived static slip distribution is used to prescribe slip on the fault. For the numerical calculation, we first project the original Raimbault slip distribution onto the fault surfaces used in this study (which, although similar to the Raimbault et al. geometry, uses a new mesh). We taper the slip at the edges of the fault planes to prevent the generation of stress artifacts. We introduce artificial time dependence to the static slip distribution applying a Yoffe source time function to every slip vector (Tinti, Fukuyama, et al., 2005). We use a rise time of 1 second and a duration of positive acceleration of 0.1 seconds. We then impose this slip distribution with artificial time dependence as a boundary condition on the fault and allow the simulation to run. This is what we call the Dynamic Relaxation simulation. Because the slip vectors on the fault are prescribed, in this method no assumptions are required about the dynamic traction direction (Tinti, Spudich, & Cocco, 2005; Tinti et al., 2021). After all seismic waves have dispersed, we calculate the final volumetric stress tensor at every point in the mesh. We then smooth that volumetric field which still contains some artifacts from the courser discretization of the original Raimbault et al. slip model. We can then use the final stress state from this dynamic relaxation simulation in combination with regional stresses to describe more realistic initial stress conditions on the fault. Dynamic Relaxation-derived stresses are multiplied by a scaling factor, α, which weights the components of the Dynamic Relaxation stress at every point on the faults before being added to the regional stress tensor components.

The resulting slip distribution and synthetic surface deformation field is shown in Fig. 2.7. The slip distribution shows two compact slip patches: one large patch concentrating on the TF and one shallow patch on the RSF. Surface deformation data shows good agreement with InSAR observations, with RMS = 0.089 for A042, RMS=.209 for A043 (likely due in part to unwrapping uncertainties in the interferogram), and RMS=.077 for D138. Surface rupture is visible on a portion of the RSF. We confirm that the moment magnitude, slip distribution, and surface deformations of our dynamic relaxation simulation matches that of the Raimbault et al. (2023) model, and can be used as a reference for subsequent results.

2.3.5 Nucleation procedure

We nucleate rupture at the hypocenter location reported by the USGS on the TF (Goldberg et al., 2022). We force rupture by artificially reducing the friction coefficient at radius r from the hypocenter at the time T given by:

$$T = \begin{cases} \frac{r}{0.7V_S} + \frac{0.081\, r_{crit}}{0.7V_S}\left(\frac{1}{1-(r/r_{crit})^2} - 1\right), & \text{if } r < r_{crit} \\ 1.0 \times 10^9, & \text{if } r \geq r_{crit} \end{cases}$$

Where r is the current distance from the hypocenter, r_{crit} is the forced rupture radius (typically set to 7km in our simulations), and V_S is the shear wave velocity. Velocity varies with distance from the hypocenter which encourages a smooth rupture. The full rupture nucleation method is described in detail in the SCEC/USGS Rupture Benchmarks TPV36 and TPV37 (Barrall and

Harris, 2024).

Table 2.1. Table of parameters and value ranges used in this study.

Symbol	Parameter	Value Range
D_c	Critical Linear Slip Weakening distance	0.02 - 0.06
μ_s	Static coefficient of friction	0.15 - 0.5
μ_d	Dynamic coefficient of friction	0.5 - 0.57
r_{crit}	Nucleation radius	7.0 - 7.5 km
α	Weight of Dynamic Relaxation stresses	0.0 - 0.9
R_0	Scaling of prestress ratio, R, for an optimally oriented virtual fault. Effectively scales regional stress magnitudes.	0.14 - 0.5
SH_{max}	Orientation of maximum principal stress component for regional stress tensor.	40-50°
ν	Stress Shape Ratio	0 - 0.5
C_0	Frictional Cohesion	3-5 MPa at the surface, 0.5 MPa below 6 km depth

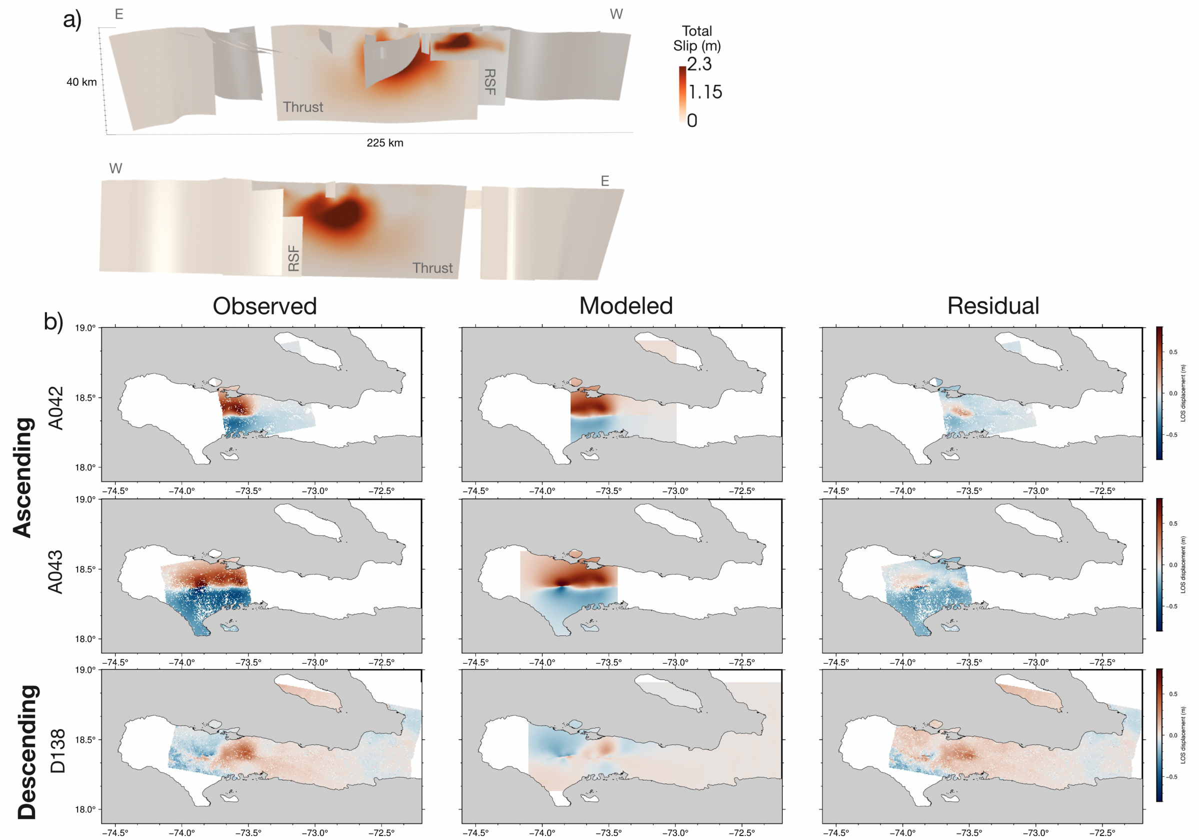

Figure 2.7. Dynamic Relaxation simulation results summary. a) Final slip distribution from the kinematically informed dynamic relaxation simulation. Slip concentrates in one large patch on the TF and one shallow patch on the RSF. Surface rupture is expressed by very shallow slip distribution on the RSF; b) Observed InSAR comparison with simulated LOS surface deformation data.

2.4 Constraining the regional stress state

We seek to orient and scale the regional stress tensor to approximate the broad transpressional tectonic loading of the TF and RSF. The faulting regime in combination with the orientation of the principal horizontal stress component (SH_{max} orientation) and scaling of the principal stress components relative to one another (stress shape ratio, ν) determines the direction of traction (i.e. the direction of shear stress) resolved on the fault surfaces. Past modeling studies in this region have assumed a strike slip faulting regime (Douilly et al., 2015a). SH_{max} orientation for the 2010 earthquake has been estimated using GNSS block modeling and dynamic rupture modeling to be approximately $40-50°$ (Calais et al., 2015, 2023; S. Symithe et al., 2015). However, these assumptions have not been tested for consistency with the 2021 earthquake rupture. Additionally, stress orientations are associated with large uncertainties, at best ± 15° at the surface and ± 25° at depth (Heidbach et al., 2018) and there may be significant variation across the peninsula (Calais et al., 2015).

Therefore, before developing any dynamic simulations, we first conduct a parameter exploration aimed at constraining the orientation and shape of the regional stress field in the vicinity of the 2021 rupture. To do this, we examine the impact of SH_{max} orientation and ν on the direction of traction resolved on the TF and RSF faults. If we assume that the direction of initial shear traction on a fault is parallel to the direction of slip (rake) during rupture, then we aim to find the range of regional stress conditions that produce traction aligned with rake observed during the 2021 earthquake. The rake and direction of traction are both defined according to Aki and Richards conventions (Aki & Richards, 1980) where 0° is pure left-lateral motion and 90° is pure thrust motion (Fig. 2.8). Slip distributions from inversion studies report the rake of the first sub-event to be greater than 40° (a combination of thrust and left lateral motion), while the rake of the second sub-event on the RSF is less than 30° (closer to pure left-lateral motion) (Calais, Symithe, Monfret, Delouis, Lomax, Courboulex, Ampuero, Lara, Bletery, Chèze, Peix, Deschamps, de Lépinay, et al., 2022b; Z. Li & Wang, 2023; Raimbault et al., 2023). We resolve the average traction direction on the TF and RSF for a range of SH_{max} orientations from $30-70°$ and ν values from 0.0 to 0.7, for both the case where $S_v > SH_{min}$ (thrust faulting regime) and the case where $SH_{min} > S_v$ (strike slip faulting regime).

Fig. 2.8 shows the impact of SH_{max} orientation and ν on the direction of the average traction on the RSF and TF in the thrust faulting regime. In the thrust faulting regime, increases in the stress shape ratio, ν, result in a traction vector with a larger dip slip component, while clockwise rotation of the orientation SH_{max} reduces the dip slip component of the traction vector. Changing the orientation of the stress tensor, SH_{max}, also changes the direction of traction across the faults depending on the change in strike along the fault, but the effects are small (±5°, Fig.S3).

Traction direction on the RSF is less sensitive to parameter changes and remains less than 30° in most parameter combinations (Fig. 2.8). We find that in the strike slip faulting regime, the traction vectors generally have an insufficient components of dip slip to match observations. Even when $\nu = 0$ (the transition point between strike slip and thrust faulting regimes where $Sh_{min} = S_v$), the rake on the TF is only 15-20°. This case is explored more fully in the first dynamic rupture simulation (Model 2).

In addition to the alignment of the traction direction to the expected rake, we also consider how the choice of SH_{max} orientation and ν impacts the pre-rupture stress magnitude and strength of the fault. If, for example, stresses on the fault are not large enough to overcome the fault strength, then rupture cannot be sustained. We calculate the pre-stress ratio, R, across the fault surfaces, where higher R indicates that the fault is more likely to sustain rupture. We find that as the traction azimuth increases (closer to pure thrust motion), R tends to decrease (Fig. 2.3). R values are highest for low values of ν in the thrust-faulting regime.

We identify a range of values of ν and SH_{max} that balance agreement between the direction of traction within 15 degrees of the slip model rake while maintaining a high R value: we select values of ν between 0.2 and 0.5 and orientations of SH_{max} between 40-60° in the thrust faulting regime. In subsequent simulations, the modeled surface deformation reproduces the ratio of strike slip to dip slip motion implied by the InSAR data and GNSS observations, confirming this range of regional stress values.

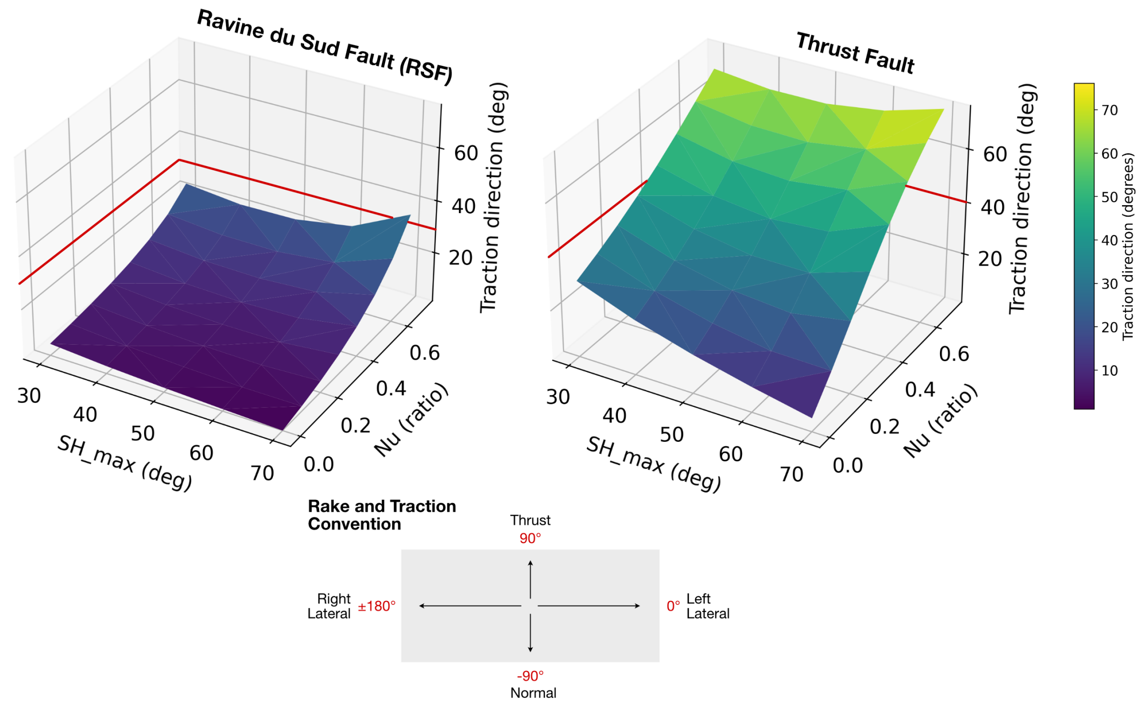

Figure 2.8. Plot showing the impact of SH_{max} and ν on the direction of the average traction vector on both the RSF and TF in the thrust faulting regime; a) on the RSF, the expected traction direction is less than 30° (shown with the red line); b) on the TF, the expected traction direction is greater than 40° (red line); c) schematic of Aki and Richards rake and traction direction convention.

Table 2.2. Parameter values for all models.

Parameter	Model 1	Model 2	Model 3	Model 4	Model 5
D_c	0.03 m	0.05 m	0.06 m	0.06 m	0.02 m
μ_s	0.5	0.57	0.5	0.52	0.52
μ_d	0.15	0.5	0.16	0.16	0.16
r_{crit}	7 km	7 km	7 km	7 km	7 km
SH_{max}	40°	50°	40°	40°	40-50°
ν	0.5	0	0.5	0.5	0.0 - 0.5
R_0	0.4	0.4	0.4	0.4	0.14 - 0.41
α	0	0	0.9	0.9	0.7
C_0	3 MPa	3 MPa	3 MPa	3 MPa	2 - 5 MPa

2.5 Dynamic Rupture Modeling

2.5.1 Modeling Approach

Having identified a range of plausible regional stress parameters (SH_{max} orientation and ν), we now begin designing and running dynamic rupture simulations with the goal of better understanding the conditions which led to the observed 2021 rupture. Our approach for each suite of simulations is to begin with some assumptions about the initial conditions, then run and refine simulations, eventually producing a rupture most consistent with observations given the initial assumptions. By comparing the simulation outputs to key rupture observations, we learn more about rupture dynamics and can then update our assumptions about the initial conditions before running a new suite of simulations. In general, we aim to begin with the simplest assumptions and add complexity to the initial conditions only as needed.

For each simulation, we compare to six key observations and characteristics of the earthquake:

1. separation of strike slip and dip slip motion;
2. unilateral westward rupture;
3. rupture transfer from the TF to the RSF;
4. total moment magnitude (M_w7.2);
5. source time function (detailed below);
6. surface deformation observations (InSAR and GNSS, detailed below).

We compare to the source time functions from Calais, Symithe, Monfret, Delouis, Lomax, Courboulex, Ampuero, Lara, Bletery, Chèze, Peix, Deschamps, de Lépinay, et al. (2022b), Goldberg et al. (2022), and Okuwaki and Fan (2022a). Three InSAR interferogram pairs are used for comparison to model results. JAXA ALOS-2 interferograms are used because the

L-band wavelength of this mission better captures large surface deformations in this highly vegetated region, especially in the near-fault region (Yin, Xu, Haase, Douilly, Sandwell, & Mercier de Lepinay, 2022). Two ascending (A043 and A042) and one descending (D138) path interferograms covering the coseismic period are used from Yin, Xu, Haase, Douilly, Sandwell, and Mercier de Lepinay (2022). GNSS static offset data is taken from campaign data published in Raimbault et al. (2023).

In the following sections we present the results of five dynamic rupture simulations which each represent a major evolution in the initial condition assumptions. We address how each informed our understanding of the rupture dynamics of the 2021 earthquake and the conditions which may have led to it.

2.5.2 Model 1: Regional stress in the thrust regime

We begin with a simple dynamic rupture model where pre-rupture stress conditions across the fault system are defined by a single regional stress orientation and shape. We seek to determine if a single regional stress field, when applied to the assumed complex fault geometry, is sufficient to create dynamic rupture both on the TF and RSF with separated strike slip and dip slip motion. If sufficient, this would imply that the earthquake is primarily a result of the broad regional transpressive stress field in the presence of existing faults.

Based on the results from the sensitivity study in Section 3, this initial model imposes a regional stress tensor oriented at SH_{max} = 40° and with stress shape ratio, ν= 0.5 in the thrust-faulting regime. We expect these conditions to create shear traction and therefore slip on the TF with an average rake of $\sim 51°$ and slip on the RSF with an average rake of $\sim 12°$ (Fig. 2.8), consistent with the expected rake from slip inversions. We vary the values of the remaining parameters to find a combination which sustains dynamic rupture beyond the forced nucleation zone but does not produce an unreasonably large earthquake (i.e. $< M_w = 7.4$). For this model, the parameters we find are $D_c = 0.03$ m, $\mu_s = 0.5, \mu_d = 0.15$, $R_0 = 0.4$, and $C_0 = 3MPa$ at the surface. This results in a $M_w 7.39$ earthquake, which produces slip on nearly the entire TF with an average rupture velocity of $\sim$ 3.5 km/s (Fig. 2.9a). There is a maximum of $\sim$2.5m of slip developing on the fault, which is comparable to estimates of peak slip from slip inversions. However, slip occurs over the entire extent of the TF, resulting in surface deformation that far exceeds that observed by InSAR and GNSS (Fig. 2.9c), and produces significant mismatch with the expected source time function (Fig. 2.9b). Importantly, this scenario fails to reproduce dynamic rupture transfer to the RSF, one of the key characteristics of this earthquake. We therefore conclude that a simple regional stress field does not result in the observed coseismic faulting pattern when all properties of the fault are assumed constant along-strike.

2.5.3 Model 2: Regional stress in the strike slip regime

In order to test which conditions are controlling the transfer of rupture from the TF to the RSF, we again impose a single regional stress tensor, but this time in the strike-slip faulting regime. We select the orientation $SH_{max} = 50°$ and stress shape ratio, $\nu = 0.0$ (i.e. where $S_2 = S_3$), even though, based on the results in Section 3 (Fig. 2.8), we expect that this combination will result in slip on the TF with rake too shallow (i.e. not enough thrust motion) to match surface deformation observations. We again vary the values of the remaining parameters to find a combination which sustains rupture beyond the forced nucleation zone but does not produce an unreasonably large rupture ($< M_w = 7.4$). We find that the following values achieve this balance: $D_c = 0.05$ m, $\mu_s = 0.57, \mu_d = 0.5$, $R_0 = 0.4$, and $C_0 = 3MPa$ at the surface. Note the need to prescribe a relatively dynamically strong fault with a low strength drop ($\mu_s = 0.57$ and $\mu_d = 0.5$) in order to recreate the observed magnitude of slip. If the dynamic coefficient is decreased to make the fault dynamically weaker, then the peak slip on the fault increases to produce unreasonably large earthquakes.

After nucleation, the rupture propagates bilaterally on the north-dipping TF. After approximately 17 seconds of rupture time, nearly the entire TF has slipped on the order of 1 m. The rupture front to the west reaches the termination of the TF, $\sim$15 km west of the intersection with the more steeply dipping RSF. Despite the geometric barrier formed by this intersection at about

$\sim$14 km depth, dynamic rupture successfully transfers to the RSF almost immediately. The final moment magnitude of the earthquake is M_w 7.23, close to the observed moment magnitude of M_w7.2. However, the maximum slip of $\sim$1.4 m is smaller than the expected $\sim$2.3 m and remains relatively constant across the TF and RSF.

In this model, like Model 1, slip on the TF extends over the entire fault as opposed to the expected compact rupture centered around 73.6°W (Fig. 2.10a). This results in a broad first moment rate peak inconsistent with STF estimates (Fig. 2.10b) and does not reproduce inferred troughs and multiple peaks in the source time function. Two to three pulses of slip are inferred in many past studies of the 2021 earthquake, including back-projection results (Okuwaki & Fan, 2022a) and joint teleseismic inversion studies (Goldberg et al., 2022), which indicates that there is at least one delay in moment release which is important to recreate (Fig. 2.10b).

Slip on the TF has a rake of $\sim$16-18° and slip on the RSF has a rake of $\sim$2-3°, closer to pure strike slip motion (Fig. S2). While this change in rake between the TF and RSF reproduces the separation of strike slip and dip slip motion, it fails to produce sufficient thrust motion on the TF to match observations, estimated from slip inversions to be 40+°. The descending LOS image shows this mismatch (Fig. 2.10c), where the observed LOS shows a lobe of positive deformation (consistent with uplift) north of the TF surface trace, whereas the simulated LOS deformation remains negative north of the TF surface trace (Fig. 2.10c, RMS = 0.122). This comparison illustrates that the vertical motion produced by the TF in this simulation must be larger relative to the left lateral motion in the LOS direction to agree with InSAR observations. Producing dynamic rupture transfer coupled with sufficient thrust motion on the TF is difficult with a single regional stress field because the regional stresses required to produce enough thrust motion on the TF to match the observations, tend to result in very low pre-stress levels on the RSF (i.e. low R). This is shown in Fig. 2.3, which compares the initial values of R resolved on the fault surfaces for Model 1 and Model 2. Model 1, which produces the correct rake on the TF has near-zero R values on the RSF, which explains why it does not rupture easily. Model 2, which produced rupture transfer but insufficient dip slip motion on the TF has relatively high R

values on both TF and RSF.

Regardless of the faulting regime, both Model 1 and Model 2 simulations with a single regional stress tensor produce an extended duration and length of rupture on the TF that is not consistent with the observations. This is evident when comparing the slip distribution from Raimbault et al. (2023) (Fig. 2.7a) to the slip distribution for Model 2 (Fig. 2.10a) and Model 1 (Fig. 2.9a).

This simulation illustrates that the stress shape ratio ν is a key factor controlling the transfer of rupture from the TF to the RSF. Therefore, some along-fault variation in the initial stress and strength state or the shape and orientation of the regional stress tensor may be contributing rupture transfer and the compact nature of the resulting slip patches.

2.5.4 Model 3: Combined Regional and Kinematically Informed Heterogeneous Stresses in the Thrust Regime:

It is impossible to know the true initial stress state on the fault surfaces prior to the earthquake. However, we can carry out an experiment to see how initial stress heterogeneity may influence the dynamic rupture. In Model 3, we introduce stress heterogeneity on the faults determined from a static slip model (Raimbault et al., 2023) using a Dynamic Relaxation simulation (Sec.2.3.4). The introduction of these stresses adds variation to the background regional stress resolved on the fault surfaces (see Methods section).

We expect that dynamic slip will concentrate more compactly on parts of the fault with higher initial stress, and may encourage rupture transfer onto the RSF due to elevated stress on the RSF where slip is expected. For this simulation, we chose a regional stress field oriented with $SH_{max} = 40°$ and ν= 0.5 in the thrust faulting regime. We weight the Dynamic Relaxation-derived stresses using α=0.9. Given these conditions, the combination of parameters which sustains rupture but produces a $< M_w = 7.4$ event is: D_c = 0.06, μ_s = 0.5, μ_d = 0.16, R_0 = 0.4, and $C_0 = 3MPa$ at the surface.

After nucleation, the TF ruptures away from the hypocenter bilaterally. Within 20 seconds, the western rupture front has reached the intersection with the RSF but fails to transfer. By 30 seconds it has ruptured the entire extent of the TF. However, unlike previous ruptures, in this simulation slip concentrates in patches near the center of the TF (∼73.6°W), with a peak slip of ∼2.4 m which decreases away from the center of the fault (Fig. 2.11a) and final moment magnitude $M_w 7.31$. This results in better agreement with the InSAR data, where deformation is concentrated over the observed coseismic region (Fig. 2.11c). However, the entire TF still ruptures, creating disagreement with the extent of deformation in the InSAR observations (where the simulation creates surface deformation which extends further to the east and west compared to the observations) and the width of the single moment rate peak (which is much wider when compared to the observations, shown in Fig. 2.11b). The combination of rupture transfer from the TF to the RSF with $40+^{\circ}$ rake on the TF remains elusive.

Model 3 illustrates that initial stress heterogeneity can act to concentrate slip at particular locations on the fault but does not appear to control the extent of rupture, nor is it alone sufficient to transfer rupture from the TF to the RSF. However, stress heterogeneity significantly slows the average rupture speed in Model 3 compared to Model 2, resulting in more realistic moment rate release.

2.5.5 Model 4: Introducing fault strength variations

When constructing the fault geometry, we purposely extended the TF fault past the limits of the observed rupture in order to understand what factors influence the extent and location of rupture (Fig. 2.2). In all experiments to this point, slip on the TF extended to the limits of the fault specified in the geometry, well beyond the actual rupture. It was also difficult to reproduce the timing of the rupture transfer from the TF to the RSF. In this experiment, we introduce heterogeneities in the along-fault frictional properties on the TF to investigate whether a change in fault properties that limits slip to the east and west could be a key factor influencing rupture transfer to the RSF and the extent of slip. We note that, due to dynamic-trade-offs, choosing an increased mu_s may also be a proxy for locally lower initial shear stresses, e.g., reflecting stress shadows of previous regional earthquakes (e.g., Taufiqurrahman et al., 2023), or unmodelled changes in fault geometry. What we represent in this model as changes in fault strength could alternatively represent termination of the TF or changes to the strike or dip of the TF structure at these locations.

The InSAR data (the main observation indicating the rupture extent) shows minimal surface deformation close to the mapped EPGF approximately east of 73.4°W (point Y in Fig. 3.1b) and west of 73.8°W (point X in Fig. 3.1b) (Fig. 2.13c). In Model 4, we increase the static fault strength (μ_s) to 1.0 east and west of these locations to discourage rupture propagation. We otherwise leave $\mu_s = 0.52$ as in previous simulations. The extent of these static strength changes are shown in Fig. 2.13d. All other parameters are identical to the previous simulation (Model 3).

After nucleation, the dynamic rupture propagates on the TF, however, instead of rupturing bilaterally as in previous simulations, the rupture front quickly encounters the increased static strength of the fault to the east (east of point Y on Fig. 3.1b), limiting slip extent. To the west, after about 15 seconds, the rupture front encounters increased static strength west of point X (Fig. 3.1b), limiting the rupture. Despite the rupture propagating past the beginning of the intersection with the RSF, it does not transfer to the RSF fault. The limitation of the spatial extent of the slip on the TF creates a compact rupture that reproduces the surface deformation pattern in the eastern part of the rupture (Fig. 2.13c). These increases in fault strength also result in a narrower moment rate pulse which more closely resembles the first peak of the Goldberg et al. (2022) source time function (Fig. 2.13b). The maximum slip is $\sim$2.3 m, similar to the Raimbault et al. (2023) slip distribution, and the limited lateral extent of slip means that the moment magnitude of the rupture is smaller, $M_w7.10$. This is less than the observed $M_w7.2$ rupture but that is expected given the non-rupture of the RSF.

We find that the lack of rupture propagation from the TF to the RSF is a persistent feature of all ruptures which assume a thrust faulting regime with a high stress shape ratio (ν =0.3 - 0.5, not all simulations shown). This remains true even when the strength of the RSF is reduced, and when the pre-stress levels on the RSF are increased (achieved by increasing R_0). The lack of RSF rupture in the Model 4 simulation is evident in the mismatch between the simulated and observed InSAR data (Fig. 2.13c). The simulated InSAR data produces no surface rupture on the RSF as opposed to what is observed in track A043 (RMS=0.276). We also note the lack of multiple moment rate peaks in the source time function (Fig. 2.13b) and that there is a mismatch at the two GNSS sites, CAMR and CAMY, just south of the RSF (Fig2.14a). GNSS vectors very close to a fault are often difficult to match exactly, for example due to fault fling (e.g. Calais et al., 2010a). The fit to stations CAMR and CAMY might be improved by further refining the details of the western termination of the RSF. Despite the non-rupture of the RSF, the lobe of uplift which is readily apparent in the Descending InSAR Scene is reproduced by the increased shear strength of the eastern portion of the TF (RMS=0.079). The simulated GNSS data surrounding the rupture on the TF demonstrates a close match to the observed data (Fig. 2.13a). Model 4 demonstrates that changes in friction along the TF is one way to implement along-strike variations in fault properties and effectively limits the rupture extent.

2.5.6 Model 5: Combined Regional and Kinematically Informed Heterogeneous Stresses with Lateral Variation in Regional Stress Field

In all previous simulations in the thrust faulting regime, dynamic rupture did not transfer to the RSF. The following experiment tests the hypothesis that an along-strike change in the regional stress field would favor rupture transfer while preserving the large amount of dip slip motion on the TF.

We combine the stress conditions that produced rupture transfer from the TF to the RSF in Model 2 and the conditions which produced sufficient thrust motion on the TF in Model 4. To do this, we set SH_{max} = 50°, ν = 0.0 on the RSF and SH_{max} = 40°, ν = 0.5 on the TF, both in the thrust faulting regime. We calibrate the value of R_0 individually on each fault to ensure reasonable slip on both segments, using R_0 = 0.14 on the RSF and R_0 = 0.41 on the TF (and all other faults). We lower R_0 to 0.14 on the RSF to prevent slip from becoming too large after rupture transfer. In this simulation we also increase the frictional cohesion (C_0) near the surface on the TF to 5 MPa to better reproduce the smooth transition across the TF without obvious surface rupture. We decrease the frictional cohesion near the surface on the RSF to 2 MPa to better reproduce the sharp surface rupture across the RSF observed in the InSAR data (Fig. 2.15). We find that there is only a very narrow range of parameters that both allow rupture propagation to the RSF but generate a reasonable slip magnitude on the RSF. We ultimately find an appropriate combination of parameters: D_c = 0.02, mu_s= 0.52, mu_d=0.16, α = 0.7.

This rupture, like Model 4, begins with largely unilateral rupture to the west. After about 10 seconds, the rupture reaches the intersection between the RSF and TF (Fig. 2.13d) and soon after encounters increased static friction west of point **U** (Fig. 2.16). Here, the rupture almost stops but eventually begins to slip at the intersection between the RSF and TF. The rupture on the RSF slips slowly at first, then accelerates toward the surface of the RSF. Slip on the RSF has rake ranging between ∼40-60°, and slip on the TF has rake ranging between ∼0-30°. This period where the rupture encounters the intersection of the RSF and TF corresponds to the trough in the source time function expected from the teleseismic data at about 10 seconds (Calais, Symithe, Monfret, Delouis, Lomax, Courboulex, Ampuero, Lara, Bletery, Chèze, Peix, Deschamps, de Lépinay, et al., 2022b; Goldberg et al., 2022; Okuwaki & Fan, 2022a).

Several additional simulations which are not shown adjusted the location of point **T** (Fig. 2.13) where static friction increase begins, to better understand its relationship to rupture transfer, timing, and fit to the InSAR data. We find that when introducing an increase in μ_s on the TF further to the west, rupture extends further to the west before transferring to the RSF. This is inconsistent with the InSAR data which indicates that there is no subsurface rupture that far west. When the μ_s on the TF increases west of point **T**, we find that the rupture transfers more quickly to the RSF, resulting in a better fit to the moment rate and better fit to the InSAR data. Even with these adjustments, there is still some disagreement with the InSAR data at the western edge of the TF, west of point **X** (Fig. 2.15c and 2.14b). We find that it is difficult to reproduce the concentrated slip near the surface on the RSF which is observed in the InSAR data. This remaining discrepancy causes some misfit between the modeled surface deformation and the InSAR and GNSS data near the Ravine du Sud fault (Fig. 2.15c, RMS=0.213 for A043, RMS=0.093 for D138). However, the simulated rupture from Model 5 has otherwise strong agreement with all observations: InSAR surface deformation, GNSS offsets, and source time function. It also reproduces all of the key characteristics of the earthquake: separation of strike slip and dip slip motion on two separate fault planes, rupture transfer to the RSF, and source time function.

We use the dynamic rupture model to explore potential explanations for the rupture transfer from TF to the RSF. We extend the meshed fault surface for TF westward to point **U** (Fig. 2.13d), well beyond the intersection with RSF at **T** (Fig. 2.13d), and thus allow slip to continue on the TF if dynamic conditions are favorable. Many simulations lead to the rupture continuing on the TF past the intersection to **U**, producing a prolonged first peak in the modeled source time function, and delaying rupture propagation onto the RSF until reaching the end of the meshed TF at **U**. This produced a delay in the second pulse of slip in most source time functions (i.e. Raimbault et al., 2023) and backprojection sources (Okuwaki & Fan, 2022a) and also produced surface deformation that disagreed with InSAR observations near the RSF. Increasing the static friction coefficient on the TF westward of point **T** near intersection with the RSF is sufficient to transfer rupture to the RSF earlier and reproduces the timing of the second pulse of moment release. The mechanism producing this effect could be a change in the fault properties or termination of the TF or a change in the fault geometry at this location. There are several step-overs in the EPGFZ surface fault traces at this location to support this change in geometry.

The main result is therefore that a significant change in the regional stress field is necessary to produce the observed slip on the RSF in our fault geometry as well as some variation in along-strike dynamic parameters such as fault strength.

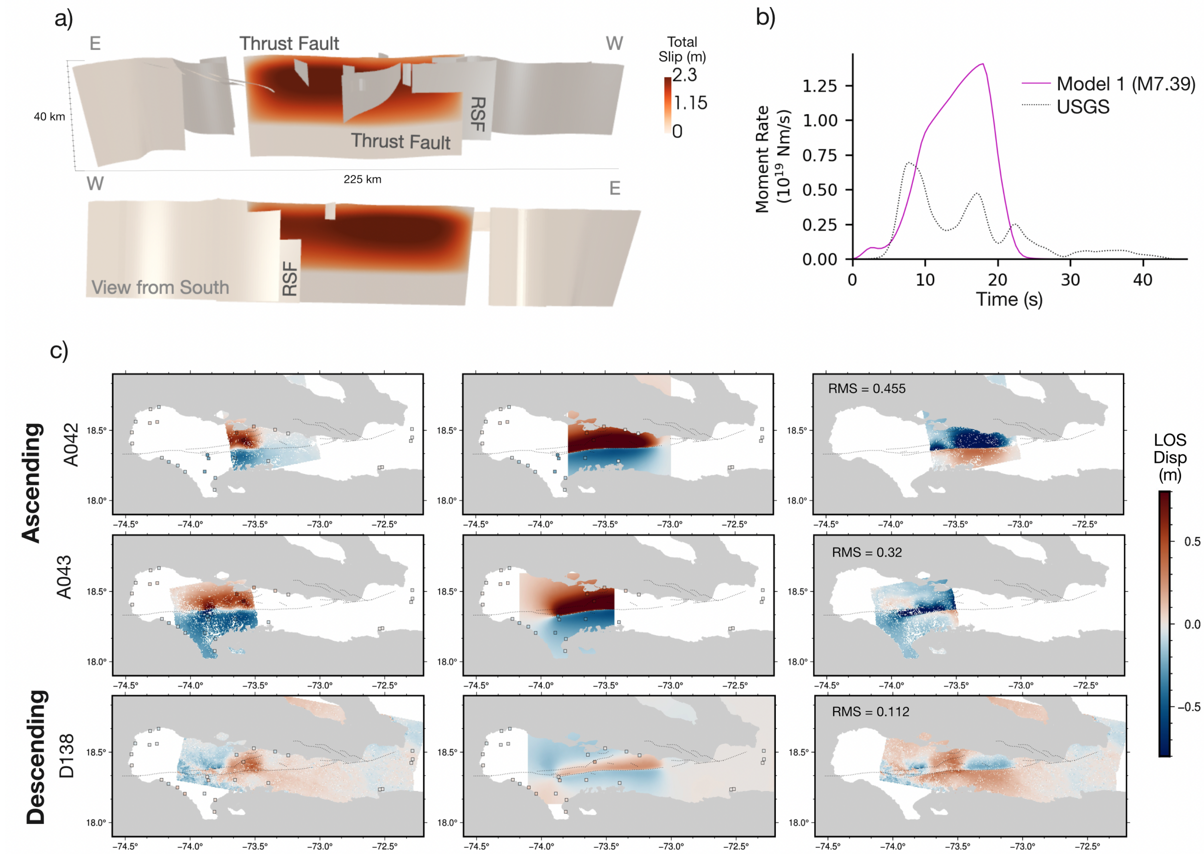

Figure 2.9. Summary of results from Model 1: Regional stresses in the thrust regime a) Final slip distribution. Slip is distributed evenly over the entire TF, no rupture transfer to the RSF; b) source time function comparison between the Goldberg et al. (2022) model (grey) and this model (purple). Overall rupture moment magnitude is too large and there are no distinct pulses, unlike the Go23 source time function; c) Observed InSAR data from ALOS-2 tracks A042, A043, an D138 compared with simulated LOS surface deformation data. Overall magnitude of surface deformation is too large, creating a large misfit in pattern andmoment magnitude between the modeled deformation and observed deformation, seen as large residuals.

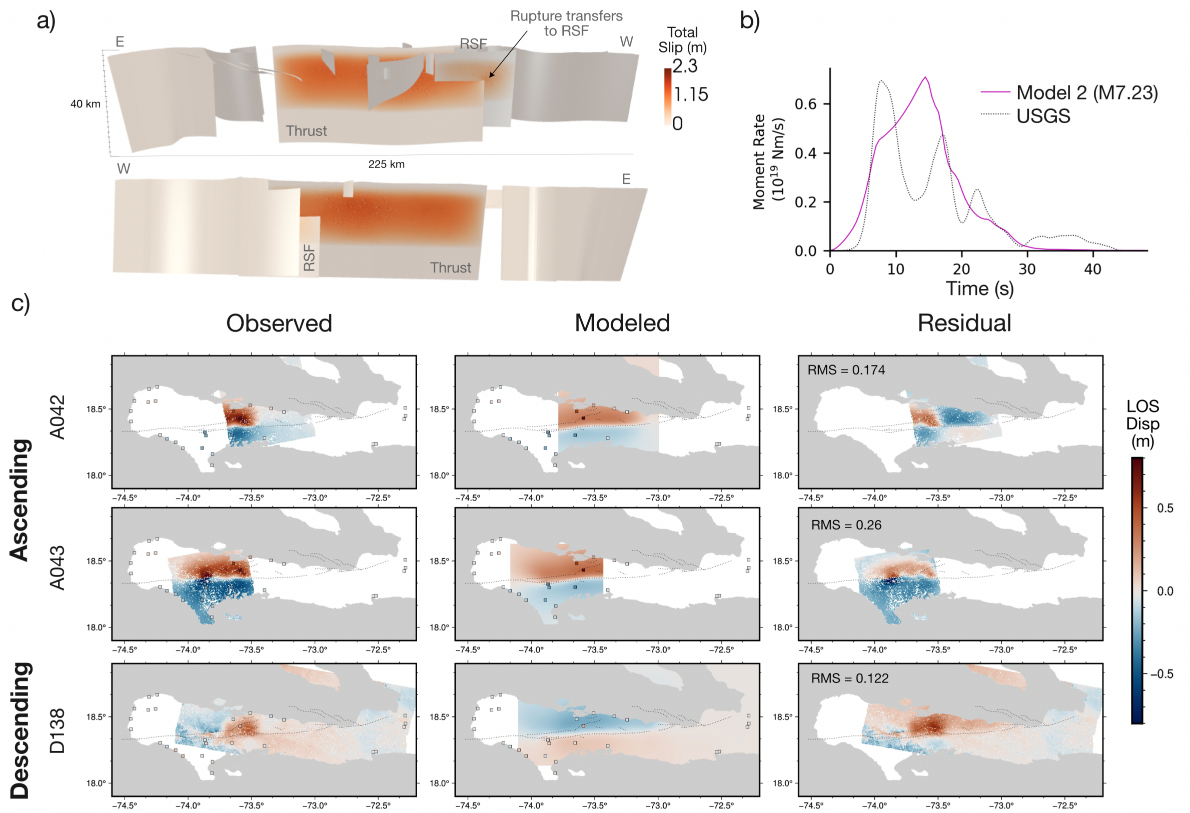

Figure 2.10. Summary of results from Model 2: regional stresses in the strike slip faulting regime: a) Final slip distribution for Model 2. Slip is distributed evenly over the entire TF and rupture has propagated to the RSF with significant slip; b) source time function comparison between the Goldberg et al. (2022) model (grey) and this model (purple). Overall rupture moment magnitude is captured but without distinct peaks, unlike the Go23 source time function; c) Observed InSAR comparison with simulated LOS surface deformation data. Amplitude of residuals is decreased with respect to Model 1, however there remains a strong misfit in the pattern between the modeled deformation and observed deformation. The descending pair (D138) shows negative deformation in the LOS direction of the observing satellite whereas we expect a lobe of positive deformation from strong thrust motion the TF as seen in the observed interferogram. This indicates the stress orientation plays a role in producing later slip on the RSF which contributes to creating a peak later in the source time function.

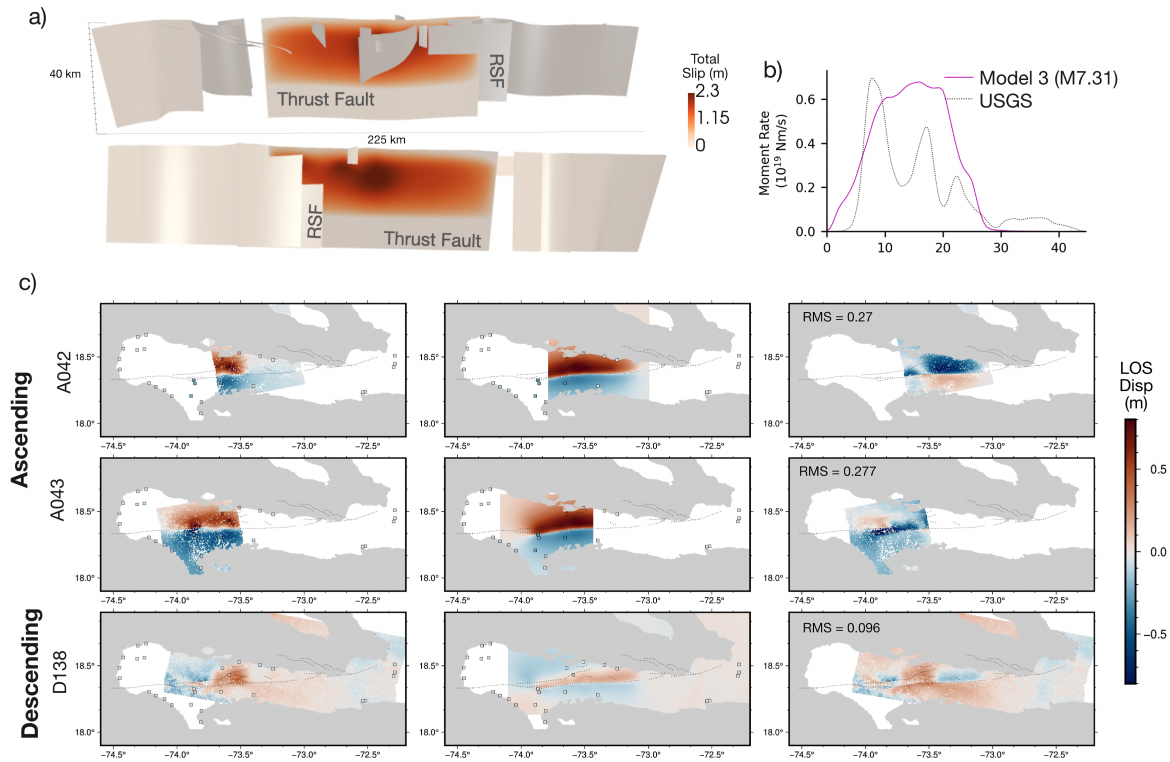

Figure 2.11. Summary of results from Model 3: Combined regional and dynamic relaxation (DRT) stresses in the thrust regime a) Final slip distribution for Model 3. While slip still extends over the entire length of TF, slip concentrates near the center of the fault. There is no rupture transfer to the RSF; b) source time function comparison between the Goldberg et al. (2022) model (grey) and this model (purple). The peak of the source time function is roughly the right amplitude but there are no distinct peaks and the single peak is too wide; c) Observed InSAR data from ALOS-2 tracks A042, A043, an D138 compared with simulated LOS surface deformation data. Overall magnitude of surface deformation remains too large, but uplift, seen as a red lobe in the simulated track D138 data, is broadly reproduced. This indicates that concentrating the dip-slip motion in lateral extent is important for reproducing the InSAR pattern with dip-slip dominating strike-slip motion in the surface deformation.

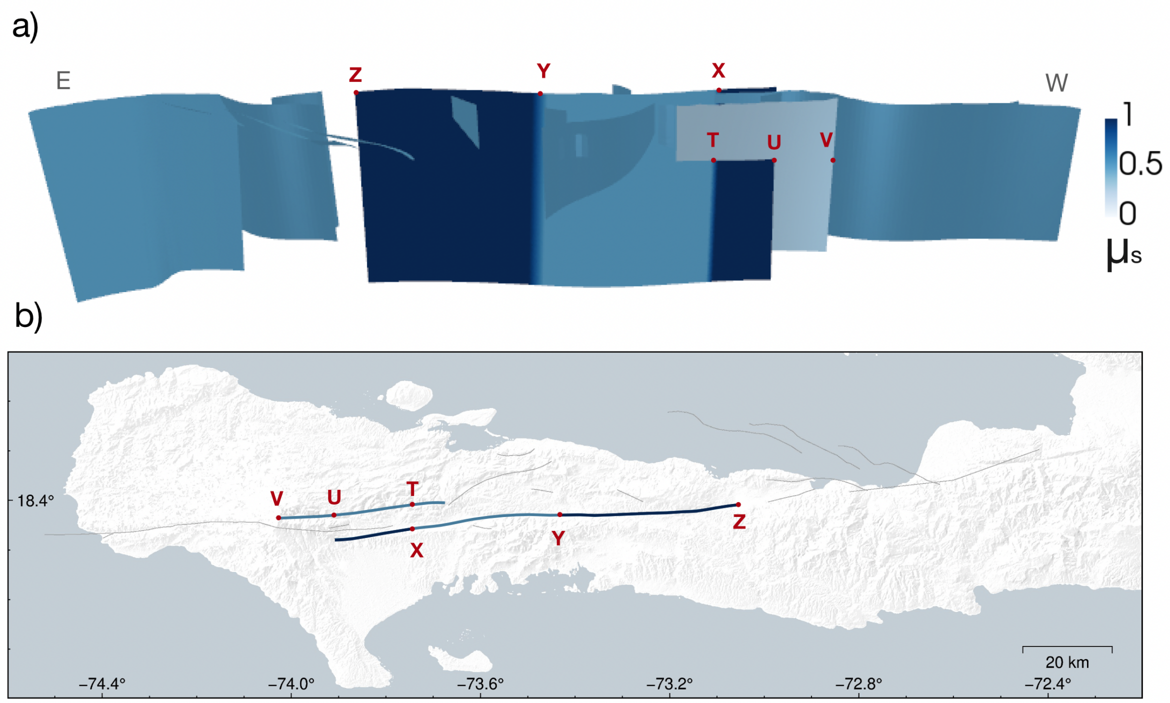

Figure 2.12. Variable static coefficient of friction on the fault surfaces. This distribution of μ_s is used in both Model 4 and Model 5. Points of interest T, U, V, X, Y, and Z are shown in red.

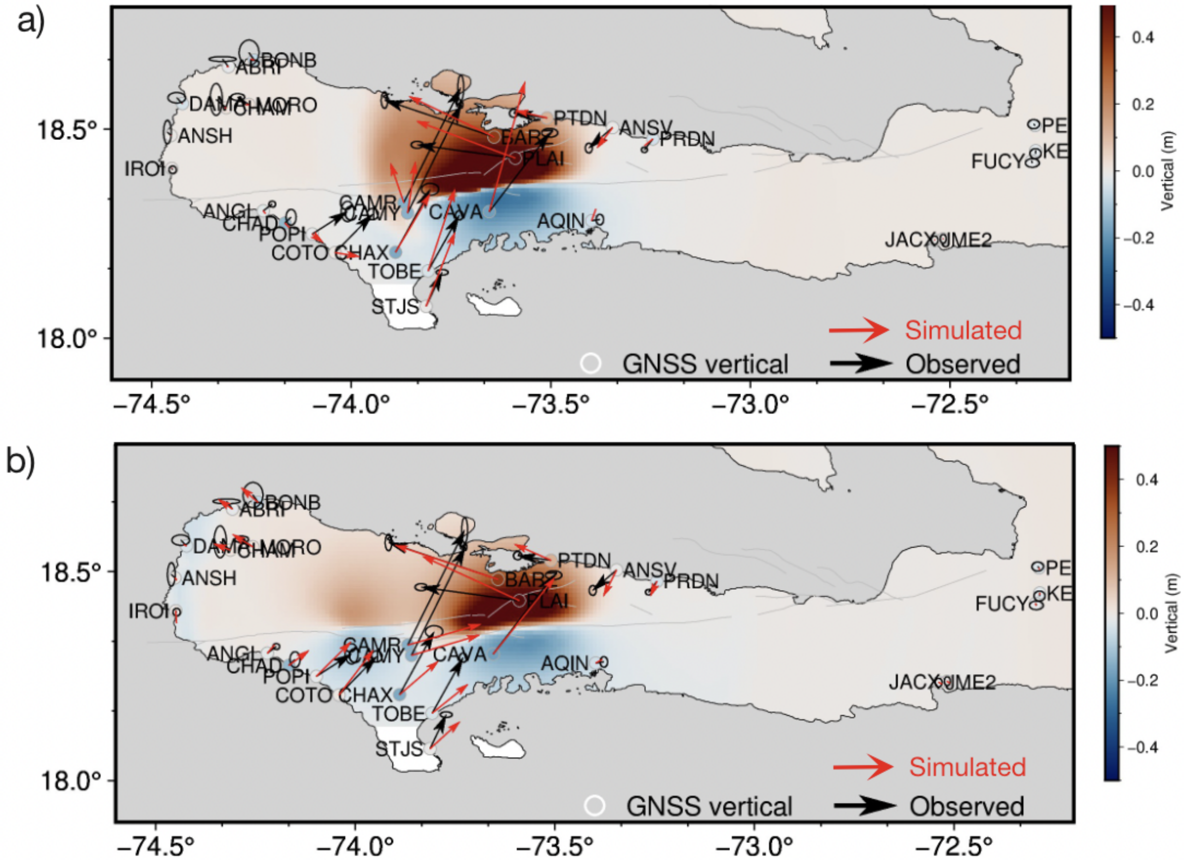

Figure 2.14. Comparison between observed GNSS coseismic offsets (horizontal deformation shown with black arrows, vertical deformation shown by color of circles) and simulated offsets (horizontal deformation shown with red arrows, vertical deformation shown as the background gridded red/blue data). a) Model 4 comparison; b) Model 5 comparison.

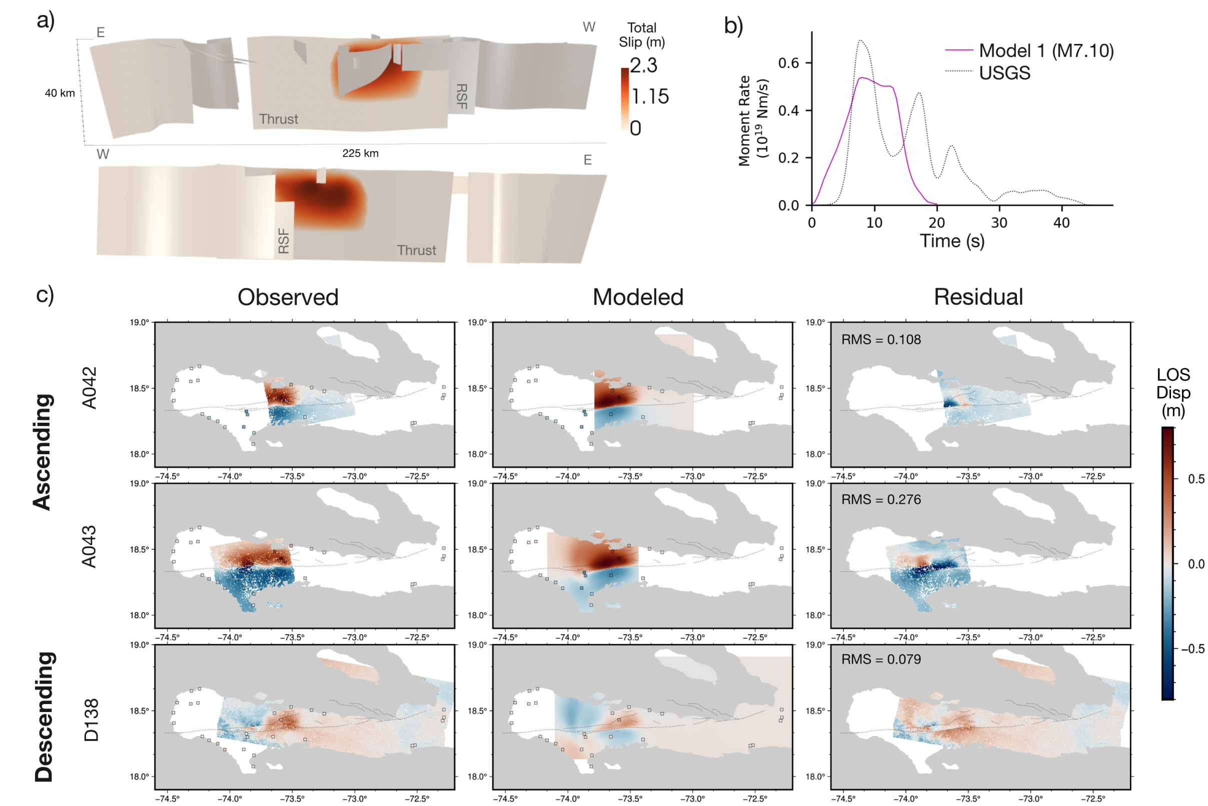

Figure 2.13. Summary of results from Model 4: combined regional and DRT stresses in the thrust faulting regime with fault strength variations: a) Final slip distribution for Model 4. Slip patches are more compact than in Model 2, but there is no rupture transfer and therefore no slip shown on the RSF; b) source time function comparison between the Goldberg et al. (2022) model (grey) and this model (purple). Overall moment magnitude is captured but there are no distinct peaks in the source time function, unlike the Go23 model; c) Observed InSAR comparison with simulated LOS surface deformation data. Modeled surface deformation data closely matches the observations in amplitude and pattern. In particular, the synthetic descending LOS deformation (D138) shows a lobe of positive deformation in the LOS direction of the observing satellite which agrees with the observed interferogram. This indicates that a limited rupture extent on TF contributes to matching the pattern of uplift;

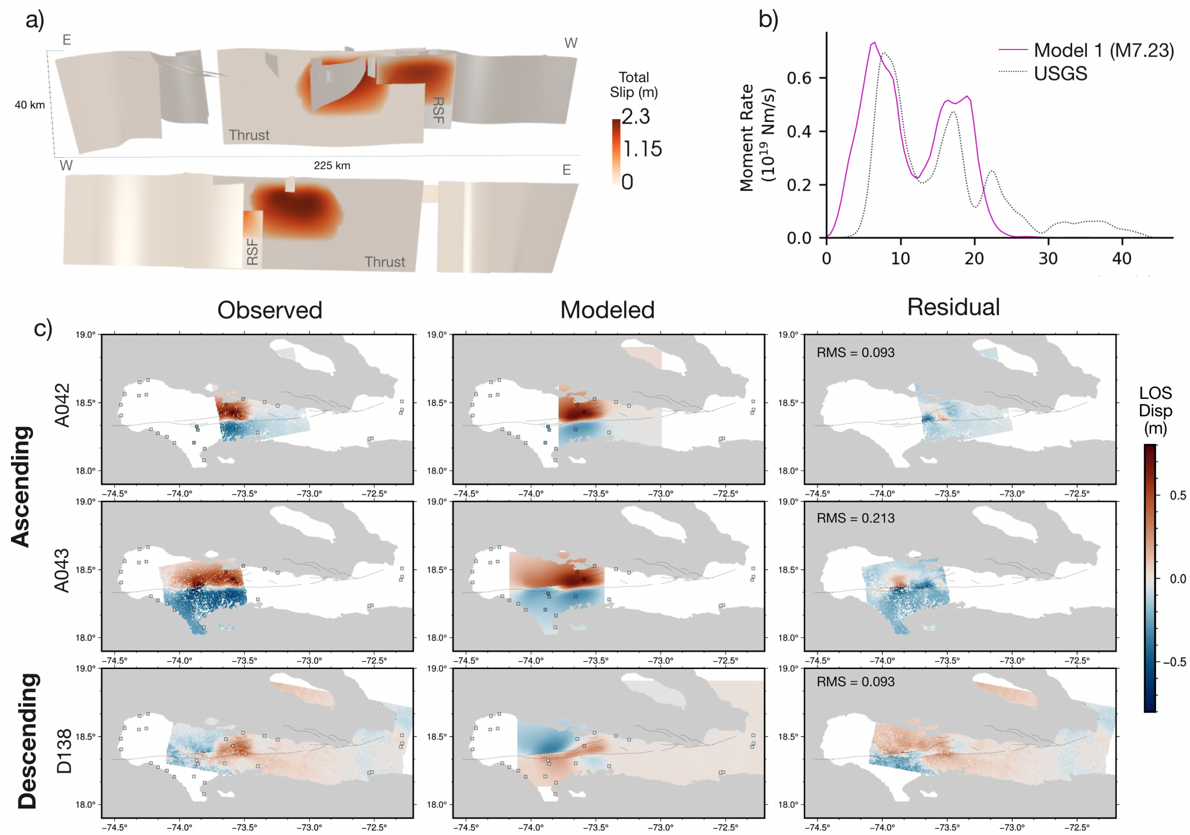

Figure 2.15. Summary of results from Model 5: Lateral variations in regional stresses combined with DRT stresses and fault strength variations: a) Final slip distribution for model 5. Slip patches concentrate compactly on the TF and RSF, where slip on the RSF indicates successful rupture transfer b) source time function comparison between the Goldberg et al. (2022) model (grey) and this model (purple), where there is good agreement in the moment magnitude and timing, and where the two distinct peaks in the source time function correspond to the rupture transfer from TF to RSF; c) Observed InSAR comparison with simulated LOS surface deformation data. Modeled surface deformation data closely matches the pattern and amplitude of the observations, with the synthetic descending LOS deformation (D138) showing the expected lobe of positive deformation in the LOS direction. The deformation now matches the InSAR deformation in the narrow region between the RSF and TF.

2.6 Discussion

2.6.1 Interpretation of the Thrust Fault

One important unresolved question about the 2021 earthquake is the relationship of the Thrust Fault to the previously assumed vertical EPGF (Prentice et al., 2003; Saint Fleur et al.,

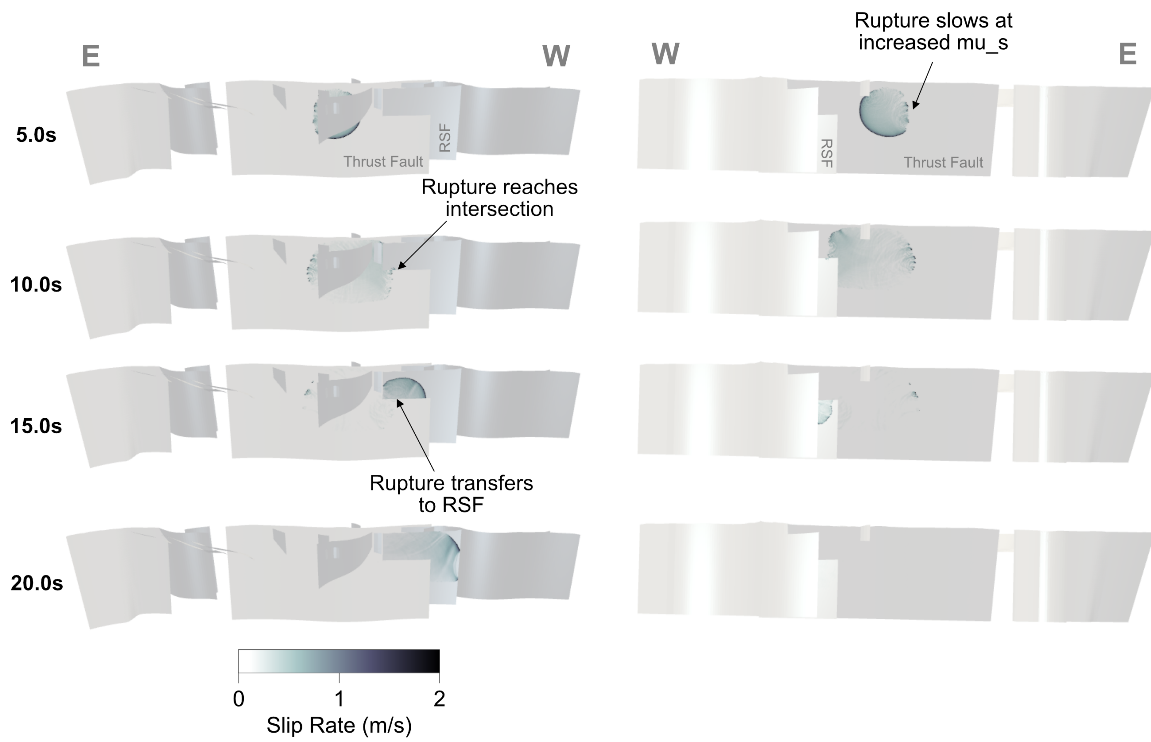

Figure 2.16. Snapshots of absolute slip rate for Model 5. Left column shows a view from the north and right column shows a view from the south. Rupture nucleates on the TF, at 10 s reaches the intersection with the RSF where the slip rate decreases before, at 15 sec, rupture transfers to the RSF and slip rate increases as the rupture propagates upwards before terminating at around 20 sec.

2020a). The same question was asked about the 2010 Léogane fault. The fault system geometry has major implications for understanding how this margin accommodates transpression. The Thrust Fault used in our model roughly follows the trace of the EPGF (Saint Fleur et al., 2020a), and continues at depth dipping 66°N, constrained such that it roughly follows the aftershock locations (Douilly et al., 2023). The fault is represented as a single, nearly planar feature as in Raimbault et al. (2023). The ability of Model 5 to reproduce observations of the 2021 event suggests that the TF geometry with our proposed modifications represents one possible geometry.

As more detailed aftershock locations became available (Douilly et al., 2023), they suggested that at depth this fault is likely not planar but can instead be interpreted as two or three planes that more closely follow aftershock clusters. This kind of variation of fault strike could also terminate of limit the extent of fault rupture, which we reproduced by varying fault friction. There is also a small subset of aftershocks that lie in a vertical plane below the EPGF fault trace east of the rupture that may indicate the presence of a separate EPGF. In this conception, the vertical EPGF would produce the persistent topographic features observed and, over geologic time, would take up the motion of a larger earthquake.

It remains unclear if this north-dipping fault, whether comprised of a single planar segment or multiple segments, is itself the EPGF or a parallel strand running alongside the vertical EPGF. The possibility of two parallel faults with different dips has different implications for understanding the long-term accommodation of strain across the peninsula.

Designing new meshed fault geometries would be an important undertaking for expanded dynamic rupture modeling experiments to help address these different hypotheses. This study serves as a guide for the level of detail and scope of simulations that could supplement such future studies.

The results of our modeling suggest that the TF we proposed is subject to transpressive regional stresses which are most closely approximated by a thrust-faulting stress regime with a stress shape ratio ν=0.5 on this fault. Recent GNSS work from Calais et al. (2023) proposed two possible block models in which shortening is either accommodated almost entirely by the

Jeremie-Malpasse thrust fault off the north-shore of the Tiburon peninsula or an alternative model where compression and strike slip motion are both accommodated along the EPGF. Our model results support the interpretation that significant shortening is acting as far south as the mapped EPGF, as opposed to being entirely accommodated by offshore thrusts, like the Jeremie-Malpasse fault to the north (Calais et al., 2023).

Including significantly longer fault segments in the model than actually ruptured in the main earthquake led to several challenges in reproducing the observed behavior. However, it also led to a more in-depth understanding of the controls on fault rupture. For example, had we made the assumption in advance that the TF terminated at the start of the RSF then rupture would likely have transferred to the RSF without an investigation of the many factors that control that transfer.

2.6.2 Unruptured Miragoâne Segment

The Thrust Fault was designed to extend from Massif Macaya all the way to Lake Miragoâne (Fig. 3.1) and dips 66°N. This distance is considerably longer than the extent of the known rupture from InSAR data (Fig. 3.1b). From the Basin of L'Asile to Lake Miragoâne, we increase the static friction coefficient in Models 4 and 5 in order to terminate rupture where surface deformation becomes negligible in the InSAR data. Increasing μ_s or decreasing initial shear stresses locally to terminate rupture is a common approximation used in dynamic rupture modeling, particularly when using a LSW friction law, where there is no mechanism to account for velocity-strengthening rheology of the fault that may decelerate dynamic rupture (e.g., Galis et al., 2019). The segment of the EPGF between the 2010 and 2021 ruptures is puzzling because both earthquakes were estimated to have increased the Coulomb Failure Stress here (Calais, Symithe, Monfret, Delouis, Lomax, Courboulex, Ampuero, Lara, Bletery, Chèze, Peix, Deschamps, de Lépinay, et al., 2022b; S. J. Symithe et al., 2013a). Interestingly, the west and the east ends of this unruptured segment also slipped shallowly in the weeks following the 2010 and 2021 earthquakes, respectively (Wdowinski & Hong, 2012; Yin, Xu, Haase, Douilly, Sandwell, &

Mercier de Lepinay, 2022). It is critical to understand whether this segment is locked and highly hazardous, or whether it is accommodating strain differently than the surrounding segments.

One explanation could be that the the eastern edge of the 2021 rupture simply marks the end of the TF where it intersects with the vertical EPGF. This change in geometry could prevent the propagation of the rupture onto the unruptured segment. This interpretation is supported by the change from north-dipping to vertical clusters of aftershock seismicity east of the rupture (Douilly et al., 2023). A change in fault dip could also make rupture transfer less dynamically feasible, as we showed was the case for the rupture transfer between the north-dipping TF and vertically-dipping RSF, which would explain the eastern termination of the rupture. Another possibility is that the unruptured segment is relatively weak and, for example, creeping at depth such that there is little stress remaining to be released to continue the rupture. However, the GNSS velocity transects across the fault do not indicate interseismic creep (Calais et al., 2015). A third possibility is that this segment ruptured most recently (i.e. 1770, Hough et al., 2023) and stress has not yet recovered.

2.6.3 TF West of the 2021 Rupture

In Models 4 and 5, we increase the static coefficient of friction west of the rupture as seen in the InSAR. Increasing the static fault strength of this section was required to match the InSAR surface deformation field and GNSS coseismic offsets and reproduced the timing of the first trough in the modeled source time functions (Calais, Symithe, Monfret, Delouis, Lomax, Courboulex, Ampuero, Lara, Bletery, Chèze, Peix, Deschamps, de Lépinay, et al., 2022b; Goldberg et al., 2022; Okuwaki & Fan, 2022a). The dynamic rupture models demonstrated a need to increase the static strength of the west end of the TF that is parallel to the RSF in order to reproduce the observations. This suggests that, while at one point this may have been an active strand of the EPGFZ or part of a flower structure, it is either no longer active or the north-dipping TF ends before this section begins.

Here and for the east end of the TF, the change in frictional properties can be considered a proxy for fault characteristics or features that change that location. The change in characteristics means that segmentation is important, however as the two earthquakes in 2010 and 2021 showed, it cannot be easily interpreted from surface features in advance. This presents challenges for earthquake hazard estimates that include a recurrence model for characteristic earthquakes based on fault length (Wells & Coppersmith, 1994). A statistical approach that accounts for different potential rupture lengths (e.g. Field et al., 2014) is necessary.

2.6.4 Strain Partitioning at the EPGF

The oblique relative motion between the North American and Caribbean tectonic plates creates transpression across Hispaniola. However, there is ongoing debate about how that transpression is accommodated and partitioned among fault systems. While the Enriquillo-Plantain Garden Fault Zone (EPGFZ) has historically been understood to be a vertical fault accommodating only left lateral motion, recent geodetic work, recent re-examination of historical events, and oblique focal mechanisms in the recent 2010 and 2021 earthquakes supports the interpretation that significant crustal shortening and thrust faulting reaches as far south as the EPGF. The partitioning of strain across the region plays a critical role in our understanding or earthquake hazard and risk in Haiti (S. Symithe & Calais, 2016). Recent block modeling of GNSS data proposed two competing block models for this region, but the observations cannot easily distinguish between the two models (Calais et al., 2023).

The historical earthquakes in 1701, 1770, and 1860, were assumed to be strike slip earthquakes which occurred on the EPGF (Bakun et al., 2012). Some have used this to suggest a multi-rupture mode for this plate boundary which alternates between strike slip events on the EPGF and thrust events on secondary faults over the course of centuries (Wang et al., 2018b). However, (Hough et al., 2023) recent re-examination of the 1770 and 1860 events, suggests that these events could have occurred on partially on oblique thrust faults (Hough et al., 2023; Martin & Hough, 2022). This, combined with the knowledge of the 2010 and 2021 events both initiating on north-dipping unmapped thrust faults, suggests that perhaps significant thrust motion is a typical mode of failure for this fault zone. Despite significant geologic field work and other geophysical data collection over the last several decades, there is still high uncertainty in the fault dip through much of the peninsula. Perhaps fault segmentation includes sections of vertical strike slip fault (like the unruptured section) while other sections prefer oblique thrusting. This work supports the interpretation of combined thrust and strike slip motion and adds the constraint that this implies variation in the stress tensor along the plate boundary.

2.7 Conclusions

3D dynamic rupture modeling experiments were used to test which conditions may have contributed to the complex 2021 M_w7.2 Haiti earthquake rupture. We developed a highly complex fault geometry which captured two main coseismic fault surfaces: a north-dipping Thrust Fault (TF) and a near-vertical Ravine du Sud Fault (RSF), as well as a detailed network of surrounding fault segments. The dynamic rupture models were tested against the following observations and characteristics: M_w7.2 moment magnitude, a multi-peak source time function, spatial separation of dip slip and strike slip motion interpreted from surface deformation, surface rupture of the vertical RSF, and GNSS and InSAR surface deformation observations.

Results indicated that regional stress shape and orientation were key influences on both the orientation of slip (rake) and the transfer of dynamic rupture from the TF to the RSF. Regional stress with orientation SH_{max}=40° and ν=0.5 produced shear stress resolved on the TF that best aligned with the surface deformation observations. However, a dynamic rupture model using this simple description of regional stress (Model 1) did not produce the observed slip on the RSF, which suggested that a more complex system was required. While stress heterogeneities localize the simulated slip in closer agreement with the observed surface deformation pattern, they did not impact the lateral extent of rupture or the rupture transfer to the RSF. Changing the assumed orientation of the stress tensor and the stress shape ratio between the RSF and TF faults was required to produce transfer of the rupture to the RSF and to produce shear stresses on the RSF oriented in agreement with the observed rake.

Along-strike variations in fault friction on the TF were key to focusing the slip to the observed geographic patches and producing narrow peaks in the source time function. The change in frictional properties can be considered a proxy for fault characteristics or features that changed at that location, for example a change in orientation or termination of the fault might produce similar results. The change in characteristics means that segmentation is important, however as the two earthquakes in 2010 and 2021 showed, it cannot be easily interpreted from surface features in advance. In fact, the segmentation proposed in Saint Fleur et al. (2020a) does not represent conditions that can lead to a dynamic rupture model that reproduces the observed characteristics.

Combining regional stress changes with along strike variations in fault friction created a major slip patch on the TF and then transferred rupture to the RSF with the right timing to reproduce the source time functions. This model best fit all of the observational datasets. These results assume the dynamic rupture of a thrust fault with 66°N dip. However, this does not preclude the existence of a parallel vertical EPGF, nor does it test any variations in the assumed rupture geometry. Future dynamic rupture modeling efforts may be used to how variations in the coseismic rupture geometry may have impacted the dynamic rupture evolution.

The variability in local stress regime and fault strength implied by the dynamic rupture modeling results suggests that any of the minor or unmapped compressional fault features or strike slip segments located within this highly deformed compressional microplate boundary are candidates for contributing to the release of the accumulated strain. More work is needed to understand how this fault zone is accommodating tectonically driven stresses. Recent efforts to map and categorize these minor faults (Calais et al., 2023; Saint Fleur et al., 2020a, 2024) and monitor their microseismic activity (Calais, Symithe, Monfret, Delouis, Lomax, Courboulex, Ampuero, Lara, Bletery, Chèze, Peix, Deschamps, de Lépinay, et al., 2022b; Douilly et al., 2023) will contribute to these ends.

Chapter 3

Coulomb stress analysis and slip on secondary faults following the 2021 Haiti earthquake

3.1 Abstract

During and after the M_w7.2 2021 Haiti earthquake, cm-scale shallow slip as far as 15 km from the main rupture was observed at a variety of orientations using high-resolution InSAR phase gradients. The most prominent secondary fault, a 25 km feature, was observed to slip in two sections with different slip directions over the course of the two weeks after the earthquake. Here we use four models of earthquake slip are used to test the hypothesis that Coulomb Failure Stress (dCFS) resolved onto secondary fault surfaces increased where there was observed shallow slip. The models include a static slip inversion of InSAR and GNSS displacement data; a kinematic slip inversion of teleseismic data, far-field GNSS data, and InSAR data; and two fully dynamic rupture models calibrated using InSAR and GNSS data, one where slip occurs on a single fault plane and one where slip occurs on multiple faults. We find high overlap between static dCFS increases and slip on the largest secondary fault for all models. There is particularly strong agreement between the geodetic static slip inversion and the observed slip on the 25 km secondary fault. This model shows large changes in shear stresses ($\sim$1 MPa) coinciding with the sections of observed fault slip and shear stress directions (changing from left-lateral to right-lateral) which

are consistent with observations of sense of slip across the fault. While static dCFS increases were large where secondary faults showed the largest slip, some secondary faults with shallow slip were located in regions with negative static dCFS. Dynamic stress changes calculated using the dynamic rupture models indicate that dynamic stresses likely brought these faults closer to failure and may be responsible for features which occur in static dCFS shadows.

3.2 Introduction

The 2021 M_w 7.2 Haiti earthquake was an enormously destructive combined left-lateral, thrust event which led to more than 2200 deaths. This event occurred within a complex network of faults comprising the Enriquillo Plantain Garden Fault Zone (EPGFZ), which spans the Tiburon Peninsula in southern Haiti and accommodates left lateral transpressive tectonic motion (Figure 3.1). The 2021 event initiated on a north-dipping fault segment which hosted a combination of blind thrust and left-lateral motion with no observed surface rupture before transferring westward to the adjacent steeply-dipping Ravine du Sud (RSF) fault with primarily strike slip motion where surface rupture was observed (Fig 3.1, Calais, Symithe, Monfret, Delouis, Lomax, Courboulex, Ampuero, Lara, Bletery, Chèze, Peix, Deschamps, de Lépinay, et al., 2022b; Z. Li & Wang, 2023; Okuwaki & Fan, 2022a; Wen et al., 2023; Yin, Xu, Haase, Douilly, Sandwell, & Mercier de Lepinay, 2022)

Following the 2021 Haiti earthquake, Interferometric Synthetic Aperture Radar (InSAR) satellite remote sensing observations showed the broad pattern of surface deformation from the combined left lateral and thrust motion in the direction of the Line-of-Sight (LOS) of the observing satellite. InSAR observations also revealed the presence of shallow deformation on several secondary faults as far as 15 km from the main rupture which were not associated with any major seismicity (Fig 3.2 Yin, Xu, Haase, Douilly, Sandwell, & Mercier de Lepinay, 2022). Across the secondary faults, offsets on the order of 2-3 cm in LOS were imaged clearly by JAXA's L-band ALOS-2 satellite in stripmap mode (resolution of 4 x 8 m). Several of these

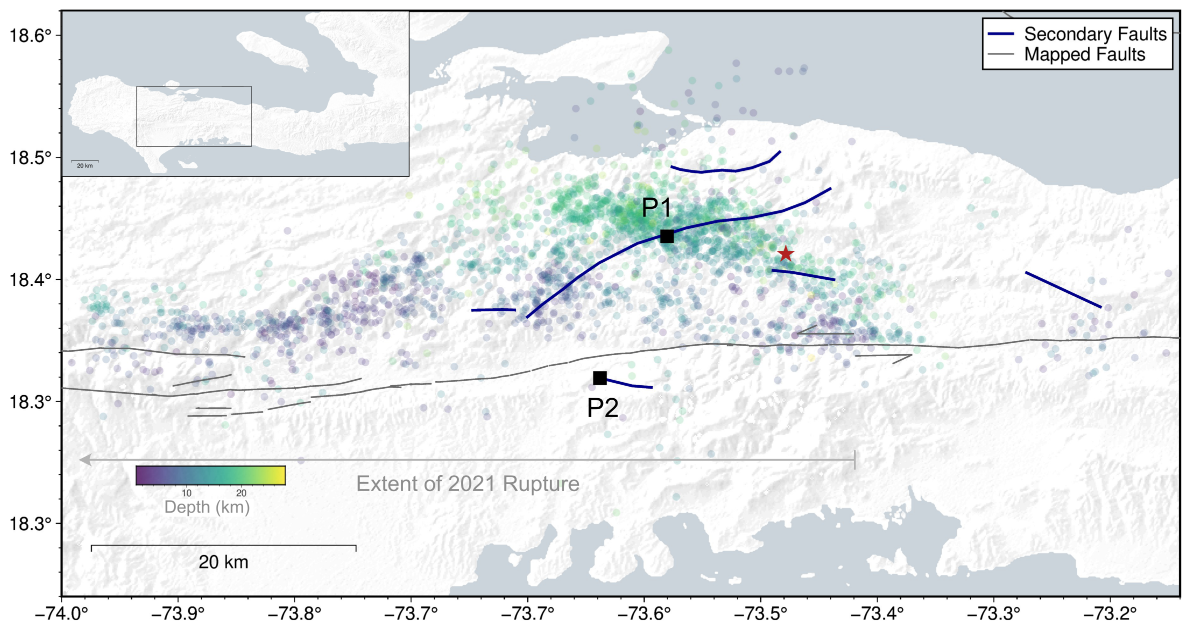

Figure 3.1. Summary of faults active in the 2010 and 2021 ruptures. The approximate extents of the 2021 and 2010 co- and post-seismic slip features are shown with colored lines (Douilly et al., 2015a; Saint Fleur et al., 2020a; Wdowinski & Hong, 2012; Yin, Xu, Haase, Douilly, Sandwell, & Mercier de Lepinay, 2022). The line-of-sight deformation from the descending ALOS-2 track D138 coseismic pair (Dec 10, 2019 - Aug 17, 2021) is overlaid for context, where the region of red indicates uplift. Modified from Yin, Xu, Haase, Douilly, Sandwell, and Mercier de Lepinay (2022)

slip features aligned with pre-existing mapped Holocene faults, (Bien-Aime-Momplaisir et al., 1988b; Mercier de Lépinay et al., 2011). They were active within 4 days of the earthquake (the time to the first InSAR acquisition), and deformation continued for at least two weeks following the earthquake (Yin, Xu, Haase, Douilly, Sandwell, & Mercier de Lepinay, 2022).0.

Observations of deformation on nearby faults following large earthquakes are not unprecedented. There are several analogous examples of slip on secondary faults in response to earthquake ruptures in the well-studied Southern California region, aided the region's ideal conditions for InSAR observations. Following the 1992 Landers earthquake, InSAR observations illuminated deformation on preexisting mapped faults within 50 km of the main rupture within approximately one month of the earthquake using the phase gradient technique (Price & Sandwell, 1998a). Similarly, phase gradient analysis revealed triggered slip on adjacent faults within 4 days and within 15 km of the the 1999 M_w7.1 Hector Mine earthquake (Fialko et al., 2002; Sandwell et al., 2000a). More recently, the InSAR phase gradient technique was used to reveal slip on hundreds of secondary faults within 5-10 days and 20 km of the 2019 Ridgecrest earthquake ruptures (Xu, Sandwell, & Smith-Konter, 2020b; Xu, Sandwell, Ward, et al., 2020a).

3.3 Data

3.3.1 InSAR Observations

Yin, Xu, Haase, Douilly, Sandwell, and Mercier de Lepinay (2022) identified the activation of secondary fault features following the 2021 earthquake. The InSAR phase gradient technique highlights areas of discrete surface offsets directly from the wrapped phase (Price & Sandwell, 1998a; Xu, Sandwell, & Smith-Konter, 2020b). The method calculates the gradient of the complex phase in the azimuth (flight) direction of the observing satellite, applying a square Gaussian filter with a large wavelength (200 m) in order to suppress noise. Fig 3.2 shows the phase gradient of 8 stacked interferometric pairs (collectively covering about one year) from the Japan Aerospace Exploration Agency's (JAXA's) ALOS-2 ascending track A042 and A043 pairs.

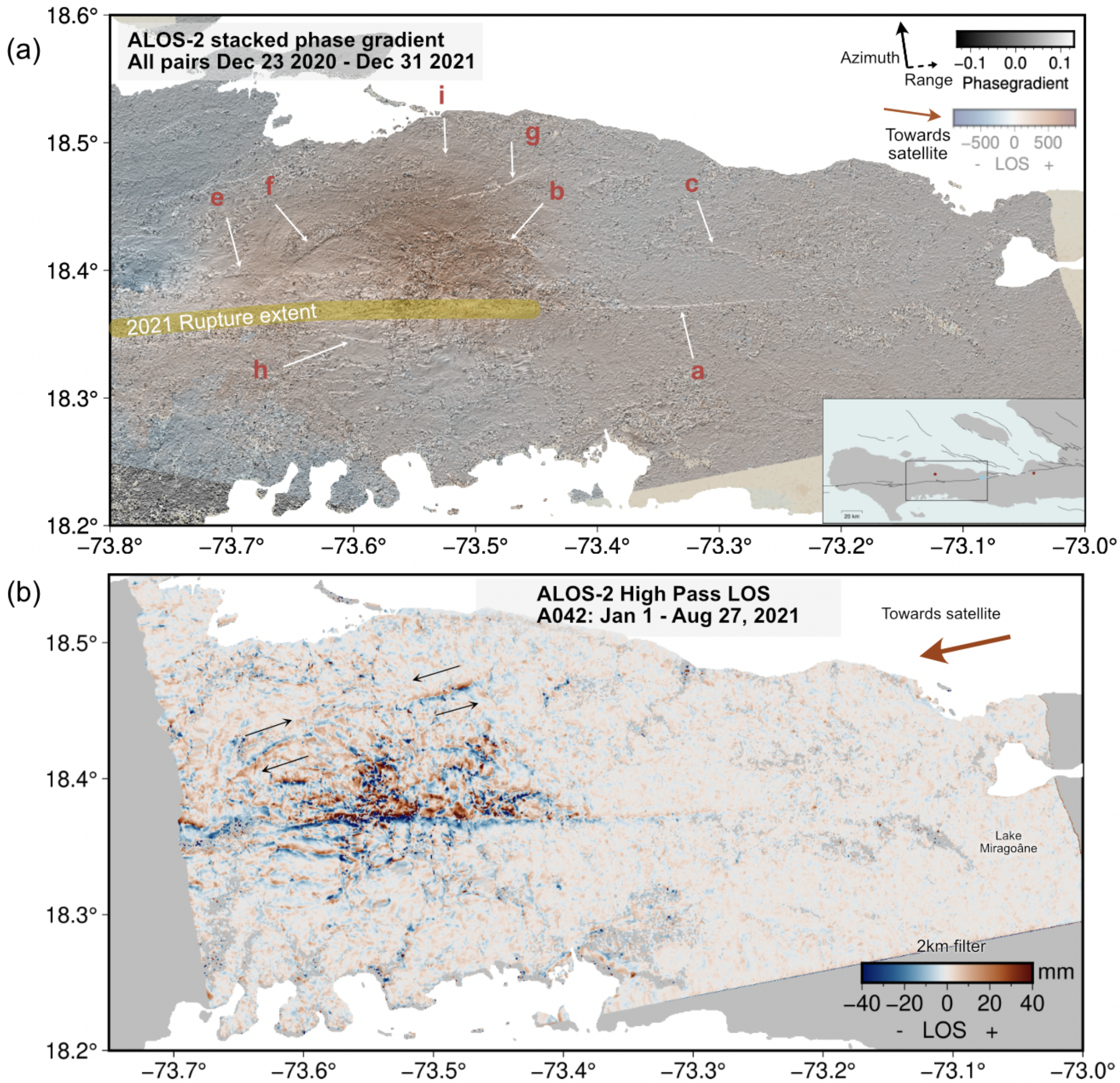

Figure 3.2. Identification of secondary fault features resulting from the Aug 7, 2021 earthquake using InSAR data. (a) Stacked phase gradient in the azimuth direction, including all ascending ALOS-2 pairs between Dec 23, 2020 and Dec 31, 2021, with three pairs from track A042 and five pairs from track A043. The phase gradient is overlain with the LOS plot from ALOS-2 pair D138 for context, with uplift shown in red.; (b) High-pass filtered LOS deformation highlights the sense of motion on identified features. The sense of motion is indicated with black arrows. The noisy area immediately surrounding the main rupture is not easily interpretable and is likely due to the main coseismsic deformation field. (Modified from Yin, Xu, Haase, Douilly, Sandwell, & Mercier de Lepinay, 2022)

Features of interest were identified as features with high positive or negative phase gradient values (Fig. 3.2a). The offset direction cannot be interpreted directly from the sign of the phase gradient. Instead, high-pass filtered LOS plots (with 2 km Gaussian filter) were used to interpret the sense of motion on each of these features (Fig. 3.2b). Because only one look direction was acquired with high enough resolution to clearly resolve slip on the secondary faults (ascending tracks 042 and 043), the description of direction and magnitude of cross-fault offsets remains limited to the LOS direction.

Eight total features were identified in the InSAR data (Fig 3.2a). The most prominent features, f and g, appear to slip in different directions (Fig 3.2b). The high-passed LOS clearly shows the northern side of the feature f moving away from the satellite and the northern side of feature g moving toward the satellite (relative to the southern side, Fig 3.2b). These observations are consistent with left lateral and/or reverse motion on g and right lateral and/or normal motion on f. f and g can be robustly observed in multiple InSAR images over different time spans (Yin, Xu, Haase, Douilly, Sandwell, & Mercier de Lepinay, 2022).

The other seven features are also considered with varying degrees of certainty. Features a,e and h, for example, can be clearly identified in the stacked phase gradient (Fig 3.2) and the component interferograms, while features b, c and i can only be identified in individual interferogram pairs (Yin, Xu, Haase, Douilly, Sandwell, & Mercier de Lepinay, 2022).

3.3.2 Source Models

We use four source descriptions from three studies to calculate changes in stress on the secondary fault surfaces to test the hypothesis that Coulomb Failure Stress increased where shallow slip occurred. While the models capture similar features, they have significant differences in fault geometry that could affect dCFS distribution.

Goldberg et al. (2022) (herein Go22) used teleseismic and strong ground motion seismic data, continuous 1Hz GNSS far-field displacements and Sentinel-1 C-band InSAR observations, in a kinematic source inversion. The rupture was described using a single fault plane, striking

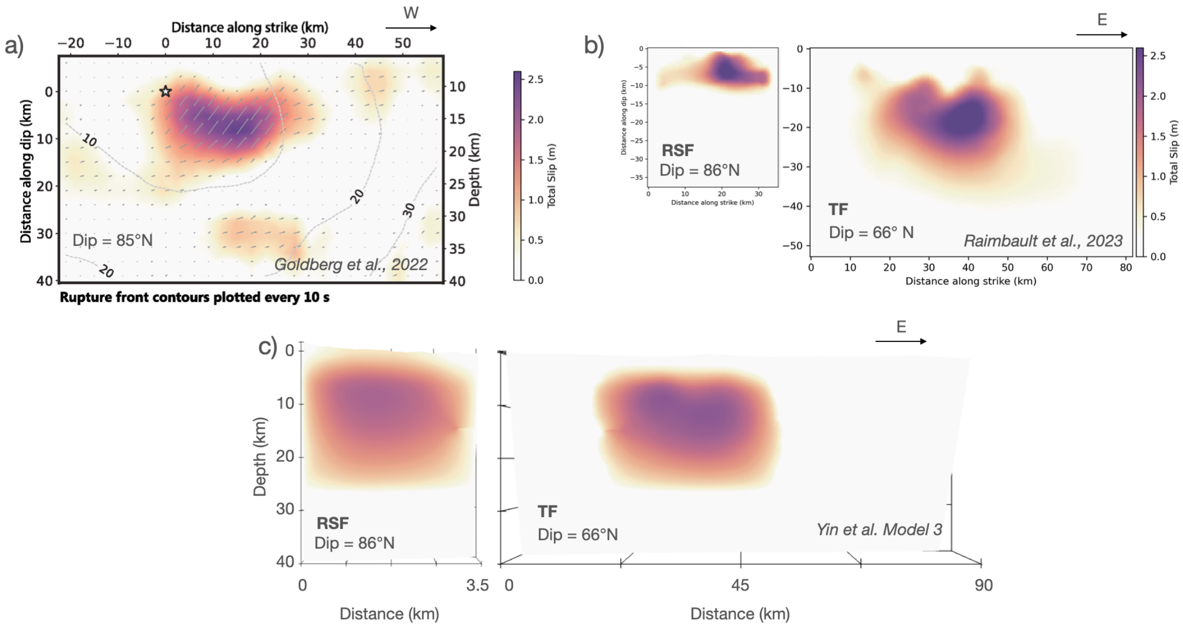

Figure 3.3. Summary of slip models from: a) Go22, seismogeodetic kinematic slip inversion on a single north-dipping plane (Goldberg et al., 2022) ; b) Ra23, geodetic static slip inversion (Raimbault et al., 2023); c) YinB, 3D dynamic rupture model (Yin et al., 2025). Slip is shown using the same color scale for all models.

266°, dipping 85°N, and subdivided into 3km x 3km subfaults. They found one main oblong patch of slip on the fault, with a combination of left lateral and thrust motion peaking at ∼2.7 meters of slip down-dip and west of the hypocenter (Fig 3.3). They found a smaller, shallow patch of primarily left lateral slip to the west of the main patch, on the order of ∼1 meter Their model described unilateral westward rupture with three pulses of moment release at 8, 18 and, 22 sec after the origin time. This model was developed as a rapid model as part of the USGS response and is the simplest of the models considered (Goldberg et al., 2022).

Raimbault et al. (2023) (herein Ra23) used a combination of static GNSS offsets and ALOS-2 L-band InSAR deformation data to invert for a static slip distribution. They tested a range of fault dips for their proposed two-fault rupture. The find minimal misfit for a geometry with: (1) a thrust fault running subparallel to the EPGF, herein called the Thrust Fault (TF) which dips north 66 ± 4°; and (2) the Ravine du Sud Fault (RSF) which is a mapped near-vertical fault, dipping north 86 ± 2° (Fig 3.3). The resulting static slip distribution combined reverse and strike-slip motion on the north-dipping TF between 10 and 20 km depth with a maximum slip of 2.9 m. On the RSF they found primarily left-lateral strike slip motion shallower than 7 km (not extending below the intersection with the TF), with maximum slip of 2.6 m.

Finally, Yin et al. (2025) developed a suite of 3-D dynamic rupture models using the open source software SeisSol (https://github.com/SeisSol/) which simulates coupled physics-based rupture propagation and dynamic 3-D wave propagation (Gabriel et al., 2023; Taufiqurrahman et al., 2023; Ulrich et al., 2019). The two-fault geometry followed that of Raimbault et al. (2023) and was meshed with an on-fault resolution of $\sim$200 m, increasing with distance from the fault. They developed a suite of dynamic rupture simulations which were used to understand the key factors required to reproduce distinct patches of strike slip and dip slip motion rather than a single throughgoing strike slip fault. We consider two simulations from the Yin et al. (2025) suite of models: One simulation (Model 4 in the original text, herein YinA) imposed a constant regional stress tensor and orientation across the RSF and TF, resulting in no rupture transfer to and therefore no slip on the RSF. In this model, the TF ruptured in a combination of strike slip and dip slip motion with maximum slip of $\sim$2.3 m (Fig 3.3). This rupture fit most observations and represented a single fault dynamic rupture model.

An additional Yin et al. (2025) simulation (Model 5 in the original text, herein YinB), introduced changes to the regional stress tensor and its orientation between the RSF and TF which promoted rupture propagation onto the RSF and produced slip on both faults. Similarly to the previous model, the TF ruptured in a combination of strike slip and dip slip motion with maximum slip of $\sim$2.2 m. On the RSF, left lateral strike slip motion dominated with maximum slip of $\sim$1.9 m. YinB, while more complex, better reproduced the major observations of the event including the characteristic spatial separation of strike-slip and dip-slip motion, the extent of observed rupture, the InSAR surface deformation field, GNSS offsets, total seismic moment, and source time function. When compared to YinA, YinB better reproduced the InSAR observations in the Western part of the rupture and the observed multi-peak source time function due to slip transfer to the RSF.

Both Go22 and YinA can be considered single-fault models with one primary patch of slip centered at ~73.6°W. Ro23 and YinB both capture distinct patches of strike slip and dip slip motion on the TF and RSF, respectively which reproduce the observed InSAR surface deformation pattern. The Ra23 slip distribution is more spatially complex than YinB (Fig 3.3), and slip on the RSF is more shallow.

3.4 Methods

Coulomb Failure Stress (CFS) provides one possible explanation for deformation on secondary faults. The CFS hypothesis asserts that slip on so called "source faults" produces changes in CFS (dCFS) on the surrounding faults, "receiver faults", and that failure on receiver faults is promoted by increases in dCFS (King and Stein,1994). dCFS is calculated using the definition:

$$dCFS = \Delta\tau_s + \mu'\Delta\sigma_n \tag{3.1}$$

where $\Delta\tau_s$ is the change in shear stress in a chosen rake direction (often assumed to be the direction of coseismic slip on the source fault), μ' is the effective coefficient of friction, and $\Delta\sigma_n$ is the change in effective normal stress (where negative normal stress implies compression) (Harris, 1998; King et al., 1994). The receiver fault can be specified to have a given rake to assess whether slip in that direction is encouraged or discouraged.

We consider both static and dynamic dCFS, where dynamic dCFS is the time dependent evolution of dCFS and static dCFS reflects the final stress state due to the slip distribution on the source fault(s). Static dCFS is a permanent stress change which does not consider the time-dependent rupture process. Static dCFS has correlates with aftershock production for days to weeks after a mainshock (Kilb et al., 2002; King et al., 1994) and has been proposed to explain triggering and advance or delay of large earthquakes (Stein et al., 1997; Yun et al., 2024). Static dCFS has been used to describe the increase in hazard on fault systems surrounding major earthquakes (e.g. Ali et al., 2008a; S. J. Symithe et al., 2013a; Toda & Stein, 2020) as well as to explain the general locations of aftershock production (e.g. Hardebeck & Harris, 2022; Kilb et al., 2002). Static dCFS has also been linked to the activation of secondary faults which fail with frictional slip (Fialko et al., 2002; Xu, Sandwell, Ward, et al., 2020a). The time dependent, dynamic dCFS is primarily induced by the passage of seismic waves (Kilb et al., 2002). While dynamic dCFS is transient, it can can change conditions in the crust (e.g. by increasing permeability, Elkhoury et al., 2006) and trigger aftershocks for several days after seismic waves have dissipated (Brodsky, 2006; Kilb, 2003; Pollitz et al., 2012).

Here we use several different models of the 2021 Haiti rupture to calculate static and dynamic dCFS produced by the event and explore the respective roles of static and dynamic stresses in secondary fault activation. We first calculate the components of static dCFS resolved on the secondary fault surfaces to determine if secondary faults which slip experience in increase in static dCFS due to the rupture. We also calculate the direction of maximum shear stress on the faults to see if the direction of shear stress is consistent with the direction of observed slip on features f and g. We then calculate static dCFS field across the southern peninsula assuming a constant receiver orientation and rake. This is used to confirm whether secondary faults which are observed to slip experience occur in regions of static dCFS increases. Finally, we calculate the time dependent dCFS for the dynamic rupture models to assess the role of dynamic stresses in secondary fault activation.

For the static (Ra23) and kinematic (Go22) slip models, we use the Matlab-based Coulomb 3.3 software to carry out static stress change calculations (Toda, Shinji et al., 2011). In this calculation, slip is partitioned onto rectangular subfaults and each is approximated as a point source with a slip magnitude and direction. Strains and stresses caused by these dislocations are calculated and summed at each point in an elastic half-space with uniform isotropic elastic properties following Okada (1992). We treat the stresses due to the dislocations as the stress change due to the slip, without making any assumptions about the absolute stress state prior to the earthquake. We assume a uniform shear modulus (G) of 33 GPa. The shear stress change and normal stress change vectors are then resolved on each receiver subfault and dCFS is calculated using equation (1), specifying an effective coefficient of friction, μ'. For more direct comparison with the dynamic rupture model, we use the static coefficient of friction, μ_s, which was constrained by Yin et al. (2025), $\mu' = 0.52$. We generate the secondary 3-D fault surfaces using the fault traces of Yin, Xu, Haase, Douilly, Sandwell, and Mercier de Lepinay (2022) and assuming a vertical dip, discretizing each fault into 1km x 1km subfaults.

The dynamic rupture models (YinA and YinB) use a layered elastic halfspace with layered shear modulus from a seismic velocity inversion (Douilly et al., 2023). The stress tensor is calculated at each point on each of the fault surfaces at each simulated time step, both from the evolution of slip on the fault and from passing seismic waves (Yin et al. 2025). For the dynamic rupture model there is an absolute initial stress state resolved on the fault surfaced prior to the earthquake, so we calculate the change in stress at each time step by taking the current minus initial stress. The stress tensor is resolved as shear and normal stress vectors on each subfault surface at every time step. Shear and normal stresses are then used along with the calibrated static coefficient of friction for YinB ($\mu' = 0.52$) to calculate dCFS on the fault surfaces through time using equation 3.1. The dynamic dCFS is considered to be the time dependent dCFS resolved on the faults surfaces. The static dCFS is considered to be the final dCFS on the fault surfaces after all dynamic waves have dissipated.

3.5 Results

3.5.1 Static dCFS resolved on fault surfaces

The static dCFS from the Ra23 and Go22 models are calculated using the Coulomb3 software and resolved directly onto the 3-D fault surface of f and g, where each subfault acts as a receiver fault. In this calculation we resolve the maximum dCFS on each subfault by calculating dCFS in the direction of shear stress change (i.e. $\Delta\tau_s = \Delta\tau$ in Eq 3.1). Positive dCFS promotes failure in the direction of the shear stress change. The resulting static dCFS and its

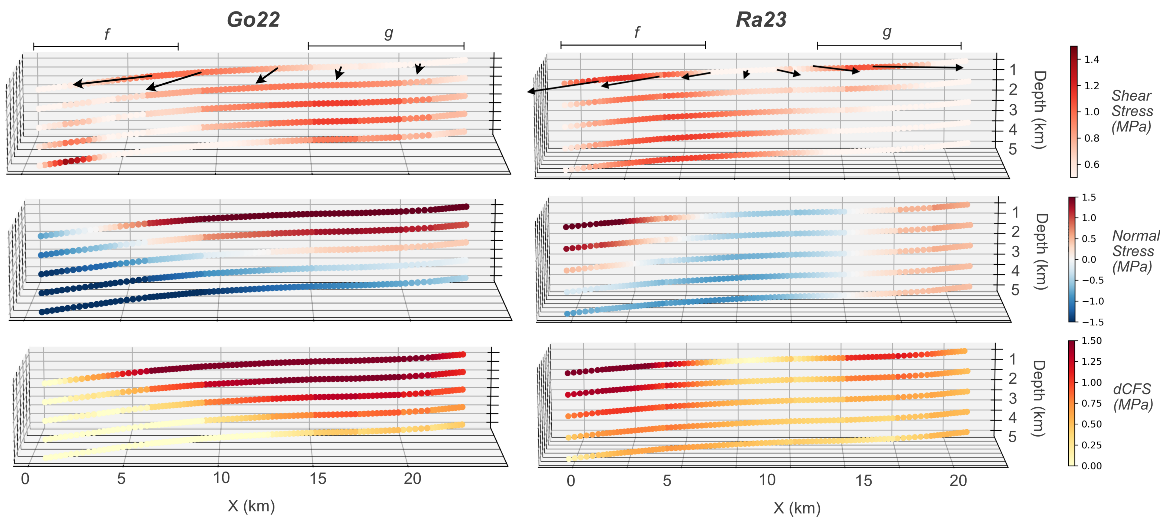

Figure 3.4. Components of static dCFS calculated on the surface of fault f-g, with the Go22 model used as the source on the left and the Ra23 model used as the source on the right. Only the shallowest 5km of the fault is shown. a) Shear stress, τ resolved on $f-g$. Arrows represent the shear stress vector across the fault approximately scaled by shear stress magnitude and oriented by shear stress direction, where left indicates left-lateral stresses and right indicates right-lateral stresses. b) Direction of shear stress explicitly shown where dark colors represent right-lateral, light colors represent left-lateral, blue colors represent normal, and red colors indicate reverse. c) Normal stress, $\Delta\sigma_n$ where red colors indicate tension and blue colors indicate compression. d) dCFS computed using $dCFS = \Delta\tau_s + \mu'\Delta\sigma_n$ (Eq 3.1), where $\mu' = 0.52$.

components (shear stress change and normal stress change) for Ra23 and Go22 are shown in Fig 3.4. Increases in shear stress change and more positive normal stress change (less compression) both contribute to positive dCFS and encourage slip on receiver faults in the shear stress change direction. If the secondary faults are responding to positive dCFS, then the shear stress change direction should agree with InSAR observations of sense of slip on secondary faults.

Both Go22 (Fig 3.4, left) and Ra23 (Fig 3.4, right) models show an increase in dCFS for f and g, suggesting that in both models, shallow parts of the secondary faults were brought closer to failure by coseismic slip.

For the Go22 model, the largest shear stress changes ($\sim$0.8 MPa) only partially align with feature f and don't overlap with feature g. Comparing the shear and normal stress change components shows that dCFS increases on the shallow fault are driven primarily by positive changes in normal stress (i.e. less compression). The resulting Go22 dCFS values are greater than $\sim$1MPa over almost the entire upper 1km on the fault surface, except the western part of f. The direction of shear stress change in the upper 1km starts as pure right-lateral slip at the western end of the feature and smoothly changes to a combination of right-lateral and normal slip at the eastern end, which is not consistent with InSAR observations of sense of slip (Fig 3.2).

In the Ra23 model, the largest shear stress changes in the upper km (over 1 MPa) align well with the extent of both f and g, with low shear stress changes in between. Similarly, the normal stress change distribution has two large, positive maxima which align well with f and g (1MPa on feature f and $\sim$0.5 MPa on feature g), with negative values (compression) in between. Shear and normal stress changes both contribute to a large ($\sim$1.5 MPa) peak in dCFS along feature f and a smaller peak ($\sim$1 MPa) aligned with feature g. The Ra23 model has a large variation in direction of shear stress change across the f and g. From the west to the east, shear stress changes gradually change from pure right-lateral to left-lateral, which agrees well with InSAR observations of sense of slip across the both secondary faults. The Ra23 model both promotes slip on $f-g$ in the observed locations of slip as well as the observed directions of slip. It inhibits slip in between the features, which matches observations.

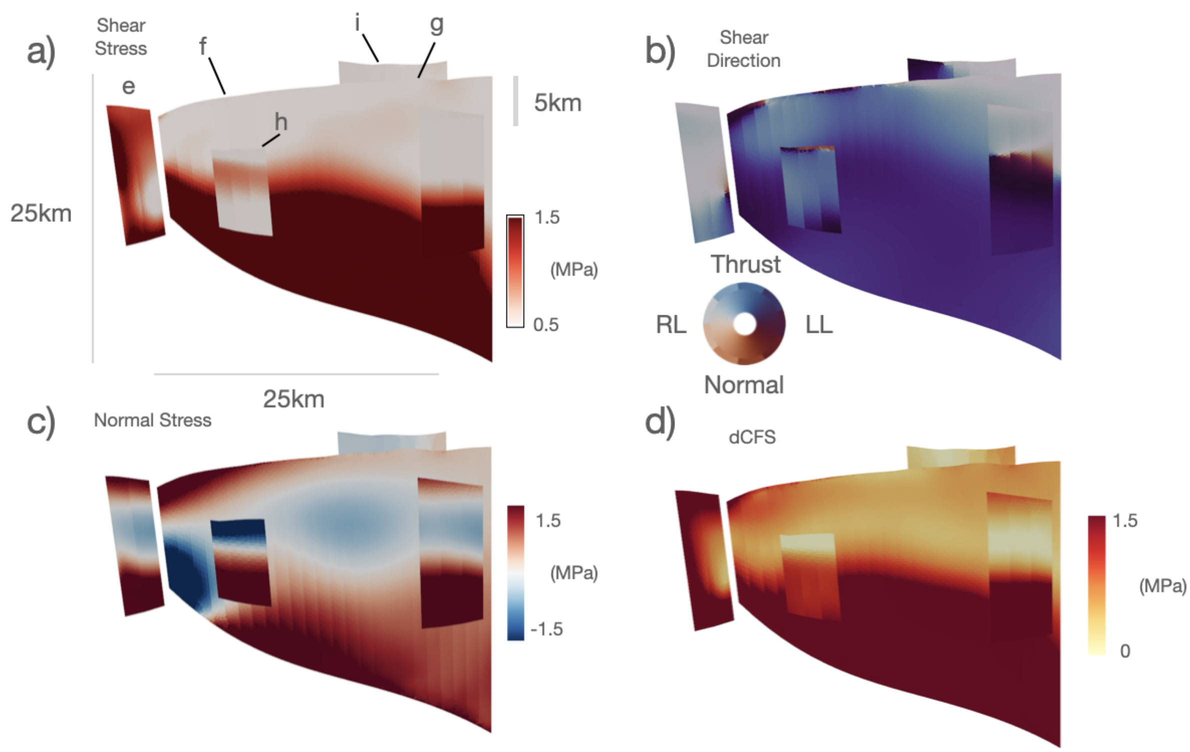

Figure 3.5. Components of static dCFS calculated on the surface of fault f-g, with the YinB dynamic rupture model used as the source. a) Magnitude of shear stress change, τ resolved on $f-g$. b) Direction of shear stress change where dark colors represent right-lateral, light colors represent left-lateral, blue colors represent normal, and red colors indicate reverse. c) Normal stress change, σ_n where red colors indicate tension and blue colors indicate compression. d) dCFS computed using $dCFS = \Delta\tau_s + \mu'\Delta\sigma_n$ (Eq 3.1), where $\mu' = 0.52$.

The dynamic rupture models allow for a similar, though not exactly comparable, calculation of the dCFS and its components (normal stress change and shear stress change) resolved on the fault surfaces at every simulated time step. We calculate the static dCFS by subtracting the initial stress conditions from the final stress conditions on the fault surfaces, after all seismic waves have left the model domain (60 seconds of simulation). We use a coefficient of friction of μ'=0.52 in the dCFS calculation which is the static coefficient of friction set in the dynamic rupture models (Yin et al., 2025). One major difference between this calculation and the previous Coulomb3 calculation is that the dynamic rupture model uses a medium with vertically stratified values of shear modulus (Douilly et al., 2023) to determine the final stress state. We expect that lower shear modulus in the shallow crust may likely result in lower shear and normal stress changes near the surface.

The static stress change components resulting from dynamic rupture YinB, where rupture transfers to the RSF, are shown in Fig 3.5 resolved on all secondary fault surfaces, where the longest feature is $f-g$. Very low shear stress changes (below 0.2 MPa) are found in the upper 5km of feature $f-g$ (Fig 3.5a). Normal stress changes (Fig 3.5c), however, show high positive values (greater than 1.5 Mpa) over the extent of feature f and increasing to the west. The resulting dCFS distribution (Fig 3.5d) is driven primarily by positive normal stress changes. The largest dCFS values are on the far west end of feature f, with a maximum of $\sim$1.5 MPa. The direction of shear, similar to the Ra23 model, shows variation from right-lateral (west side) to left-lateral (east side), which aligns with InSAR observations of the sense of motion on $f-g$, despite small shear stress amplitudes.

We calculate the static dCFS on the other secondary fault segments surrounding the main rupture for all rupture models. For Ra23 and Go22, 5 of the 6 remaining secondary fault features show a shallow dCFS of 0.5 MPa or higher. For YinB, 3 of the 6 features show a shallow dCFS of 0.5 MPa or higher. This difference in the YinB model may be due to the difference in shallow shear modulus (Fig S1).

We also consider the YinA dynamic rupture simulation which does not result in rupture

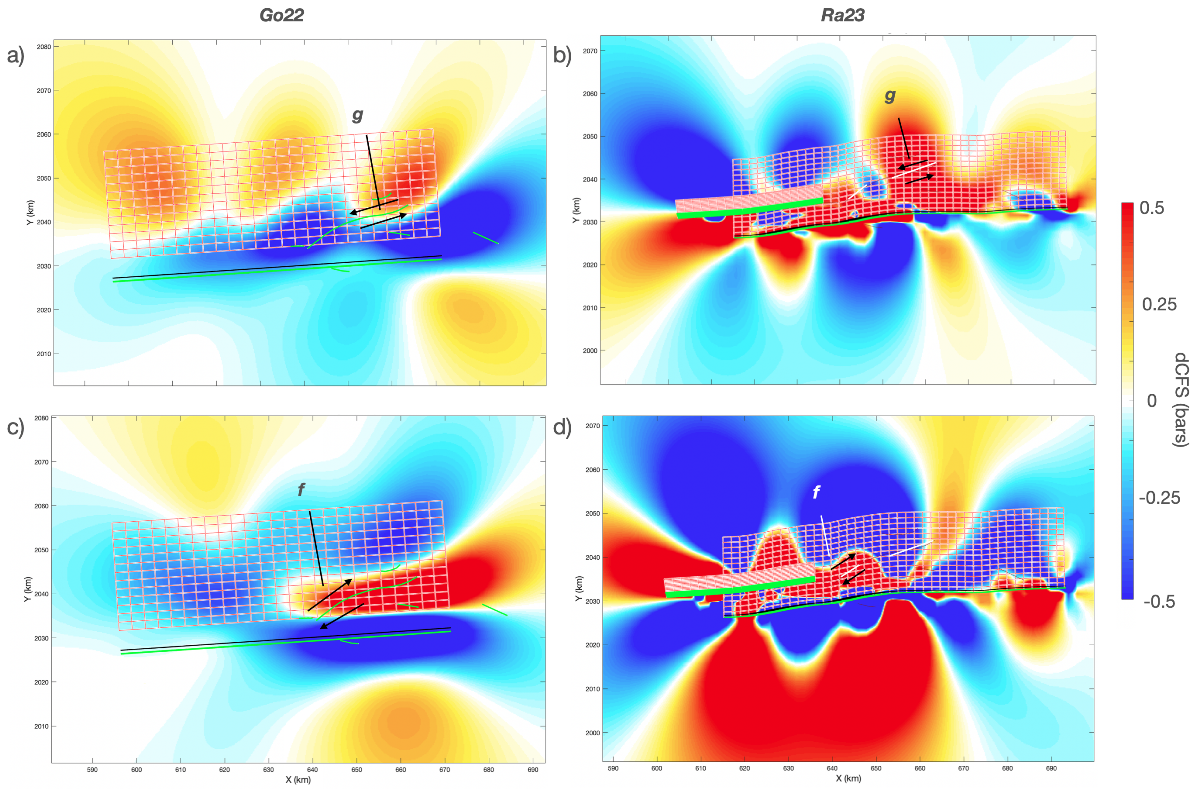

Figure 3.6. dCFS calculated using the Go22 slip model (left) and the Raimbault slip model (right) both shown at 1 km depth. The top panels assume a receiver fault oriented at 52° with pure left lateral (0°) rake which approximates the orientation and assumed rake on feature g. The bottom panels assume a receiver fault oriented at 49° with pure right lateral (90°) rake which approximates the orientation and assumed rake on feature f.

transfer to the RSF and a version of the Ra23 model which excludes slip on the RSF to test the response of the static dCFS distribution to the absence of slip on the RSF. For both Ra23 with vs. without slip on the RSF and YinA vs. YinB, the static dCFS field remains largely the same, indicating that slip on the RSF does not have a large impact on the dCFS field in the region of the secondary faults. However, removing slip on the RSF slightly decreases shallow dCFS ($\leq 0.5MPa$) on the westernmost end of $f-g$ in both cases (Fig S2). Thus, slip on $f-g$ is further encouraged in the rupture models that include slip on the RSF.

3.5.2 Static dCFS with specified rake

We calculate the static dCFS field at all points to test the spatial correspondence of features f and g with positive dCFS. In this calculation, the orientation of the receiver fault and rake are assumed to be constant throughout the volume. Based on the InSAR observations of sense of slip (Fig 3.2b), we assume that motion on features f and g is purely strike slip, with motion on f purely right lateral and feature g purely left lateral. Fig 3.6 shows the static dCFS field in map view resulting from the Raimbault et al. (2023) and Goldberg et al. (2022) models at 1 km depth. The upper panel assumes a receiver fault oriented at 52° with pure left lateral rake (0°) which approximates the orientation and assumed rake on feature g. The bottom panels assume a receiver fault oriented at 49° with pure right lateral rake (180°) which approximates the orientation and assumed rake on feature f. The Go22 slip model with fault orientation aligned with feature g (Fig 3.6a) shows feature g in a lobe of small but positive dCFS, (0- 0.2 MPa) with feature f in a negative lobe of dCFS. For the fault orientation aligned with feature f (Fig 3.6c), feature f is predominantly located a positive dCFS lobe up to 0.5 MPa. This corresponds to left lateral motion being encouraged on a fault which aligns with feature g and right lateral motion being encouraged on a fault which aligns with feature f. For the Ra23 slip model with fault orientation aligned with feature g (Fig 3.6b), feature g is centered in a lobe of positive dCFS greater than 0.5 MPa. For fault orientation aligned with feature f (Fig 3.6d), feature f is also centered in a lobe of positive dCFS greater 0.5 MPa. The Ra23 model has a more spatially complex slip distribution than the Go22 model and has a correspondingly more complex dCFS distribution when we assume a constant fault orientation and rake (Fig 3.6). Both models are consistent with observations of slip on both f and g, supporting the interpretation that static dCFS is encouraging the observed slip on f and g.

The comparison between the simpler Go22 model and the more complex Ra23 model show that the source complexity (both in rupture geometry and slip distribution) is reflected in the complexity of the shallow dCFS field. Despite both models having good agreement with broad observations of the coseismic rupture (Goldberg et al., 2022; Raimbault et al., 2023), the dCFS fields produced by each slip distribution were quite distinct. This is illustrated in Fig 3.6 which shows a simpler dCFS pattern in map view for the Go22 model versus the Ra23 model which has much shorter wavelength features, especially close to the fault, and distinct areas of positive and negative dCFS. Despite its complexity, the Ra23 model's dCFS distribution and shear stress direction are still consistent with the observed secondary fault activations.

3.5.3 Dynamic dCFS

Dynamic stress changes can be larger than static stress changes and can promote failure on favorably oriented faults. The dynamic rupture models (YinA and YinB) provide an opportunity to examine the relative magnitude of the static vs. dynamic stress changes. In particular, we can test whether secondary faults which slipped despite being located in static dCFS shadows (regions of negative static dCFS) had large dynamic stress changes which may have contributed to their failure. Simulated dCFS during dynamic rupture of YinB is shown in Fig 3.7 at two points at $\sim$1 km depth, each on different secondary fault features. The point shown in fig 3.7a is located below the surface trace of feature $f-g$ (within 10 km of the main fault rupture), and as shown in figure 6 was located in a region of positive static dCFS. The point shown in fig3.7b is located below the surface trace of h (within 3 km of the main fault rupture). This point is located in a region of negative static dCFS. Seismic waves are seen passing the through $f-g$ (Fig 3.7a) as large dCFS fluctuations beginning at 5 seconds after the start of the rupture, with peak dCFS during rupture of $\sim$0.8 MPa. The static dCFS is the offset between the initial dCFS and the final dCFS, $\sim$0.5 MPa. This illustrates that, on feature $f-g$, static dCFS encourages slip on the fault, while dynamic stresses further encourage slip. For feature h (Fig 3.7b), the peak dCFS reaches $\sim$0.3 MPa after 6 seconds of rupture, but the static dCFS is negative ($\sim$-0.4 MPa) due to permanent decreases in normal stress (increased compression). In this case, static stress changes discouraged slip on feature h, while dynamic stress changes encouraged slip. Since slip was observed on this fault, we conclude that dynamic stresses may have been primarily responsible

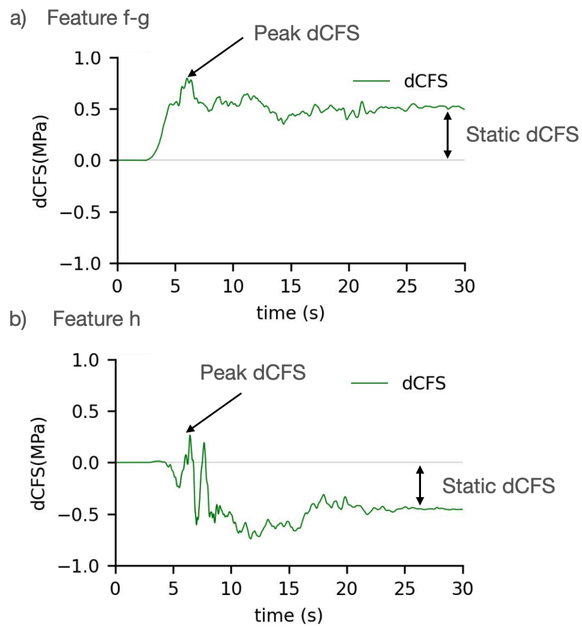

Figure 3.7. Dynamic dCFS shown at two points in the fault system. a) Point P1 (Fig 3.1) on feature $f-g$, within 10 km of the main fault rupture, where the largest value of dCFS is at ∼6 sec and the final dCFS is the positive offset between initial and final CFS. b) Point P2 (Fig 3.1) on feature h, within 3 km of the main fault rupture, where the largest value of dCFS is at ∼6 sec and the final dCFS is the negative offset between initial and final CFS.

for slip on feature h.

Fig 3.8 shows peak dCFS for the YinB model, illustrating the pattern of peak dCFS over the entire fault system. Dark colors indicate where dynamic stresses created high peak dCFS. There is clear asymmetry, with higher peak dCFS values concentrating west of the rupture, with minimal dynamic stresses impacting the fault system east of the rupture, including the offshore thrust fault system to the northeast. This is likely due to directivity effects from the unilateral westward rupture captured in the dynamic model. There is also a rapid drop-off in peak dCFS with distance from the fault, apparent on features $f-g$, and i to the north.

3.6 Discussion

All four rupture models showed a general increase in static dCFS at shallow depths in the region where shallow slip was observed on $f-g$ The Ra23 model showed particularly strong

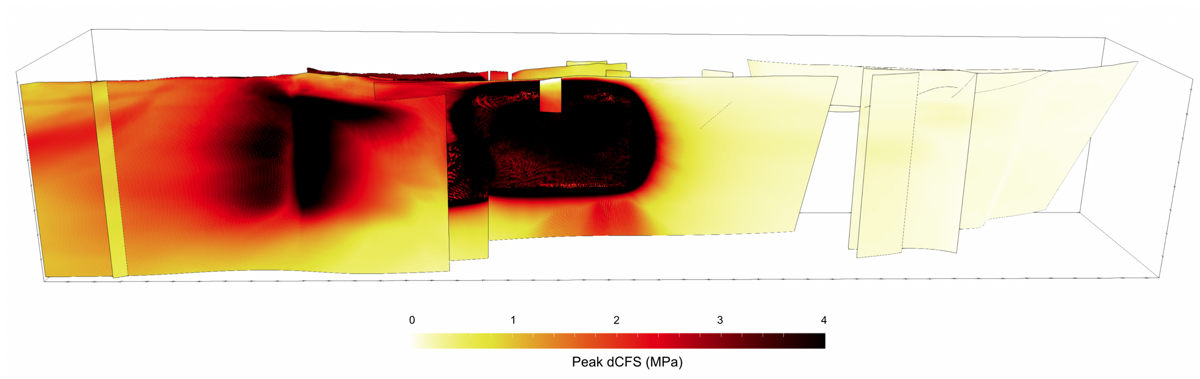

Figure 3.8. Peak dynamic dCFS for Model YinB, shown for all meshed fault surfaces.

agreement between static dCFS distribution, shear stress direction, and secondary fault failure.

The Go22 model is relatively simple, both in geometry and slip distribution which reflects its development as a rapid response product (Goldberg et al., 2022). Go22 utilized the rapidly available C-band Sentinel-1 InSAR data in their joint inversion of geodetic and teleseismic data for kinematic slip. The shorter wavelength C-band satellite data was later shown to underestimate the large near-fault deformation in response to shallow slip of this event, due to the dense vegetation in the region (Yin, Xu, Haase, Douilly, Sandwell, & Mercier de Lepinay, 2022). These factors may have contributed to underestimates of shallow slip in the Go22 model. For example, Go22 does not assign slip shallower than 5 km, while slip on the RSF in Ra23 assigns slip of over 2 m at shallower than 5 km depth. This may have contributed to the weaker agreement of stresses on secondary faults of Go22 relative to the Ra23 model. It also suggests that shallow slip likely only affects stress closer to the fault than $f-g$.

In future work it would be useful to test the sensitivity to variations in the effective coefficient of friction. We expect changes in μ' to have the biggest impact on models whose final dCFS distributions had strong influence from normal stress.

The Ra23 and Go22 slip distributions are both more spatially complex than the YinA or YinB slip distributions (Fig 3.3). This is a typical difference between slip inversions which solve directly for the slip distribution which best explains the observations, as opposed to dynamic rupture models which are aimed at capturing the dynamics of the event. This difference is reflected in the strong agreement between location of dCFS increase for the Ra23 model and the location of slip on $f-g$. The layered elastic properties used in the dynamic rupture models had lower rigidity in the shallow crust than the elastic halfspace used in the Coulomb3 calculations. This may have also contributed to the smaller shear and normal stress changes relative to the Go22 and Ra23.

Two modes of slip have been proposed to explain deformation on secondary faults in cases where slip is observed in different directions (Fialko et al., 2002; Xu, Sandwell, Ward, et al., 2020a): 1) Frictional slip, where the fault strength is overcome by the shear stress on the fault. This mode of failure is promoted by increases in shear stress or decreases in normal stress and tends to result in very sharp surface deformation on the fault. Therefore, increases in Coulomb Failure Stress (CFS) from the main rupture can be used to quantify whether a fault was brought closer to or further from failure by the main rupture; 2) Compliant deformation, where elastic failure of a weak ”compliant zone” is a passive response to surrounding stress changes. These displacements depend on the shear stress changes on the receiver fault resulting from the stress change of the main earthquake, effective width of the receiver fault zone, and the rigidity contrast with the surrounding rocks but are independent of the absolute background stress (Fialko et al., 2002; Xu, Sandwell, Ward, et al., 2020a). This study is not aimed at distinguishing between these two modes of slip. Further examination of the cross-fault deformation pattern of these secondary features would be needed to determine the mode of failure.

3D dynamic rupture models were used to model dynamic and static stresses on the fault system surrounding the main rupture. As expected, there was a rapid drop-off of peak dCFS with distance from the fault (Hardebeck & Harris, 2022) and strong directivity effects which caused asymmetric peak dCFS west of the rupture. While peak dCFS values on the main fault rupture can be an order of magnitude larger than static dCFS values (i.e. Jia et al., 2023), the lateral distance from the rupture appears to significantly attenuate the magnitude of dynamic stresses within a few kilometers of the fault for this event. Simulated dCFS through time on secondary faults (Fig 3.7) shows that, while the peak dCFS occurs during the passage of seismic waves, the static dCFS also encourages rupture on $f-g$. However, there are also cases, like feature h, which occurred in static stress shadows but modeled dynamic stresses seem to encourage slip and may be responsible for the triggered slip. This triggering mechanisms where some features appear to respond to static dCFS increases while others, within stress shadows, appear to respond to dynamic stresses, is similar to a relationship proposed for aftershock production. Hardebeck and Harris (2022) studied the relative impact of static vs. dynamic dCFS on aftershock production and found that for three major California earthquakes, $\sim 34\%$ of of aftershocks were due to dynamic triggering and $\sim 66\%$ were due to static triggering. Yun et al. (2024) similarly found that static dCFS is more effective in modulating the timing of subsequent triggered earthquakes than dynamic dCFS. We hypothesize that a similar relationship may be true for the triggering of shallow slip on secondary faults. This would explain why some faults (like fault h), which did not have static increases in dCFS according to any of the source models, may still have slipped encouraged by dynamic effects. Future work could include an in-depth study of the aftershocks and their focal mechanisms, following the methods of Hardebeck and Harris (2022). This could determine if, in the case of the 2021 Haiti earthquake, aftershocks within stress shadows were dynamically triggered and aftershocks in regions of positive static dCFS were statically triggered as proposed. However, for such an analysis, a larger catalog of aftershocks would be needed than currently exists for the 2021 event.

3.7 Conclusions

Four rupture models were used to calculate dCFS for the 2021 Haiti earthquake and assess whether features which slipped shallowly during and after the earthquake occurred in regions of positive dCFS. All four rupture models considered showed general agreement between static dCFS in the shallow portion of feature $f-g$ and the observed activation of this feature, suggesting that static dCFS may have contributed to slip on secondary faults. However, more study is needed to better understand the mechanism for slip.

dCFS calculated using the dynamic rupture model, YinB, provides insights into the relative influence of dynamic and static dCFS in the activation of secondary fault features. In the case of fault $f - g$, static dCFS increased encouraging slip, while peak dCFS during the passage of seismic waves, further encourage slip on the fault. In the case of feature h, static dCFS decreased, making it less likely to slip, but the positive dCFS during the rupture may have been sufficient to trigger slip on the feature nonetheless. We find that secondary fault h was likely dynamically triggered, while secondary faults f and g were likely statically triggered.

The spatial distribution of peak dCFS across the fault system in Fig 3.8 shows that peak dCFS is highly impacted by the unilateral western rupture of the earthquake. The ability to capture the directivity effects and resulting dynamic stresses using dynamic rupture modeling could be a useful tool in improving ground motion estimates in the future.

This work highlights that secondary faults can actively participate in the stress response to major earthquakes. Triggered slip on secondary faults also highlights faults which are active and may pose additional sources of hazard, not known prior to the earthquake. This is important for improving ongoing hazard estimates into the future.

Bibliography

Aagaard, B. T., Knepley, M. G., & Williams, C. A. (2013, August). *A Domain Decomposition Approach to Implementing Fault Slip in Finite-Element Models of Quasi-static and Dynamic Crustal Deformation* (tech. rep.). https://doi.org/10.1002/jgrb.50217 arXiv:1308.5846 [physics].

Aiken, C., Chao, K., Gonzalez-Huizar, H., Douilly, R., Peng, Z., Deschamps, A., Calais, E., & Haase, J. S. (2016). Exploration of remote triggering: A survey of multiple fault structures in Haiti. *Earth and Planetary Science Letters*, *455*, 14–24. https://doi.org/10.1016/j.epsl.2016.09.023

Aki, K., & Richards, P. G. (1980). *Quantitative seismology: Theory and methods*. W. H. Freeman.

Ali, S. T., Freed, A. M., Calais, E., Manaker, D. M., & McCann, W. R. (2008a). Coulomb stress evolution in Northeastern Caribbean over the past 250 years due to coseismic, postseismic and interseismic deformation. *Geophysical Journal International*, *174*(3), 904–918. https://doi.org/10.1111/j.1365-246X.2008.03634.x

Ali, S. T., Freed, A. M., Calais, E., Manaker, D. M., & McCann, W. R. (2008b). Coulomb stress evolution in Northeastern Caribbean over the past 250 years due to coseismic, postseismic and interseismic deformation. *Geophysical Journal International*, *174*(3), 904–918. https://doi.org/10.1111/j.1365-246X.2008.03634.x

Andrews, D. J. (1976). Rupture propagation with finite stress in antiplane strain. *Journal of Geophysical Research*, *81*(20), 3575–3582. https://doi.org/10.1029/JB081i020p03575

Aochi, H. (2003). The 1999 Izmit, Turkey, Earthquake: Nonplanar Fault Structure, Dynamic Rupture Process, and Strong Ground Motion. *Bulletin of the Seismological Society of America*, *93*(3), 1249–1266. https://doi.org/10.1785/0120020167

Aochi, H., & Ulrich, T. (2015). A Probable Earthquake Scenario near Istanbul Determined from Dynamic Simulations. *Bulletin of the Seismological Society of America*, *105*(3), 1468–1475. https://doi.org/10.1785/0120140283

Bakun, W. H., Flores, C. H., & Ten Brink, U. S. (2012). Significant Earthquakes on the Enriquillo Fault System, Hispaniola, 1500-2010: Implications for Seismic Hazard. *Bulletin of the Seismological Society of America*, *102*(1), 18–30. https://doi.org/10.1785/0120110077

Bien-Aime-Momplaisir, R., Amilcar, H., Murat-Pierre, G., & Cenatus-Amilcar, H. (1988a). Geologic Map of Haiti (Carte géologique de la République d'Haïti).

Bien-Aime-Momplaisir, R., Amilcar, H., Murat-Pierre, G., & Cenatus-Amilcar, H. (1988b). Geologic Map of Haiti (Carte géologique de la République d'Haïti).

Bizzarri, A., & Cocco, M. (2003). Slip-weakening behavior during the propagation of dynamic ruptures obeying rate- and state-dependent friction laws. *Journal of Geophysical Research: Solid Earth*, *108*(B8), 2002JB002198. https://doi.org/10.1029/2002JB002198

Bodin, P., Bilham, R., Behr, J., Gomberg, J., & Hudnut, K. W. (1994). Slip Triggered on Southern California Faults by the 1992 Joshua Tree, Landers, and Big Bear Earthquakes. *Bulletin of the Seismological Society of America*, 11.

Boisson, D. (1987). *Etude geologique du massif du nord d'haiti (hispaniola - grandes antilles)* [PhD Thesis]. http://www.theses.fr/1987PA066771

Brodsky, E. E. (2006). Long-range triggered earthquakes that continue after the wave train passes. *Geophysical Research Letters*, *33*(15), 2006GL026605. https://doi.org/10.1029/2006GL026605

Calais, E., Symithe, S., Monfret, T., Delouis, B., Lomax, A., Courboulex, F., Ampuero, J. P., Lara, P. E., Bletery, Q., Chèze, J., Peix, F., Deschamps, A., de Lépinay, B., Raimbault, B., Jolivet, R., Paul, S., St Fleur, S., Boisson, D., Fukushima, Y., … Meng, L. (2022a). Citizen seismology helps decipher the 2021 Haiti earthquake. *Science*, *376*(6590), 283–287. https://doi.org/10.1126/science.abn1045

Calais, E., Freed, A., Mattioli, G., Amelung, F., Jónsson, S., Jansma, P., Hong, S.-H., Dixon, T., Prépetit, C., & Momplaisir, R. (2010a). Transpressional rupture of an unmapped fault during the 2010 Haiti earthquake. *Nature Geoscience*, *3*(11), 794–799. https://doi.org/10.1038/ngeo992

Calais, E., Freed, A., Mattioli, G., Amelung, F., Jónsson, S., Jansma, P., Hong, S.-H., Dixon, T., Prépetit, C., & Momplaisir, R. (2010b). Transpressional rupture of an unmapped fault during the 2010 Haiti earthquake. *Nature Geoscience*, *3*(11), 794–799. https://doi.org/10.1038/ngeo992

Calais, E., Symithe, S., Monfret, T., Delouis, B., Lomax, A., Courboulex, F., Ampuero, J. P., Lara, P. E., Bletery, Q., Chèze, J., Peix, F., Deschamps, A., de Lépinay, B., Raimbault, B., Jolivet, R., Paul, S., St Fleur, S., Boisson, D., Fukushima, Y., … Meng, L. (2022b).

Citizen seismology helps decipher the 2021 Haiti earthquake. *Science*, *376*(6590), 283–287. https://doi.org/10.1126/science.abn1045

Calais, E., Symithe, S., Mercier de Lépinay, B., & Prépetit, C. (2015). Plate boundary segmentation in the northeastern Caribbean from geodetic measurements and Neogene geological observations. *Comptes Rendus. Géoscience*, *348*(1), 42–51. https://doi.org/10.1016/j.crte.2015.10.007

Calais, E., Symithe, S., Mercier de Lépinay, B., & Prépetit, C. (2016). Plate boundary segmentation in the northeastern Caribbean from geodetic measurements and Neogene geological observations. *Comptes Rendus Geoscience*, *348*(1), 42–51. https://doi.org/10.1016/j.crte.2015.10.007

Calais, E., Symithe, S. J., & de Lépinay, B. M. (2023). Strain Partitioning within the Caribbean–North America Transform Plate Boundary in Southern Haiti, Tectonic and Hazard Implications. *Bulletin of the Seismological Society of America*, *113*(1), 131–142. https://doi.org/10.1785/0120220121

Chen, C. W., & Zebker, H. A. (2002). Phase unwrapping for large SAR interferograms: Statistical segmentation and generalized network models. *IEEE Transactions on Geoscience and Remote Sensing*, *40*(8), 11.

Crameri, F., Shephard, G. E., & Heron, P. J. (2020). The misuse of colour in science communication. *Nature Communications*, *11*(1), 5444. https://doi.org/10.1038/s41467-020-19160-7

DeMets, C., Jansma, P. E., Mattioli, G. S., Dixon, T. H., Farina, F., Bilham, R., Calais, E., & Mann, P. (2000a). GPS geodetic constraints on Caribbean-North America Plate Motion. *Geophysical Research Letters*, *27*(3), 437–440. https://doi.org/10.1029/1999GL005436

DeMets, C., Jansma, P. E., Mattioli, G. S., Dixon, T. H., Farina, F., Bilham, R., Calais, E., & Mann, P. (2000b). GPS geodetic constraints on Caribbean-North America Plate Motion. *Geophysical Research Letters*, *27*(3), 437–440. https://doi.org/10.1029/1999GL005436

Douilly, R., Aochi, H., Calais, E., & Freed, A. M. (2015a). Three-dimensional dynamic rupture simulations across interacting faults: The $\boldsymbol{M}_w$ 7.0, 2010, Haiti earthquake. *Journal of Geophysical Research: Solid Earth*, *120*(2), 1108–1128. https://doi.org/10.1002/2014JB011595

Douilly, R., Aochi, H., Calais, E., & Freed, A. M. (2015b). Three-dimensional dynamic rupture simulations across interacting faults: The ***M*** $_\textrm *w* $ 7.0, 2010, Haiti earthquake. *Journal of Geophysical Research: Solid Earth*, *120*(2), 1108–1128. https://doi.org/10.1002/2014JB011595

Douilly, R., Haase, J. S., Ellsworth, W. L., Bouin, M.-P., Calais, E., Symithe, S. J., Armbruster, J. G., de Lepinay, B. M., Deschamps, A., Mildor, S.-L., Meremonte, M. E., & Hough,

S. E. (2013a). Crustal Structure and Fault Geometry of the 2010 Haiti Earthquake from Temporary Seismometer Deployments. *Bulletin of the Seismological Society of America*, *103*(4), 2305–2325. https://doi.org/10.1785/0120120303

Douilly, R., Haase, J. S., Ellsworth, W. L., Bouin, M.-P., Calais, E., Symithe, S. J., Armbruster, J. G., de Lepinay, B. M., Deschamps, A., Mildor, S.-L., Meremonte, M. E., & Hough, S. E. (2013b). Crustal Structure and Fault Geometry of the 2010 Haiti Earthquake from Temporary Seismometer Deployments. *Bulletin of the Seismological Society of America*, *103*(4), 2305–2325. https://doi.org/10.1785/0120120303

Douilly, R., Mavroeidis, G. P., & Calais, E. (2017). Simulation of broad-band strong ground motion for a hypothetical Mw 7.1 earthquake on the Enriquillo Fault in Haiti. *Geophysical Journal International*, *211*(1), 400–417. https://doi.org/10.1093/gji/ggx312

Douilly, R., Paul, S., Monfret, T., Deschamps, A., Ambrois, D., Symithe, S. J., Fleur, S. S., Courboulex, F., Calais, E., Boisson, D., Lépinay, B. M. d., Font, Y., & Chèze, J. (2022). Rupture Segmentation of the August 14, 2021 Mw7.2 Nippes, Haiti, Earthquake Using Aftershock Relocation from a Local Seismic Deployment. *Bulletin of the Seismological Society of America*.

Douilly, R., Paul, S., Monfret, T., Deschamps, A., Ambrois, D., Symithe, S. J., St Fleur, S., Courboulex, F., Calais, E., Boisson, D., de Lépinay, B. M., Font, Y., & Chèze, J. (2023). Rupture Segmentation of the 14 August 2021 Mw 7.2 Nippes, Haiti, Earthquake Using Aftershock Relocation from a Local Seismic Deployment. *Bulletin of the Seismological Society of America*, *113*(1), 58–72. https://doi.org/10.1785/0120220128

Dumbser, M., & Käser, M. (2006). An arbitrary high-order discontinuous Galerkin method for elastic waves on unstructured meshes - II. The three-dimensional isotropic case. *Geophysical Journal International*, *167*(1), 319–336. https://doi.org/10.1111/j.1365-246X.2006.03120.x

Elkhoury, J. E., Brodsky, E. E., & Agnew, D. C. (2006). Seismic waves increase permeability. *Nature*, *441*(7097), 1135–1138. https://doi.org/10.1038/nature04798

Farr, T. G., Rosen, P. A., Caro, E., Crippen, R., Duren, R., Hensley, S., Kobrick, M., Paller, M., Rodriguez, E., Roth, L., Seal, D., Shaffer, S., Shimada, J., Umland, J., Werner, M., Oskin, M., Burbank, D., & Alsdorf, D. (2007). The Shuttle Radar Topography Mission. *Reviews of Geophysics*, *45*(2), 2005RG000183. https://doi.org/10.1029/2005RG000183

Fialko, Y., Sandwell, D., Agnew, D., Simons, M., Shearer, P., & Minster, B. (2002). Deformation on Nearby Faults Induced by the 1999 Hector Mine Earthquake. *Science*, *297*(5588), 1858–1862. https://doi.org/10.1126/science.1074671

Field, E. H., Arrowsmith, R. J., Biasi, G. P., Bird, P., Dawson, T. E., Felzer, K. R., Jackson, D. D., Johnson, K. M., Jordan, T. H., Madden, C., Michael, A. J., Milner, K. R., Page, M. T., Parsons, T., Powers, P. M., Shaw, B. E., Thatcher, W. R., Weldon, R. J., & Zeng, Y. (2014). Uniform California Earthquake Rupture Forecast, Version 3 (UCERF3)–The Time-Independent Model. *Bulletin of the Seismological Society of America*, *104*(3), 1122–1180. https://doi.org/10.1785/0120130164

Frankel, A., Harmsen, S., Mueller, C., Calais, E., & Haase, J. (2011). Seismic Hazard Maps for Haiti. *Earthquake Spectra*, *27*(1_suppl1), 23–41. https://doi.org/10.1193/1.3631016

Gabriel, A.-A., Ulrich, T., Marchandon, M., Biemiller, J., & Rekoske, J. (2023). 3D Dynamic Rupture Modeling of the 6 February 2023, Kahramanmaraş, Turkey Mw 7.8 and 7.7 Earthquake Doublet Using Early Observations. *The Seismic Record*, *3*(4), 342–356. https://doi.org/10.1785/0320230028

Galis, M., Ampuero, J.-P., Mai, P. M., & Kristek, J. (2019). Initiation and arrest of earthquake ruptures due to elongated overstressed regions. *Geophysical Journal International*, *217*(3), 1783–1797. https://doi.org/10.1093/gji/ggz086

Garagash, D. I. (2021). Fracture mechanics of rate-and-state faults and fluid injection induced slip. *Philosophical Transactions of the Royal Society A: Mathematical, Physical and Engineering Sciences*, *379*(2196), 20200129. https://doi.org/10.1098/rsta.2020.0129

Glehman, J., Gabriel, A.-A., Ulrich, T., Ramos, M., Huang, Y., & Lindsey, E. (2024, August). Partial ruptures governed by the complex interplay between geodetic slip deficit, rigidity, and pore fluid pressure in 3D Cascadia dynamic rupture simulations. https://doi.org/10.31223/X5GH66

Goldberg, D. E., Koch, P., Melgar, D., Riquelme, S., & Yeck, W. L. (2022). Beyond the Teleseism: Introducing Regional Seismic and Geodetic Data into Routine USGS Finite-Fault Modeling. *Seismological Research Letters*, *93*(6), 3308–3323. https://doi.org/10.1785/0220220047

Hardebeck, J. L., & Harris, R. A. (2022). Earthquakes in the Shadows: Why Aftershocks Occur at Surprising Locations. *The Seismic Record*, *2*(3), 207–216. https://doi.org/10.1785/0320220023

Harris, R. A., Barall, M., Andrews, D. J., Duan, B., Ma, S., Dunham, E. M., Gabriel, A.-A., Kaneko, Y., Kase, Y., Aagaard, B. T., Oglesby, D. D., Ampuero, J.-P., Hanks, T. C., & Abrahamson, N. (2011). Verifying a Computational Method for Predicting Extreme Ground Motion. *Seismological Research Letters*, *82*(5), 638–644. https://doi.org/10.1785/gssrl.82.5.638

Harris, R. A. (1998). Introduction to Special Section: Stress Triggers, Stress Shadows, and Implications for Seismic Hazard. *Journal of Geophysical Research: Solid Earth*, *103*(B10), 24347–24358. https://doi.org/10.1029/98JB01576

Harris, R. A., Barall, M., Aagaard, B., Ma, S., Roten, D., Olsen, K., Duan, B., Liu, D., Luo, B., Bai, K., Ampuero, J.-P., Kaneko, Y., Gabriel, A.-A., Duru, K., Ulrich, T., Wollherr, S., Shi, Z., Dunham, E., Bydlon, S., … Dalguer, L. (2018). A Suite of Exercises for Verifying Dynamic Earthquake Rupture Codes. *Seismological Research Letters*, *89*(3), 1146–1162. https://doi.org/10.1785/0220170222

Hashimoto, M., Fukushima, Y., & Fukahata, Y. (2011). Fan-delta uplift and mountain subsidence during the Haiti 2010 earthquake. *Nature Geoscience*, *4*(4), 255–259. https://doi.org/10.1038/ngeo1115

Hayek, J. N., Marchandon, M., Li, D., Pousse-Beltran, L., Hollingsworth, J., Li, T., & Gabriel, A.-A. (2024). Non-Typical Supershear Rupture: Fault Heterogeneity and Segmentation Govern Unilateral Supershear and Cascading Multi-Fault Rupture in the 2021 Mw7.4 Maduo Earthquake. *Geophysical Research Letters*, *51*(20), e2024GL110128. https://doi.org/10.1029/2024GL110128

Hayes, G. P., Briggs, R. W., Sladen, A., Fielding, E. J., Prentice, C., Hudnut, K., Mann, P., Taylor, F. W., Crone, A. J., Gold, R., Ito, T., & Simons, M. (2010). Complex rupture during the 12 January 2010 Haiti earthquake. *Nature Geoscience*, *3*(11), 800–805. https://doi.org/10.1038/ngeo977

Heidbach, O., Rajabi, M., Cui, X., Fuchs, K., Müller, B., Reinecker, J., Reiter, K., Tingay, M., Wenzel, F., Xie, F., Ziegler, M. O., Zoback, M.-L., & Zoback, M. (2018). The World Stress Map database release 2016: Crustal stress pattern across scales. *Tectonophysics*, *744*, 484–498. https://doi.org/10.1016/j.tecto.2018.07.007

Heinecke, A., Breuer, A., Rettenberger, S., Bader, M., Gabriel, A.-A., Pelties, C., Bode, A., Barth, W., Liao, X.-K., Vaidyanathan, K., Smelyanskiy, M., & Dubey, P. (2014). Petascale High Order Dynamic Rupture Earthquake Simulations on Heterogeneous Supercomputers. *SC14: International Conference for High Performance Computing, Networking, Storage and Analysis*, 3–14. https://doi.org/10.1109/SC.2014.6

Hough, S. E., Martin, S. S., Symithe, S. J., & Briggs, R. (2023). Rupture Scenarios for the 3 June 1770 Haiti Earthquake. *Bulletin of the Seismological Society of America*, *113*(1), 157–185. https://doi.org/10.1785/0120220108

Hussain, E., Wright, T. J., Walters, R. J., Bekaert, D., Hooper, A., & Houseman, G. A. (2016). Geodetic observations of postseismic creep in the decade after the 1999 Izmit earthquake, Turkey: Implications for a shallow slip deficit. *Journal of Geophysical Research: Solid Earth*, *121*(4), 2980–3001. https://doi.org/10.1002/2015JB012737

Ida, Y. (1972). Cohesive force across the tip of a longitudinal-shear crack and Griffith's specific surface energy. *Journal of Geophysical Research*, *77*(20), 3796–3805. https://doi.org/10.1029/JB077i020p03796

Jia, Z., Jin, Z., Marchandon, M., Ulrich, T., Gabriel, A.-A., Fan, W., Shearer, P., Zou, X., Rekoske, J., Bulut, F., Garagon, A., & Fialko, Y. (2023). The complex dynamics of the 2023 Kahramanmaraş, Turkey, M_w 7.8-7.7 earthquake doublet. *Science*, *381*(6661), 985–990. https://doi.org/10.1126/science.adi0685

Jiang, J., Bock, Y., & Klein, E. (2021). Coevolving early afterslip and aftershock signatures of a San Andreas fault rupture. *Science Advances*, *7*(15), eabc1606. https://doi.org/10.1126/sciadv.abc1606

Johanson, I. A. (2006). Coseismic and Postseismic Slip of the 2004 Parkfield Earthquake from Space-Geodetic Data. *Bulletin of the Seismological Society of America*, *96*(4B), S269–S282. https://doi.org/10.1785/0120050818

Kaneko, Y., Lapusta, N., & Ampuero, J.-P. (2008). Spectral element modeling of spontaneous earthquake rupture on rate and state faults: Effect of velocity-strengthening friction at shallow depths. *Journal of Geophysical Research: Solid Earth*, *113*(B9), 2007JB005553. https://doi.org/10.1029/2007JB005553

Kilb, D. (2003). A strong correlation between induced peak dynamic Coulomb stress change from the 1992 *M* 7.3 Landers, California, earthquake and the hypocenter of the 1999 *M* 7.1 Hector Mine, California, earthquake. *Journal of Geophysical Research: Solid Earth*, *108*(B1). https://doi.org/10.1029/2001JB000678

Kilb, D., Gomberg, J., & Bodin, P. (2002). Aftershock triggering by complete Coulomb stress changes. *Journal of Geophysical Research: Solid Earth*, *107*(B4). https://doi.org/10.1029/2001JB000202

King, G. C. P., Stein, R. S., & Lin, J. (1994). Static stress changes and the triggering of earthquakes. *Bulletin of the Seismological Society of America*, *84*(3), 935–953. https://doi.org/10.1785/BSSA0840030935

Krenz, L., Uphoff, C., Ulrich, T., Gabriel, A.-A., Abrahams, L. S., Dunham, E. M., & Bader, M. (2021). 3D acoustic-elastic coupling with gravity: The dynamics of the 2018 Palu, Sulawesi earthquake and tsunami. *Proceedings of the International Conference for High Performance Computing, Networking, Storage and Analysis*, 1–14. https://doi.org/10.1145/3458817.3476173

Langbein, J. (2006). Coseismic and Initial Postseismic Deformation from the 2004 Parkfield, California, Earthquake, Observed by Global Positioning System, Electronic Distance Meter, Creepmeters, and Borehole Strainmeters. *Bulletin of the Seismological Society of America*, *96*(4B), S304–S320. https://doi.org/10.1785/0120050823

Li, Y., & Bürgmann, R. (2021). Partial Coupling and Earthquake Potential Along the Xianshuihe Fault, China. *Journal of Geophysical Research: Solid Earth*, *126*(7). https://doi.org/10.1029/2020JB021406

Li, Z., & Wang, T. (2023). Coseismic and Early Postseismic Slip of the 2021 Mw 7.2 Nippes, Haiti, Earthquake: Transpressional Rupture of a Nonplanar Dipping Fault System. *Seismological Research Letters*, *94*(6), 2595–2608. https://doi.org/10.1785/0220230160

Ma, S., Custódio, S., Archuleta, R. J., & Liu, P. (2008). Dynamic modeling of the 2004 M $_{w}$ 6.0 Parkfield, California, earthquake. *Journal of Geophysical Research: Solid Earth*, *113*(B2), 2007JB005216. https://doi.org/10.1029/2007JB005216

Madariaga, R. (1976). Dynamics of an expanding circular fault. *Bulletin of the Seismological Society of America*, *66*(3), 639–666. https://doi.org/10.1785/BSSA0660030639

Madden, E. H., Ulrich, T., & Gabriel, A.-A. (2022). The State of Pore Fluid Pressure and 3-D Megathrust Earthquake Dynamics. *Journal of Geophysical Research: Solid Earth*, *127*(4), e2021JB023382. https://doi.org/10.1029/2021JB023382

Mann, P., Calais, E., Ruegg, J.-C., DeMets, C., Jansma, P. E., & Mattioli, G. S. (2002). Oblique collision in the northeastern Caribbean from GPS measurements and geological observations: Oblique Collision In the Northeastern Caribbean. *Tectonics*, *21*(6), 7–1–7–26. https://doi.org/10.1029/2001TC001304

Mann, P., Taylor, F., Edwards, R., & Ku, T.-L. (1995). Actively evolving microplate formation by oblique collision and sideways motion along strike-slip faults: An example from the northeastern Caribbean plate margin. *Tectonophysics*, *246*(1-3), 1–69. https://doi.org/10.1016/0040-1951(94)00268-E

Martin, S. S., & Hough, S. E. (2022). The 8 April 1860 Jour de Pâques Earthquake Sequence in Southern Haiti. *Bulletin of the Seismological Society of America*, *112*(5), 2468–2486. https://doi.org/10.1785/0120220016

Maurer, J., Dutta, R., Vernon, A., & Vajedian, S. (2022a, March). *Complex rupture and triggered aseismic creep during the August 14, 2021 Haiti earthquake from satellite geodesy* (Preprint). Geodesy. https://doi.org/10.1002/essoar.10510731.1

Maurer, J., Dutta, R., Vernon, A., & Vajedian, S. (2022b, March). *Complex rupture and triggered aseismic creep during the August 14, 2021 Haiti earthquake from satellite geodesy* (preprint). Geodesy. https://doi.org/10.1002/essoar.10510731.1

McCann, W. R. (2006). Estimating the Threat of Tsunamigenic Earthquakes and Earthquake Induced-Landslide Tsunami in the Caribbean [ISBN: 978-981-256-535-8 978-981-277-461-3 Place: San Juan, Beach Hotel, Puerto Rico Publisher: WORLD SCIENTIFIC]. *Caribbean Tsunami Hazard*, 43–65. https://doi.org/10.1142/9789812774613_0002

Meng, L., Ampuero, J.-P., Sladen, A., & Rendon, H. (2012). High-resolution backprojection at regional distance: Application to the Haiti M7.0 earthquake and comparisons with finite source studies. *Journal of Geophysical Research: Solid Earth*, *117*(B4). https:

//doi.org/10.1029/2011JB008702
_eprint: https://onlinelibrary.wiley.com/doi/pdf/10.1029/2011JB008702.

Mercier de Lepinay, B., Deschamps, A., Klingelhoefer, F., Mazabraud, Y., Delouis, B., Clouard, V., Hello, Y., Crozon, J., Marcaillou, B., Graindorge, D., Vallée, M., Perrot, J., Bouin, M.-P., Saurel, J.-M., Charvis, P., & St-Louis, M. (2011). The 2010 Haiti earthquake: A complex fault pattern constrained by seismologic and tectonic observations: The 2010 Haiti Earthquake Fault Pattern. *Geophysical Research Letters*, *38*(22), n/a–n/a. https://doi.org/10.1029/2011GL049799

Mercier de Lépinay, B., Deschamps, A., Klingelhoefer, F., Mazabraud, Y., Delouis, B., Clouard, V., Hello, Y., Crozon, J., Marcaillou, B., Graindorge, D., Vallée, M., Perrot, J., Bouin, M.-P., Saurel, J.-M., Charvis, P., & St-Louis, M. (2011). The 2010 Haiti earthquake: A complex fault pattern constrained by seismologic and tectonic observations: THE 2010 HAITI EARTHQUAKE FAULT PATTERN. *Geophysical Research Letters*, *38*(22), n/a–n/a. https://doi.org/10.1029/2011GL049799

Nielsen, S. B., Carlson, J. M., & Olsen, K. B. (2000). Influence of friction and fault geometry on earthquake rupture. *Journal of Geophysical Research: Solid Earth*, *105*(B3), 6069–6088. https://doi.org/10.1029/1999JB900350

Okada, Y. (1992). Internal deformation due to shear and tensile faults in a half-space. *Bulletin of the Seismological Society of America*, *82*(2), 1018–1040. https://doi.org/10.1785/BSSA0820021018

Okuwaki, R., & Fan, W. (2022a). Oblique Convergence Causes Both Thrust and Strike-Slip Ruptures During the 2021 M 7.2 Haiti Earthquake. *Geophysical Research Letters*, *49*(2), e2021GL096373. https://doi.org/10.1029/2021GL096373

Okuwaki, R., & Fan, W. (2022b). Oblique Convergence Causes Both Thrust and Strike-Slip Ruptures During the 2021 M 7.2 Haiti Earthquake. *Geophysical Research Letters*, *49*(2). https://doi.org/10.1029/2021GL096373

Palgunadi, K. H., Gabriel, A.-A., Ulrich, T., López-Comino, J. Á., & Mai, P. M. (2020). Dynamic Fault Interaction during a Fluid-Injection-Induced Earthquake: The 2017 Mw 5.5 Pohang Event. *Bulletin of the Seismological Society of America*, *110*(5), 2328–2349. https://doi.org/10.1785/0120200106

Pelties, C., Gabriel, A.-A., & Ampuero, J.-P. (2014). Verification of an ADER-DG method for complex dynamic rupture problems. *Geoscientific Model Development*, *7*(3), 847–866. https://doi.org/10.5194/gmd-7-847-2014

Pollitz, F. F., Stein, R. S., Sevilgen, V., & Bürgmann, R. (2012). The 11 April 2012 east Indian Ocean earthquake triggered large aftershocks worldwide. *Nature*, *490*(7419), 250–253. https://doi.org/10.1038/nature11504

Prentice, C. S., Mann, P., Crone, A. J., Gold, R. D., Hudnut, K. W., Briggs, R. W., Koehler, R. D., & Jean, P. (2010a). Seismic hazard of the Enriquillo–Plantain Garden fault in Haiti inferred from palaeoseismology. *Nature Geoscience*, *3*(11), 789–793. https://doi.org/10.1038/ngeo991

Prentice, C. S., Mann, P., Crone, A. J., Gold, R. D., Hudnut, K. W., Briggs, R. W., Koehler, R. D., & Jean, P. (2010b). Seismic hazard of the Enriquillo–Plantain Garden fault in Haiti inferred from palaeoseismology. *Nature Geoscience*, *3*(11), 789–793. https://doi.org/10.1038/ngeo991

Prentice, C. S., Mann, P., Peña, L. R., & Burr, G. (2003). Slip rate and earthquake recurrence along the central Septentrional fault, North American–Caribbean plate boundary, Dominican Republic. *Journal of Geophysical Research: Solid Earth*, *108*(B3), 2001JB000442. https://doi.org/10.1029/2001JB000442

Price, E. J., & Sandwell, D. T. (1998a). Small-scale deformations associated with the 1992 Landers, California, earthquake mapped by synthetic aperture radar interferometry phase gradients. *Journal of Geophysical Research: Solid Earth*, *103*(B11), 27001–27016. https://doi.org/10.1029/98JB01821

Price, E. J., & Sandwell, D. T. (1998b). Small-scale deformations associated with the 1992 Landers, California, earthquake mapped by synthetic aperture radar interferometry phase gradients. *Journal of Geophysical Research: Solid Earth*, *103*(B11), 27001–27016. https://doi.org/10.1029/98JB01821

Raimbault, B., Jolivet, R., Calais, E., Symithe, S., Fukushima, Y., & Dubernet, P. (2023). Rupture Geometry and Slip Distribution of the Mw 7.2 Nippes Earthquake, Haiti, From Space Geodetic Data. *Geochemistry, Geophysics, Geosystems*, *24*(4), e2022GC010752. https://doi.org/10.1029/2022GC010752

Ramos, M. D., Thakur, P., Huang, Y., Harris, R. A., & Ryan, K. J. (2022). Working with Dynamic Earthquake Rupture Models: A Practical Guide. *Seismological Research Letters*, *93*(4), 2096–2110. https://doi.org/10.1785/0220220022

Rice, J. R. (1992). Chapter 20 Fault Stress States, Pore Pressure Distributions, and the Weakness of the San Andreas Fault. In *International Geophysics* (pp. 475–503, Vol. 51). Elsevier. https://doi.org/10.1016/S0074-6142(08)62835-1

Rosen, P. A., & Kumar, R. (2021). NASA-ISRO SAR (NISAR) Mission Status. *2021 IEEE Radar Conference (RadarConf21)*, 1–6. https://doi.org/10.1109/RadarConf2147009.2021.9455211

Saint Fleur, N., Dessable, J. E., Saint-Preux, G., Calais, É., Feuillet, N., Boisson, D., de Chabalier, J.-B., & Klinger, Y. (2024). Tectonic, Topographic, Geologic, and Hydroclimatic Influence on Crack Formation During the 2021 Haiti Earthquake. *Geochemistry, Geophysics, Geosystems*, *25*(7), e2023GC011255. https://doi.org/10.1029/2023GC011255

Saint Fleur, N., Feuillet, N., Grandin, R., Jacques, E., Weil-Accardo, J., & Klinger, Y. (2015). Seismotectonics of southern Haiti: A new faulting model for the 12 January 2010 *M* 7.0 earthquake. *Geophysical Research Letters*, *42*(23). https://doi.org/10.1002/2015GL065505

Saint Fleur, N., Feuillet, N., Grandin, R., Jacques, E., Weil-Accardo, J., & Klinger, Y. (2015). Seismotectonics of southern Haiti: A new faulting model for the 12 January 2010 *M* 7.0 earthquake. *Geophysical Research Letters*, *42*(23). https://doi.org/10.1002/2015GL065505

Saint Fleur, N., Klinger, Y., & Feuillet, N. (2020a). Detailed map, displacement, paleoseismology, and segmentation of the Enriquillo-Plantain Garden Fault in Haiti. *Tectonophysics*, *778*, 228368. https://doi.org/10.1016/j.tecto.2020.228368

Saint Fleur, N., Klinger, Y., & Feuillet, N. (2020b). Detailed map, displacement, paleoseismology, and segmentation of the Enriquillo-Plantain Garden Fault in Haiti. *Tectonophysics*, *778*, 228368. https://doi.org/10.1016/j.tecto.2020.228368

Sandwell, D. T., Mellors, R., Tong, X., Wei, M., & Wessel, P. (2011, April). *GMTSAR: An InSAR Processing System Based on Generic Mapping Tools* (tech. rep. No. LLNL-TR-481284, 1090004). https://doi.org/10.2172/1090004

Sandwell, D. T., & Price, E. J. (1998). Phase gradient approach to stacking interferograms. *Journal of Geophysical Research: Solid Earth*, *103*(B12), 30183–30204. https://doi.org/10.1029/1998JB900008

Sandwell, D. T., Sichoix, L., Agnew, D., Bock, Y., & Minster, J.-B. (2000a). Near real-time radar interferometry of the Mw 7.1 Hector Mine Earthquake. *Geophysical Research Letters*, *27*(19), 3101–3104. https://doi.org/10.1029/1999GL011209

Sandwell, D. T., Sichoix, L., Agnew, D., Bock, Y., & Minster, J.-B. (2000b). Near real-time radar interferometry of the Mw 7.1 Hector Mine Earthquake. *Geophysical Research Letters*, *27*(19), 3101–3104. https://doi.org/10.1029/1999GL011209

Shanker, A., & Zebker, H. (2009). Sparse Two-Dimensional Phase Unwrapping Using Regular Grid Methods. *IEEE Geoscience and Remote Sensing Letters*, *6*(3), 519–522. https://doi.org/10.1109/LGRS.2009.2020522

Simpson, R. W. (1997). Quantifying Anderson's fault types. *Journal of Geophysical Research: Solid Earth*, *102*(B8), 17909–17919. https://doi.org/10.1029/97JB01274

Stein, R. S., Barka, A. A., & Dieterich, J. H. (1997). Progressive failure on the North Anatolian fault since 1939 by earthquake stress triggering. *Geophysical Journal International*, *128*(3), 594–604. https://doi.org/10.1111/j.1365-246X.1997.tb05321.x

Symithe, S., Calais, E., de Chabalier, J. B., Robertson, R., & Higgins, M. (2015). Current block motions and strain accumulation on active faults in the Caribbean. *Journal of Geophysical Research: Solid Earth*, *120*(5), 3748–3774. https://doi.org/10.1002/2014JB011779

Symithe, S. J., Calais, E., Haase, J. S., Freed, A. M., & Douilly, R. (2013a). Coseismic Slip Distribution of the 2010 M 7.0 Haiti Earthquake and Resulting Stress Changes on Regional Faults. *Bulletin of the Seismological Society of America*, *103*(4), 2326–2343. https://doi.org/10.1785/0120120306

Symithe, S., & Calais, E. (2016). Present-day shortening in Southern Haiti from GPS measurements and implications for seismic hazard. *Tectonophysics*, *679*, 117–124. https://doi.org/10.1016/j.tecto.2016.04.034

Symithe, S. J., Calais, E., de Chabalier, J. B., Robertson, R., & Higgins, M. (2015). Current block motions and strain accumulation on active faults in the Caribbean: Current Caribbean Kinematics. *Journal of Geophysical Research: Solid Earth*, *120*(5), 3748–3774. https://doi.org/10.1002/2014JB011779

Symithe, S. J., Calais, E., Haase, J. S., Freed, A. M., & Douilly, R. (2013b). Coseismic Slip Distribution of the 2010 M 7.0 Haiti Earthquake and Resulting Stress Changes on Regional Faults. *Bulletin of the Seismological Society of America*, *103*(4), 2326–2343. https://doi.org/10.1785/0120120306

Symithe, S. J., & Calais, E. (2016). Present-day shortening in Southern Haiti from GPS measurements and implications for seismic hazard. *Tectonophysics*, *679*, 117–124. https://doi.org/10.1016/j.tecto.2016.04.034

Taufiqurrahman, T., Gabriel, A.-A., Li, D., Ulrich, T., Li, B., Carena, S., Verdecchia, A., & Gallovič, F. (2023). Dynamics, interactions and delays of the 2019 Ridgecrest rupture sequence. *Nature*, *618*(7964), 308–315. https://doi.org/10.1038/s41586-023-05985-x

Tinti, E., Fukuyama, E., Piatanesi, A., & Cocco, M. (2005). A Kinematic Source-Time Function Compatible with Earthquake Dynamics. *Bulletin of the Seismological Society of America*, *95*(4), 1211–1223. https://doi.org/10.1785/0120040177

Tinti, E., Spudich, P., & Cocco, M. (2005). Earthquake fracture energy inferred from kinematic rupture models on extended faults. *Journal of Geophysical Research: Solid Earth*, *110*(B12), 2005JB003644. https://doi.org/10.1029/2005JB003644

Tinti, E., Casarotti, E., Ulrich, T., Taufiqurrahman, T., Li, D., & Gabriel, A.-A. (2021). Constraining families of dynamic models using geological, geodetic and strong ground motion data: The Mw 6.5, October 30th, 2016, Norcia earthquake, Italy. *Earth and Planetary Science Letters*, *576*, 117237. https://doi.org/10.1016/j.epsl.2021.117237

Toda, S., & Stein, R. S. (2020). Long- and Short-Term Stress Interaction of the 2019 Ridgecrest Sequence and Coulomb-Based Earthquake Forecasts. *Bulletin of the Seismological Society of America*, *110*(4), 1765–1780. https://doi.org/10.1785/0120200169

Toda, Shinji, Stein, R.S, Sevilgen, Volkan, & Lin, Jian. (2011, October). *Coulomb 3.3 Graphic-Rich Deformation and Stress-Change Software for Earthquake, Tectonic, and Volcano Research and Teaching—User Guide* (Open-File Report No. 2011–1060). U.S. Geological Survey.

Tymofyeyeva, E., Fialko, Y., Jiang, J., Xu, X., Sandwell, D., Bilham, R., Rockwell, T. K., Blanton, C., Burkett, F., Gontz, A., & Moafipoor, S. (2019). Slow Slip Event On the Southern San Andreas Fault Triggered by the 2017 *M* $_\textrm *w* $ 8.2 Chiapas (Mexico) Earthquake. *Journal of Geophysical Research: Solid Earth*, *124*(9), 9956–9975. https://doi.org/10.1029/2018JB016765

Ulrich, T., Gabriel, A.-A., Ampuero, J.-P., & Xu, W. (2019). Dynamic viability of the 2016 Mw 7.8 Kaikōura earthquake cascade on weak crustal faults. *Nature Communications*, *10*(1), 1213. https://doi.org/10.1038/s41467-019-09125-w

Uphoff, C., Rettenberger, S., Bader, M., Madden, E. H., Ulrich, T., Wollherr, S., & Gabriel, A.-A. (2017). Extreme scale multi-physics simulations of the tsunamigenic 2004 sumatra megathrust earthquake. *Proceedings of the International Conference for High Performance Computing, Networking, Storage and Analysis*, 1–16. https://doi.org/10.1145/3126908.3126948

USGS. (2021, August). M 7.2 - Nippes, Haiti. Retrieved February 8, 2022, from https://earthquake.usgs.gov/earthquakes/eventpage/us6000f65h/executive

Wang, J., Mann, P., & Stewart, R. R. (2018a). Late Holocene Structural Style and Seismicity of Highly Transpressional Faults in Southern Haiti. *Tectonics*, *37*(10), 3834–3852. https://doi.org/10.1029/2017TC004920

Wang, J., Mann, P., & Stewart, R. R. (2018b). Late Holocene Structural Style and Seismicity of Highly Transpressional Faults in Southern Haiti. *Tectonics*, *37*(10), 3834–3852. https://doi.org/10.1029/2017TC004920

Wdowinski, S., & Hong, S.-H. (2011). Postseismic Deformation Following the 2010 Haiti Earthquake: Time-dependent Surface Subsidence Induced by Groundwater Flow in Response to a Sudden Uplift, 8.

Wdowinski, S., & Hong, S.-H. (2012). Postseismic Deformation Following the 2010 Haiti Earthquake: Time-dependent Surface Subsidence Induced by Groundwater Flow in Response to a Sudden Uplift. *Fringe 2011 Workshop', Frascati, Italy, 19–23 September 2011*.

Wei, S., Fielding, E., Leprince, S., Sladen, A., Avouac, J.-P., Helmberger, D., Hauksson, E., Chu, R., Simons, M., Hudnut, K., Herring, T., & Briggs, R. (2011). Superficial simplicity of the 2010 El Mayor–Cucapah earthquake of Baja California in Mexico. *Nature Geoscience*, *4*(9), 615–618. https://doi.org/10.1038/ngeo1213
Number: 9 Publisher: Nature Publishing Group.

Wells, D. L., & Coppersmith, K. J. (1994). New empirical relationships among magnitude, rupture length, rupture width, rupture area, and surface displacement. *Bulletin of the Seismological Society of America*, *84*(4), 974–1002. https://doi.org/10.1785/BSSA0840040974

Wen, G., Li, X., Zhao, Y., Zhang, Y., Xu, C., & Zheng, Y. (2023). Kinematic Rupture Process and Its Implication of a Thrust and Strike-Slip Multi-Fault during the 2021 Haiti Earthquake. *Remote Sensing*, *15*(7), 1730. https://doi.org/10.3390/rs15071730

Wessel, P., Luis, J. F., Uieda, L., Scharroo, R., Wobbe, F., Smith, W. H. F., & Tian, D. (2013). The Generic Mapping Tools Version 6. *Geochemistry, Geophysics, Geosystems*, 10. https://doi.org/https://doi.org/10.1029/2019GC008515

Wessels, R. J., Ellouz-Zimmermann, N., Bellahsen, N., Hamon, Y., Rosenberg, C., Deschamps, R., Momplaisir, R., Boisson, D., & Leroy, S. (2019). Polyphase tectonic history of the Southern Peninsula, Haiti: From folding-and-thrusting to transpressive strike-slip. *Tectonophysics*, *751*, 125–149. https://doi.org/10.1016/j.tecto.2018.12.011

Wollherr, S., Gabriel, A.-A., & Mai, P. M. (2019). Landers 1992 “Reloaded”: Integrative Dynamic Earthquake Rupture Modeling. *Journal of Geophysical Research: Solid Earth*, *124*(7), 6666–6702. https://doi.org/10.1029/2018JB016355

Xu, X., Sandwell, D. T., & Smith-Konter, B. (2020a). Coseismic Displacements and Surface Fractures from Sentinel-1 InSAR: 2019 Ridgecrest Earthquakes. *Seismological Research Letters*, *91*(4), 1979–1985. https://doi.org/10.1785/0220190275

Xu, X., Sandwell, D. T., & Smith-Konter, B. (2020b). Coseismic Displacements and Surface Fractures from Sentinel-1 InSAR: 2019 Ridgecrest Earthquakes. *Seismological Research Letters*, *91*(4), 1979–1985. https://doi.org/10.1785/0220190275

Xu, X., Sandwell, D. T., Tymofyeyeva, E., González-Ortega, A., & Tong, X. (2017). Tectonic and Anthropogenic Deformation at the Cerro Prieto Geothermal Step-Over Revealed by Sentinel-1A InSAR. *IEEE Transactions on Geoscience and Remote Sensing*, *55*(9), 9.

Xu, X., Sandwell, D. T., Ward, L. A., Milliner, C. W. D., Smith-Konter, B. R., Fang, P., & Bock, Y. (2020a). Surface deformation associated with fractures near the 2019 Ridgecrest earthquake sequence. *Science*, *370*(6516), 605–608. https://doi.org/10.1126/science.abd1690

Xu, X., Sandwell, D. T., Ward, L. A., Milliner, C. W. D., Smith-Konter, B. R., Fang, P., & Bock, Y. (2020b). Surface deformation associated with fractures near the 2019 Ridgecrest earthquake sequence. *Science*, *370*(6516), 605–608. https://doi.org/10.1126/science.abd1690

Yang, H., Yao, S., He, B., & Newman, A. V. (2019). Earthquake rupture dependence on hypocentral location along the Nicoya Peninsula subduction megathrust. *Earth and Planetary Science Letters*, *520*, 10–17. https://doi.org/10.1016/j.epsl.2019.05.030

Yin, H. Z., Xu, X., Haase, J. S., Douilly, R., Sandwell, D. T., & Mercier de Lepinay, B. (2022). Surface Deformation Surrounding the 2021 Mw 7.2 Haiti Earthquake Illuminated by InSAR Observations. *The Bulletin of the Seismological Society of America*, *113*, 41–57. https://doi.org/10.1785/0120220109
ADS Bibcode: 2023BuSSA.113...41Z.

Yin, H. Z., Xu, X., Haase, J. S., Douilly, R., Sandwell, D. T., & Mercier de Lépinay, B. (2022, August). InSAR Interferograms and Products from 2021, M7.2 Nippes, Haiti earthquake (Curated Dataset). https://doi.org/10.5281/zenodo.6834534
Type: dataset.

Yun, J., Gabriel, A.-A., May, D., & Fialko, Y. (2024, October). Controls of Dynamic and Static Stress Changes and Aseismic Slip on Delayed Earthquake Triggering in Rate-and-State Simulations of the 2019 Ridgecrest Earthquake Sequence. https://doi.org/10.31223/X55983